

Electronic Theses and Dissertations, 2020-

2020

Interfacial Properties Modulate Water Entry Dynamics For Spherical Projectiles

Daren Watson
University of Central Florida

 Part of the [Mechanical Engineering Commons](#)
Find similar works at: <https://stars.library.ucf.edu/etd2020>
University of Central Florida Libraries <http://library.ucf.edu>

This Doctoral Dissertation (Open Access) is brought to you for free and open access by STARS. It has been accepted for inclusion in Electronic Theses and Dissertations, 2020- by an authorized administrator of STARS. For more information, please contact STARS@ucf.edu.

STARS Citation

Watson, Daren, "Interfacial Properties Modulate Water Entry Dynamics For Spherical Projectiles" (2020). *Electronic Theses and Dissertations, 2020-*. 426.
<https://stars.library.ucf.edu/etd2020/426>

INTERFACIAL PROPERTIES MODULATE WATER ENTRY DYNAMICS FOR SPHERICAL
PROJECTILES

by

DAREN ANTONIO WATSON
M.S., University of Central Florida, 2019
M.Phil., University of the West Indies, 2016
B.S. (Hons.), University of the West Indies, 2013

A dissertation submitted in partial fulfilment of the requirements
for the degree of Doctor of Philosophy
in the Department of Mechanical Engineering
in the College of Engineering and Computer Science
at the University of Central Florida
Orlando, Florida

Fall Term
2020

Major Professor: Andrew Dickerson

© 2020 Daren Antonio Watson

ABSTRACT

Rigid bodies impacting liquid pools incite splashing and air-entraining cavities that depend on impactor shape, entry speed, surface texture, and free surface conditions. In this body of work, we investigate the influence of interfacial properties on water entry dynamics for free-falling spherical projectiles. Our investigations translate to everyday fluid-structure interactions that are complex and generally conclude beyond the temporal acuity of the naked eye. High-speed videography between 1000 – 3200 fps is used to digitize the water entry process and measure salient splash features under different initial conditions. We assess splashes arising from the impacts of free-falling hydrophilic spheres with thin, non-woven fabrics resting atop a liquid bath to ascertain alterations to splash crowns, air-cavities, and Worthington jets, when compared to impacts onto an unaltered, quiescent free surface. The inclusion of fabrics promotes air-entrainment for hydrophilic spheres, well below the impact-velocity threshold of 8 m/s otherwise required for cavity formation. Meager amounts of fabric amplifies splash metrics while providing the drag-reducing benefits of flow separation. Punctured fabrics suppress splash crowns normally seen for cavity-producing impacts while intact fabrics generate deeper cavities, higher Worthington jets, and more pronounced splash crowns. We proceed to modulate super-surface splash features, and alter sphere trajectories with impactor surface texture. When fluid flowing around the impactor encounters the hydrophobic surface, flow separation is tripped and air entrained across all entry speeds and impact orientations. We conclude this work by replacing solid impactors with liquid drops impacting passive super-surface particles, an experimental system inspired by the survival of water striders during rainfall. We show the strider's locomotive response, low density, resistance to wetting when briefly submerged, and the ability to regain super-surface rest state, render it impervious to impacting water drops. The compendium of new observations from our work augur well for water entry applications where the coupled dynamics of flow separation and passive trajectory control are desirable.

To my mother and father,
Sheryl Watson and Worrell Watson,
who both inspired me to pursue my dreams against all odds.
May I honor their courage, faith, wisdom, and tenacity for success.

ACKNOWLEDGMENTS

To Dr. Andrew Dickerson, for advising my dissertation, his unwavering support, creative research ideas, uncompromising push for excellence, and a well-resourced lab environment. May my intellectual endeavors honor your mentorship.

To the members of my doctoral committee, Dr. Samik Bhattacharya, Dr. Michael Kinzel, and Dr. Tadd Truscott for their diligence, scrutiny, and many useful comments. I look forward to further scientific explorations with your insightful contributions.

To my parents Sheryl Watson and Worrell Watson, my siblings Dean Watson, and Dinelle Watson, for their sacrifice and understanding towards the pursuit of my dreams and ambitions. One love.

To Shayzan McBeam, Bernadette Hutchinson, the US Embassy-Kingston, and the Fulbright Association, for the Fulbright Graduate Scholarship that made it all possible, and the National Science Foundation (CBET-1941341), for funding our research.

To Jeremy Stephens, for his assistance in the onset of my research. Thanks for your unwavering support, attention to detail, and the role played in getting my first two publications.

To Madison Weinberg, Joshua Bom, Chris Souchik, Jonathan Galves, Hiba Khan, Ryan DiAmco, Mason Thornton, and Alex Tao, for assistance on my projects. Thanks for spending hours constructing experiments, recording videos, and tracking data.

To Erfanul Alam, Dr. Nicholas Smith, Milos Krsmanovic, Dr. Dipankar Biswas, and Amy Lebanoff for their useful conversations, unparalleled camaraderie, and insightful experimental support. May our intellectual endeavors honor the FaST Lab's legacy.

To Dr. Tadd Truscott and Rafsan Rabbi, for helping me adjust to life in Logan-Utah during my trip

in July 2019. I could not have asked for a better experience. Looking forward to visiting again.

To Professor Michael Taylor, Dr. Tannecia Stephenson, and my colleagues in the Department of Physics at the University of the West Indies, for providing the platform that initiated my academic journey. May your efforts continue to inspire other Jamaican scholars to reach for the stars.

To Dr. Jean-Francois Dorville, Dr. Keith Duncan, Dr. Kert Edward, Dr. Tanya Kerr, Dr. Samuel McDaniel, and Mr. Samuel Daniel for providing invaluable mentorship during my time at the University of the West Indies. May your kindness be extended to others who seek to traverse a similar path.

To Danielle McLean, Jonathan Smith, David Henlin, Davian Russell, and Donald Sutherland, the best group of friends one could ever ask for. Thanks for your companionship, accountability and support throughout my academic sojourn.

To Jeremy Lothian, for his unwavering support. Your many wise, and unbiased advise have steered me through many difficult times. Thanks for always having a listening ear, and for our friendship.

To Ely Diaz, Elsa Diaz, Jasen Hunt, Luis O'Donnell, Matt Smith, Micaiah Vargas, Nathan Henderson, and William Morris, for being excellent roommates.

To the Jamaican Students' Association, for providing a community in which I felt at home. May the organization continue to flourish as you continue to provide Jamaican students with a culturally-rich environment away from home.

To the Action Church, for providing a positive, wholesome environment for spiritual development and alignment. Thank you, and I trust that you will continue to have life-changing impacts.

I offer my heartfelt thanks and gratitude to all.

TABLE OF CONTENTS

LIST OF FIGURES	xiii
LIST OF TABLES	xxvii
CHAPTER 1: INTRODUCTION	1
1.1 Motivation	1
1.2 Background	2
1.2.1 Tuning Splashes	2
1.2.2 Punctured Fabrics	2
1.2.3 Intact Fabrics	4
1.2.4 Heterogeneous Spheres	6
1.2.5 Water Striders	8
1.2.6 Raindrop Impacts	10
1.3 Thesis Outline	12
CHAPTER 2: JET AMPLIFICATION AND CAVITY FORMATION INDUCED BY PEN- ETRABLE FABRICS IN HYDROPHILIC SPHERE ENTRY	14
2.1 Experimental Techniques	14

2.1.1	Impact Experiments	14
2.1.2	Surface Alteration	16
2.1.3	Splash Visualization	16
2.2	Experimental Results	16
2.2.1	Jet Height Control by Layered Fabric	17
2.2.2	Artificial Increase in Water Repellency	19
2.2.3	Fabric Increases Drag Force at Fluid Entry	22
2.3	Discussion	25
2.4	Chapter Summary	27
CHAPTER 3: MAKING A SPLASH WITH FABRICS IN HYDROPHILIC SPHERE EN-		
	TRY	28
3.1	Experimental Techniques	28
3.1.1	Impact Experiments	28
3.1.2	Material Property Measurements	30
3.2	Experimental Results	31
3.2.1	Fabric Properties Determine Cavity Shape	32
3.2.2	Greater Puncture Resistance Promote Higher Worthington Jets	33

3.2.3	Fabrics Amplify and Attenuate Hydrodynamic Drag	39
3.3	Discussion	43
3.4	Chapter Summary	45
CHAPTER 4: WATER ENTRY DYNAMICS OF SPHERES WITH HETEROGENEOUS WETTING PROPERTIES		46
4.1	Experimental Techniques	46
4.1.1	Impactor Surface Treatment	46
4.1.2	Impact Experiments	47
4.2	Experimental Results	49
4.2.1	Impactor Surface Treatments Modulate Splash Features	51
4.2.2	Surface Roughness and Orientation Determine Cavity Depths	54
4.2.3	Submerged Impactors Experience Lift and Drag	56
4.3	Discussion	60
4.4	Chapter Summary	63
CHAPTER 5: LIFE ON STORMY SEAS: WATER STRIDERS ARE IMPERVIOUS TO RAINDROP IMPACTS		64
5.1	Experimental Techniques	65

5.1.1	Insect Capture and Care	65
5.1.2	Impact Trials and Visualization	65
5.2	Experimental Results	67
5.2.1	Raindrop Collisions	68
5.2.2	Primary Cavity Formation	68
5.2.3	Primary Cavity Collapse and Worthington Jet Formation	71
5.2.4	Secondary Cavity Formation and Collapse	73
5.3	Discussion	74
5.4	Chapter Summary	76
CHAPTER 6: CONCLUDING REMARKS		77
APPENDIX A: SUPPLEMENTARY MATERIAL		79
A.1	JET AMPLIFICATION AND CAVITY FORMATION INDUCED BY PENETRA- BLE FABRICS IN HYDROPHILIC SPHERE ENTRY	80
A.1.1	Jet Height Control by Layered Fabric	80
A.1.2	Puncture Remains Constant	81
A.1.3	Fabric Increases Form Drag	82
A.1.4	Supplementary Movie Captions	83

A.2	MAKING A SPLASH WITH FABRICS IN HYDROPHILIC SPHERE ENTRY . . .	84
A.2.1	Material Property Measurements	84
A.2.2	Greater Puncture Resistance Promote Higher Worthington Jets	85
A.2.3	Smoothing Sphere Kinematics	85
A.2.3.1	Data Acquisition	85
A.2.3.2	Evaluating Derivatives	86
A.2.4	Supplementary Movie Captions	90
A.3	WATER ENTRY DYNAMICS OF SPHERES WITH HETEROGENEOUS WET- TING PROPERTIES	91
A.3.1	Surface Roughness and Orientation Determine Cavity Depths	91
A.3.2	Submerged Impactors Experience Lift and Drag	92
A.3.3	Supplementary Movie Captions	93
A.4	LIFE ON STORMY SEAS: WATER STRIDERS ARE IMPERVIOUS TO RAIN- DROP IMPACTS	94
A.4.1	Drop Impact Area	94
A.4.2	Supplementary Movie Captions	95
APPENDIX B: SCHOLARLY ACHIEVEMENTS		96
B.1	Journal Articles	97

B.2	Conference Papers	98
B.3	Conference Presentations	98
B.4	Research Symposium	99
B.5	Graduate Theses	100
APPENDIX C: VITA		101
C.1	Academic Training	102
C.2	Water Entry	102
LIST OF REFERENCES		104

LIST OF FIGURES

- Figure 1.1: Qualitative comparison of (a) hydrophilic and, (b) hydrophobic sphere impact on an unaltered surface. Penetrable, non-woven fabric alters entry dynamics of impacting hydrophilic spheres as seen by the inclusion of (c) one, and (d) four layers of fabric. Spheres have an impact velocity of $U = 2.2$ m/s. 3
- Figure 1.2: Cavity formation and splash features for hydrophilic sphere impacts onto an aqueous pool with interfacial entry zone modified by (a) no fabric, (b) Fabric A, (c) Fabric B, (d) Fabric C, and (e) Fabric D. Fabric alters entry dynamics, producing air-entraining cavities below the critical threshold velocity $U \approx 8$ m/s required for hydrophilic spheres [1]. Cavity depths are determined at the moment of seal between the fabric and trailing cavities. The fabric cavity depth is denoted by κ_f , and the length of the trailing cavity by κ_t . The top panel shows microscopic images of fabric weaves. The spheres pictured have diameter $D = 2.0$ cm, impact velocity $U = 3.13$ m/s, and $We = 2688$ 5
- Figure 1.3: Cavity formation and splash crown ascension for the water entry of a (a) fully hydrophilic sphere, (b) fully hydrophobic sphere, (c) heterogeneous sphere, $\alpha = 0.50$, $\beta = 0^\circ$; (d) heterogeneous sphere, $\alpha = 0.50$, $\beta = 90^\circ$; and (e) heterogeneous sphere, $\alpha = 0.50$, $\beta = 180^\circ$. Grey-shaded semi-circle indicates hydrophobic region and white-shaded area indicates hydrophilic region. Spheres pictured have diameter $D = 2.54$ cm and $We = 2014$ 7

Figure 1.4: (a) Adult water strider of order–Hemiptera; family–Gerridae; genus–Trepobates; species–*subnitidus*. Microscopic images showing (b) densely–packed macro-hairs along the leg of the water strider, and the (c) dorsal, and (d) ventral views of an adult’s exoskeleton. The exoskeleton is populated with both micro– and macro–hairs such that water contact angle exceeds 150° 9

Figure 1.5: (a) Water striders resting atop the free surface with torsal regions elevated, and fluid contact limited to superhydrophobic appendages. Some pelagic species spend their entire lives without contacting ground. (b) Striders submerged during cavity formation, and dispersed with the ascending splash crown after drop impact onto the free surface of a deep liquid pool. Corresponding video is Movie D1. (c) Temporal evolution of a drop impacting the quiescent liquid bath at $We \approx 2150$. Upon impact, an air-entraining cavity is generated simultaneously with the ascending splash crown. This sequence is followed by the ejection of a super-surface axisymmetric jet that subsequently recedes into the fluid. The retraction in-turn produces a secondary air-entraining cavity with a narrower expansion $\lambda_2 < \lambda_1$, and a more rapid collapse than the primary cavity. As such, a narrower, less voluminous secondary Worthington jet protrudes the free surface. Corresponding video is Movie D2. 11

Figure 2.1: (a) Experimental setup showing the Photron Mini AX-100 (Camera 1) for front views, and the Photron Mini UX-100 (Camera 2) for overhead views. (b) SEM image of the non-woven fibers comprising the fabric used in experiments. Fibers have a width of approximately $11 \mu\text{m}$. Impact outcomes for $We = 716$ on (c) an unaltered surface, and (d) a surface with a single layer of non-woven fabric, where the fabric is drawn upward by the protruding jet. 15

Figure 2.2: (a) Worthington jet height H_{max} versus Weber number We . The number preceding ‘ply’ denotes layers of fabric. The presence of fabric creates greater jet heights for We sufficient to penetrate the fabric plies. (b) Time-sequence of a 2.54-cm sphere impact from an overhead view for $We = 1580$. (c) Worthington jet height H_{max} versus sphere release height h . Filled symbols denote impacts onto clean water, while open symbols denote impacts onto 1-ply of fabric. Linear fits are applied to clean water impacts only with $R^2 = 0.931$ (2.54-cm linear fit), 0.9984 (2.20-cm linear fit), 0.766 (1.90-cm linear fit) and 0.995 (1.43-cm linear fit). The presence of fabric disrupts a linear progression of splash height, with $R^2 < 0.65$ for all spheres. 18

Figure 2.3: Diagrams depicting (a) the separation angle Θ , separation location ϕ , and impact wave height β , and (b) cavity width λ and depth κ for a cone-shaped quasi-static seal. Θ is measured from the location of flow separation ϕ and β is measured from the free surface. The relation between Weber number and the (c) separation angle Θ , (d) cavity depth κ , (e) cavity width λ , and (f) impact wave height β . Properties are non-dimensionalized in terms of the sphere diameter, $D = 2.20 \text{ cm}$ 20

Figure 2.4: Threshold velocity for cavity formation as a function of the advancing contact angle. For impacts onto clean water, spheres can be found in non-cavity forming region. The introduction of fabric increases separation angle, comparable to increasing θ_a , thereby shifting impacts into the cavity-forming region. . . . 22

Figure 2.5: (a) Temporal tracks of vertical position for impacting spheres with 0– to 4– layers of fabric atop the water. Trajectories are non-dimensionalized in terms of the sphere diameter, $D = 2.54$ cm. (b) Relation between the coefficient of drag C_d and the Reynolds number Re for impacting spheres with 0– to 4– layers of fabric atop the water. Addition of fabric increases drag on impacting spheres. 24

Figure 3.1: (a) Schematic of experimental setup. High-speed cameras capture frontal (Photron Mini AX–100) and overhead (Photron Mini UX–100) views with diffuse lighting positioned behind the tank. A wireless router enables multi-camera synchronization. (b) Sphere impact onto punctured (left) and intact (right) fabrics from an overhead view for $We = 2688$ 30

Figure 3.2: Fabric A. (a) Time-sequence of a 2–cm hydrophilic steel sphere impacting a single sheet for $We = 2688$ (Movie C2). Upon impact, a fabric-dependent cavity is formed and collapses near the free surface due to pressure imbalances. As sphere descend, a deeper, smoother, vertically-aligned cavity develops. The trailing cavity again pinches off and adds inertia to the retracting mass of fluid prior to the formation of a Worthington jet. (b) Non-dimensionalized fabric cavity depths κ_f/D versus Weber number We . (c) Non-dimensionalized Worthington jet height H_{max}/D versus Weber number We . (d) Non-dimensionalized trailing cavity lengths κ_t/D versus Weber number We . (e) Non-dimensionalized Worthington jet height H_{max}/D versus non-dimensionalized trailing cavity lengths κ_t/D 34

Figure 3.3: Fabric B. (a) Time-sequence of a 2–cm hydrophilic steel sphere impacting a single sheet for $We = 2688$ (Movie B3). Upon impact, a fabric-dependent cavity is formed and collapses near the free surface due to pressure imbalances. As sphere descend, a deeper, smoother, vertically-aligned cavity develops. (b) Non-dimensionalized fabric cavity depths κ_f/D versus Weber number We . (c) Non-dimensionalized Worthington jet height H_{max}/D versus Weber number We 35

Figure 3.4: Fabric C. (a) Time-sequence of a 2–cm hydrophilic steel sphere impacting a single sheet for $We = 2688$ (Movie B4). Upon impact, fabrics are pulled inward and form deep seal cavities, with pinch-off occurring close to spheres, typically $2/3$ the distance between spheres and the modified free surface. (b) Non-dimensionalized fabric cavity depths κ_f/D versus Weber number We . (c) Non-dimensionalized Worthington jet height H_{max}/D versus Weber number We 36

Figure 3.5: Fabric D. (a) Time-sequence of a 2-cm hydrophilic steel sphere impacting a single sheet for $We = 2688$ (Movie B5). Upon impact, fabrics are pulled inward and form deep seal cavities, with pinch-off occurring close to spheres, typically $2/3$ the distance between spheres and the modified free surface. (b) Non-dimensionalized fabric cavity depths κ_f/D versus Weber number We . (c) Non-dimensionalized Worthington jet height H_{max}/D versus Weber number We 37

Figure 3.6: (a) Aggregated plot of non-dimensionalized fabric cavity depths κ_f/D versus Weber number We for all fabrics on test. (b) Non-dimensionalized Worthington jet height H_{max}/D versus Weber number We for sphere impacts onto an unmodified free surface. (c) Aggregated plot of non-dimensionalized Worthington jet height H_{max}/D versus Weber number We for all fabrics on test. (d) Aggregated plot of non-dimensionalized Worthington jet height H_{max}/D versus non-dimensionalized fabric cavity depths κ_f/D for all fabrics on test. 39

Figure 3.7: (a) Non-dimensionalized vertical position versus dimensionless time. Trajectories are smoothed with a Savitzky-Golay filter to remove the effects of experimental error. (b) The relation between hydrodynamic drag coefficient C_D and instantaneous Reynolds number Re 42

Figure 4.1: (a) Schematic of experimental setup. High-speed cameras capture frontal (Photron Mini AX–100) and overhead (Photron Mini UX–100) views with diffuse lighting positioned behind the glass tank and above the frontal camera. Optional trigger switch complements manual controls in video recording software on computer. Wireless router enables multi-camera synchronization. (b) Threshold velocity U^* for cavity formation as a function of the advancing contact angle θ_a . Solid lines are theoretical predictions based on the seminal work of Duez *et al.* (2007) [1]. 48

Figure 4.2: (a) Temporal evolution of an air-entraining cavity and ascending splash crown for the water entry of a heterogeneous sphere, $\alpha = 0.50$, $\beta = 90^\circ$. A smooth cavity wall develops on the hydrophobic side of sphere, whereas a rough cavity wall envelopes the sphere along the hydrophilic hemisphere prior to cavity pinch-off. Cavity formation and splash crown ascension for the water entry of a half-coated hydrophilic sphere making impact across the range of (b) Weber numbers We and, (c) impact orientations β on test. Spheres have diameter $D = 2.54$ cm. We choose $We = 2014$ when iterating impact angles in (c). 50

Figure 4.3: Aggregated plots of cavity depths κ versus (a) $We^{1/2}$ and, (b) $(\alpha We)^{1/2}$. Cavities arising from the water entry of hemispherically-coated spheres may be described by $\kappa \sim (\alpha We)^{1/2}$ for low impact velocities, and $\kappa \sim We^{1/2}$ for increasing entry speeds. Cavity (b) depths κ , and (c) widths λ versus coated-sphere diameter αD for heterogeneous spheres with the line of demarcation parallel to the free surface at water entry. Spheres tested have impact velocity $U = 2.4$ m/s. 52

Figure 4.4: Spatiotemporal diagrams [2] showing water entry dynamics of a (a) fully hydrophilic sphere, (b) fully hydrophobic sphere, (c) heterogeneous sphere, $\alpha = 0.50$, $\beta = 0^\circ$; and (d) heterogeneous sphere, $\alpha = 0.50$, $\beta = 180^\circ$. The water entry dynamics of a heterogeneous sphere, $\alpha = 0.50$, $\beta = 90^\circ$ is shown in Figure 4.6. Spheres pictured have diameter $D = 2.54$ cm and $We = 2014$ 53

Figure 4.5: (a) Non-dimensionalized vertical y/D and (b) horizontal x/D positions versus dimensionless time. The point at which the sphere's center of mass makes contact with the free surface is chosen as $y/D = x/D = 0$. Vertical lines indicate the dimensionless time Ut/D at which cavity pinch-off occurs. (c) The relation between vertical C_{Fy} and (d) lateral C_{Fx} hydrodynamics force coefficients, and instantaneous Reynolds number Re . Spheres have an impact velocity of $U = 2.4$ m/s. 59

Figure 4.6: Spatiotemporal diagrams [2] showing water entry dynamics of a heterogeneous sphere, $\alpha = 0.50$, $\beta = 90^\circ$. Sphere trace gets thinner over time, and super-surface splash features appear lower in height than all other cavity-producing cases due to a skewed visual perception influenced by lateral sphere migration. Spheres have an impact velocity of $U = 2.4$ m/s. 60

Figure 4.7: Time-sequence of a 2.20-cm hydrophilic Delrin sphere impacting the edge of a single sheet of fabric for $We = 592$. Fabric thickness $\chi = 80 \mu\text{m}$, dry density $\rho''_{\text{dry}} = 2.88 \text{ mg/cm}^2$, wet density $\rho''_{\text{wet}} = 23.00 \text{ mg/cm}^2$, dry failure stress $\sigma_{\text{f,dry}} = 1.20 \text{ MPa}$, and wet failure stress $\sigma_{\text{f,wet}} = 0.09 \text{ MPa}$. Upon sphere impact, an asymmetric cavity originates at the three-phase point of contact with the fabric sheet and promotes lateral translation of sphere trajectory. As the sphere traverses the fluid downwards, force due to buoyancy F_B and drag \mathcal{D} oppose gravitational force W acting on the sphere, and lift force \mathcal{L} acts perpendicular to the velocity U , shifting the sphere laterally from its straight-line trajectory. 61

Figure 5.1: (a) Schematic of experimental setup. A Photron Mini AX-100 high-speed video-camera captures frontal views with diffuse lighting positioned behind the impact zone and above the camera. Optional trigger switch complements manual controls in video recording software on computer. (b) Plastron (air bubble) forms around water strider as syringe head pushes the insect beneath the free surface. Densely-packed micro- and macro-hairs populate the water strider exoskeleton such that water contact angle [3] exceeds 150° . Corresponding video is Movie D3. 66

Figure 5.2: (a) Drop impact incites cavity formation. Water striders behave as passive particles due to their low inertia, and are pushed downward a distance of several body lengths at the same speed as, and along the periphery of the expanding cavity. (b) Cavity expansion subsequent to drop impact. Cavities are tracked with sub-pixel accuracy of 180 pixel/cm at 3200 frames per second. (c) Cavity depth κ_1 , (d) velocity $u_{c,1}$, and (e) acceleration $a_{c,1}$ versus time. Cavity kinematics are unaltered by the presence of water striders along the cavity, and are representative of the displacement, velocity, and acceleration of a strider impacted by a drop. Drop impact pictured has $We \approx 2150$ 69

Figure 5.3: (a) Primary splash showing a free-falling drop approaching water striders atop the quiescent liquid bath. An air-entraining cavity and Worthington jet are formed after drop impact at $We \approx 2150$. The low mass of the water strider ensures resulting inertial forces are low, despite high impact accelerations, enabling the insect to survive the initial drop collision, while passively moving with the resulting splash. (b) Worthington jets are tracked with sub-pixel accuracy of 180 pixel/cm at 3200 frames per second. (c) Jet height δ_1 , (d) velocity $u_{j,1}$, and (e) acceleration $a_{j,1}$ versus time. Worthington jet kinematics are unaltered by the presence of water striders along the lamellae, and are representative of the displacement, velocity, and acceleration of a strider propelled above the free-surface. 71

Figure 5.4: (a) Secondary splash showing an adult water strider trapped within a gas-filled cavity, ejected with the ensuing Worthington jet, pushed subsurface along the cavity wall, and submerged by the rapidly collapsing cavity for $We \approx 2150$. Water striders with center of mass above the air-water interface of gas-filled cavities are propelled above the free surface with ascending secondary Worthington jets. In contrast, striders with center of mass below the air-water interface of cavities are left submerged due to the precipitous collapse of secondary cavities. Corresponding videos are Movies D4 and D1. (b) Secondary cavities are tracked with sub-pixel accuracy of 180 pixel/cm at 3200 frames per second. (c) Cavity depth κ_2 , (d) velocity $u_{c,2}$, and (e) acceleration $a_{c,2}$ versus time. 73

Figure A.1: Non-dimensional splash jet height H_{max}/D versus Weber number We . Splash heights non-dimensionalized in terms of the sphere diameter, D . The number preceding 'ply' denotes layers of fabric. The presence of fabric creates greater jet heights for We sufficient to penetrate the fabric plies. 80

Figure A.2: The relation between Weber number and the area of the puncture α . Area non-dimensionalized in terms of the sphere diameter, $D = 2.20$ cm. 81

Figure A.3: Relation between the non-dimensionalized form drag diameter $D^* = D_d/D$ and the instantaneous Reynolds number Re . Form drag diameter D_d is non-dimensionalized in terms of the sphere diameter, $D = 2.54$ cm. 82

Figure A.4: Stress-strain curves showing tensile strength of fabric sheets tested, in dry and wet states. Fabrics tested are (a) Georgia Pacific Compact Coreless 2-Ply Toilet Paper, Fabric A; (b) Kleenex Trusted Care Facial 2-Ply Tissue, Fabric B; (c) Georgia Pacific Sparkle Professional Series 2-Ply Perforated Roll Paper Towel, Fabric C; and (d) Darice Assorted Colors Tissue Paper, Fabric D. 84

Figure A.5: Non-dimensionalized Worthington jet height H_{\max}/D versus non-dimensionalized cavity depth κ/D for hydrophilic sphere impacts onto (a) Fabric A, (b) Fabric B, (c) Fabric C, and (d) Fabric D. Individual correlation values are given in Table 3.1 alongside best fit exponents according to $H_{\max} \sim \kappa_f^\alpha$. Variables are non-dimensionalized in terms of the sphere diameter D 86

Figure A.6: Non-dimensionalized temporal tracks of (a) vertical position $y(t)/D$, (b) instantaneous velocity $u(t)/U$, and (c) instantaneous acceleration $a(t)/g$ for a hydrophilic sphere traversing an aqueous pool after impacting the unmodified free surface. Sphere trajectory is non-dimensionalized in terms of the impact velocity $U = 3.13$ m/s, sphere diameter $D = 2.0$ cm and acceleration due to gravity $g = 9.81$ m/s. We apply different smoothing spans in the range $S = 0.1 - 1.0$ to determine the most suitable filter parameter which maintains the physical integrity of experimental data. (d) The relation between hydrodynamic drag coefficient C_D and instantaneous Reynolds number Re . We apply different smoothing spans in the range $S = 0.8 - 1.0$ to determine the most suitable filter parameter which maintains the physical integrity of experimental data. 87

Figure A.7: Non-dimensionalized temporal tracks of (a) vertical position $y(t)/D$, (b) instantaneous velocity $u(t)/U$, and (c) instantaneous acceleration $a(t)/g$ for a hydrophilic sphere traversing an aqueous pool after impacting the unmodified free surface. Sphere trajectory is non-dimensionalized in terms of the impact velocity $U = 3.13$ m/s, sphere diameter $D = 2.0$ cm and acceleration due to gravity $g = 9.81$ m/s. We apply different degree polynomials determine the most suitable filter parameter which maintains the physical integrity of experimental data, while fixing the span $S = 1.0$. (d) The relation between hydrodynamic drag coefficient C_D and instantaneous Reynolds number Re . We apply different degree polynomials determine the most suitable filter parameter which maintains the physical integrity of experimental data. 89

Figure A.8: (a) Measurements and linear fits of non-dimensionalized cavity depths κ/D versus Weber number We for the range of coating α and impact orientations β tested. Individual linear fit R^2 values are tabulated in the manuscript. Disaggregated plots with error bars are shown in (b)–(h). Cavities arising from the water entry of hemispherically-coated spheres may be described by $\kappa \sim (\alpha We)^{1/2}$ for low impact velocities, and $\kappa \sim We^{1/2}$ for increasing entry speeds. Variables are non-dimensionalized in terms of sphere diameter D 91

Figure A.9: Non-dimensionalized trajectories of heterogeneous spheres $\alpha = 0.33$, and $\alpha = 0.50$ with the line of demarcation perpendicular to the free surface at water entry. Trajectories are non-dimensionalized in terms of the sphere diameter, $D = 2.54$ cm, and have impact velocity $U = 2.4$ m/s. 92

Figure A.10 Impact area of an adult water strider. The strider's exoskeleton including the legs has impact area in the range $A_s = 34 - 165 \text{ mm}^2$. Impact area varies depending on drop size D , and is determined by first tracing the body of the strider with the desired drop. The area of the drop trace is then obtained graphically using ImageJ. Raindrop collisions within the impact area are considered as direct impacts. The water strider's legs account for 80% of the impact area, while the torso only accounts for 20%. During the heaviest rainfall [4, 5] with drops of mass $m = 16 \text{ mg}$, falling with an intensity [6] $I \approx 50 \text{ mm/h}$, a resting water strider will experience impacts on average every $\Delta t = m/(I \cdot \rho \cdot A_s) \approx 7 \text{ s}$, considering the entire impact area of the insect, and direct torsal impacts every $\Delta t \approx 34 \text{ s}$ 94

LIST OF TABLES

Table 3.1: Measured fabric properties and curve fitting correlation values. Curve fitting values for Fabric A corresponds to non-dimensionalized trailing cavity depths κ_t/D as the independent variable, and are thus shown in red to distinguish this uniqueness.	29
Table 3.2: Single-factor analysis of variance (ANOVA) test for cavity depths and jet height with respect to Weber number.	32
Table 4.1: Single-factor analysis of variance test for measured cavity depths κ with respect to $We^{1/2}$	55
Table 4.2: Hydrodynamic force coefficients at $Re = 69,000$	58

CHAPTER 1: INTRODUCTION

1.1 Motivation

Complex interactions between free-falling projectiles and deep liquid pools have marveled engineers for more than a century. The elegance of splashes, depth of fluid mechanics, and far-reaching applicability are unmatched. Splashes are worthy of our attention and still have much to teach us. The motivation for this body of work is both theoretical and experimental, and seek to determine new methods of tuning splashes by focusing on interfacial properties. Our experience with splashes occur daily, ranging from household activities to industrial processes. These splashes are often produced by the water entry of liquid drops and solid projectiles. The water entry of spherical impactors have been studied extensively since the seminal work of Worthington [7, 8, 9] in the late 19th century, and is relevant to applications in animal locomotion [10, 11, 12], aquatic sports [13, 14], sea-surface landing [15, 16], toilet dynamics [17, 18, 19], and missile water entry [1, 20, 21, 22, 23, 24, 25, 26]. The vast majority of water entry studies have been performed with impactors striking an unaltered, quiescent free surface, and with impactors having homogeneous wetting properties. However, surface homogeneity is not always possible when considering many real-life scenarios and much remains to be understood about water entry onto a modified free surface, and the water entry of impactors with heterogeneous wetting properties. Understanding the influence of surface heterogeneity on splash crowns, air-entraining cavities, and Worthington jets will lead to new engineering applications that mitigate unwanted splash exposure, control impactor deceleration, and modulate impactor trajectory in the milliseconds following free surface contact.

1.2 Background

1.2.1 Tuning Splashes

Traditionally, splashing and splash reduction have been investigated in the context of impactor shape, speed and wettability [1, 27, 26, 28]. Such studies are applicable to military and naval applications such as missile water entry, space vehicle sea surface landing, and industrial processes [29, 30]. In Chapter 2, we modify splashing characteristics without alteration of fluid or impactor properties, but by the placement of thin layers of penetrable fabric upon the surface of a liquid pool. Splash characteristics such as Worthington jets, air-entraining cavities, and radial splash crowns are dependent on surface tension, impactor wettability and velocity [1, 31]. The variance of these parameters for a desired splash outcome has been previously dubbed the ‘tuning of a splash’ [16]. Several studies modified surface tension and viscosity and showed jet height decreases with increasing viscosity whereas jet diameter is linearly proportional to the viscosity [16, 32, 33, 34]. Splash height may also be tuned by changing fluid depth, thereby influencing the amount of interaction of a collapsing cavity with the floor of a container [16]. When the impactor is a liquid droplet, splash height reaches a maximum when the pool depth is roughly 2X the droplet diameter, but attenuated when a sponge is affixed to the floor of the liquid pool [16]. Cavity pinch-off is delayed and its shape distorted by wall effects [35]. Pools deeper than cavities can be considered infinitely deep with respect to influencing splash mechanics. Here, we explore an alternate method for tuning a splash by altering fluid surface conditions in a deep pool.

1.2.2 Punctured Fabrics

Splash cavities have been extensively studied in the context of impactor shape [27], wettability[1], dynamics [22, 24, 36, 25], cavity shape [26], and pinch-off location. The formation of an air-

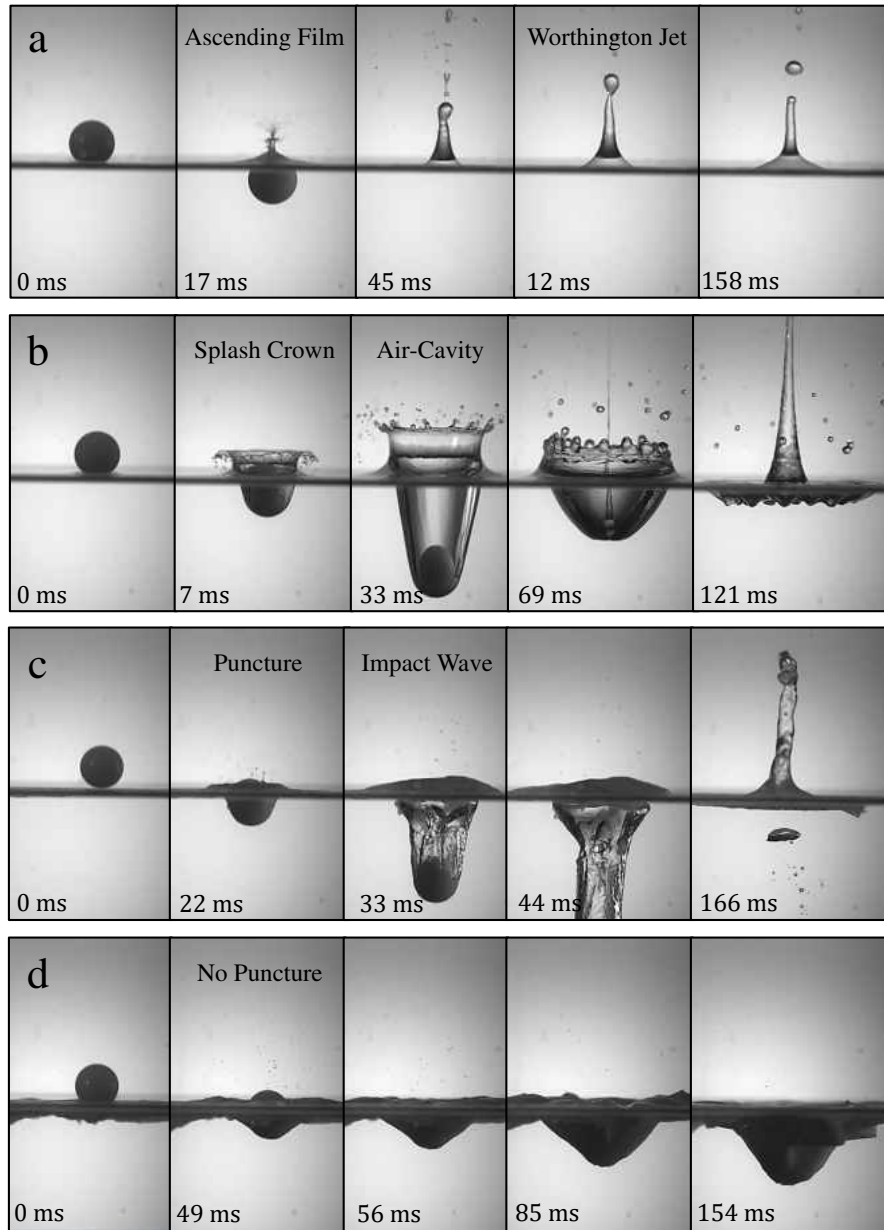


Figure 1.1: Qualitative comparison of (a) hydrophilic and, (b) hydrophobic sphere impact on an unaltered surface. Penetrable, non-woven fabric alters entry dynamics of impacting hydrophilic spheres as seen by the inclusion of (c) one, and (d) four layers of fabric. Spheres have an impact velocity of $U = 2.2$ m/s.

entraining cavity behind a solid impacting a liquid pool is greatly dependent on the hydrophobicity of the impactor [1, 37, 24, 38]. Hydrophobic impactors repel water upon entry to create cavities at

lower speeds than their hydrophilic counterparts. Water entry of hydrophilic spheres (Figure 1.1a) at entry velocities $U \lesssim 8$ m/s show minimal displacement of the fluid and no cavity formation [1, 24]. In Chapter 2, we consider the effect of a thin, penetrable fabric sitting atop a water surface on cavity formation.

Cavity forming splashes from spherical impactors typically include a well-developed dome rising above the surface whose periphery contains small jets that form an axisymmetric film [39, 16, 40, 37]. This splash crown grows prior to the development of the primary jet due to the ‘under-pressure’ and airflow behind the impactor. The maximum height attained by the splash crown is driven by inertial forces for Weber number $We = \rho U^2 D / \sigma \gg 1$, where ρ is the density of the fluid, D is the sphere diameter, and $\sigma = 72$ dyn/cm the surface tension [41]. In our observations, the presence of a thin penetrable fabric inhibits the ascension of a typical splash crown.

Chapter 2 provides the first documented application of a thin penetrable fabric atop a deep liquid pool to alter splash characteristics of vertically impacting hydrophilic spheres. Splashing sequences with clean water using hydrophilic and hydrophobic spheres can be seen in Figure 1.1a and Figure 1.1b respectively. A cavity-forming impact induced by one layer of penetrable fabric can be seen in Figure 1.1c. Four layers of fabric is impenetrable by the impacting sphere in Figure 1.1d, producing no Worthington jet.

1.2.3 *Intact Fabrics*

We explore the splash and cavity dynamics of water entry by again employing thin fabrics atop the water surface to reveal the physics at the transition between fabrics which are punctured and those remaining intact after impacts within the range of Weber number $We = 430 - 2700$. This work moves beyond our previous study [17] by employing a wider variety of surface modification by fabric, and by connecting fabric material properties to entry dynamics. Here, punctured fabrics

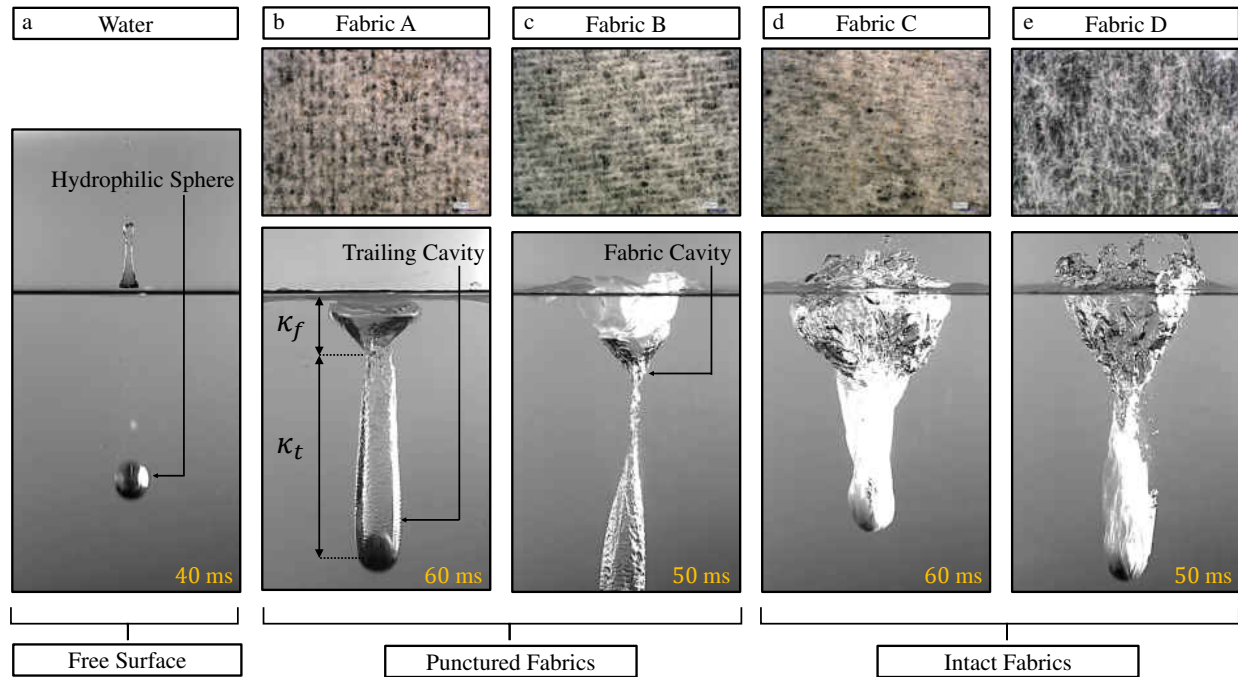


Figure 1.2: Cavity formation and splash features for hydrophilic sphere impacts onto an aqueous pool with interfacial entry zone modified by (a) no fabric, (b) Fabric A, (c) Fabric B, (d) Fabric C, and (e) Fabric D. Fabric alters entry dynamics, producing air-entraining cavities below the critical threshold velocity $U \approx 8$ m/s required for hydrophilic spheres [1]. Cavity depths are determined at the moment of seal between the fabric and trailing cavities. The fabric cavity depth is denoted by κ_f , and the length of the trailing cavity by κ_t . The top panel shows microscopic images of fabric weaves. The spheres pictured have diameter $D = 2.0$ cm, impact velocity $U = 3.13$ m/s, and $We = 2688$.

refer to those that are always torn by our impactors within the experimental range of We , while intact fabrics are not torn by impactors in our trials. Thus we relate splash dynamics to the resistance of fabrics to puncture. Our four chosen test fabrics are shown in Figure 1.2. Chapter 3 provides the first documented investigation on the influence of deformable fabric thickness χ , area density $\rho'' = \rho_f/A$, where ρ_f and A are the density and area of the fabric sheets respectively, and failure stress σ_f on cavity lengths, splash heights, and hydrodynamic drag coefficients.

1.2.4 *Heterogeneous Spheres*

The vast majority of water entry studies have been performed with impactors having homogeneous wetting properties. The water entry of purely hydrophilic spheres into a liquid bath generates minimal fluid displacement and no air-entrainment as pictured in Figure 1.3a, at entry speeds [1] below $U \approx 8$ m/s. Upon impact, a thin film of liquid travels radially upwards along the sphere's periphery, converging at the apex to form an asymmetric Worthington jet [17, 42] inversely proportional to the fluid's surface tension and viscosity at low Bond numbers [32, 33, 43, 44, 37]. Conversely, flow separation arising from the water entry of a cavity-producing impactor is shown in Figure 1.3b. Flow separation may be instigated by purely hydrophilic impactors without altering surface roughness or entry speeds. The water entry of spinning spheres [22]; placement of tiny droplets near the equator of free-falling hydrophilic spheres [45]; sphere impacts onto buoyant, non-woven fabric sheets placed atop the free surface [17, 18, 19]; and the water entry of heated spheres [14] at temperatures above the Leidenfrost temperature, all achieve flow separation at speeds [1] well below 8 m/s.

Recent studies show directional control of autonomous objects is possible without active propulsion, which warrants deeper investigation into impactors with heterogeneous wetting properties [46, 13, 47]. Few studies from the compendium of fluid engineering research have considered such impactors. One such study investigated the path of slender axisymmetric projectiles with heterogeneous surface treatments and elucidated the influence of the leading edge geometry and impact angle on impactor trajectory [46]. At impact velocities below 8 m/s, surface roughness destabilizes the three-phase contact line along hydrophilic surfaces to alter flow separation [13]. In contrast, the impact angle of partially-coated cylinders has a greater influence on their trajectories than surface roughness when inertial effects dominate water entry [13]. Tuning flow separation by way of surface treatment can also promote localized air-entrainment as observed during the wa-

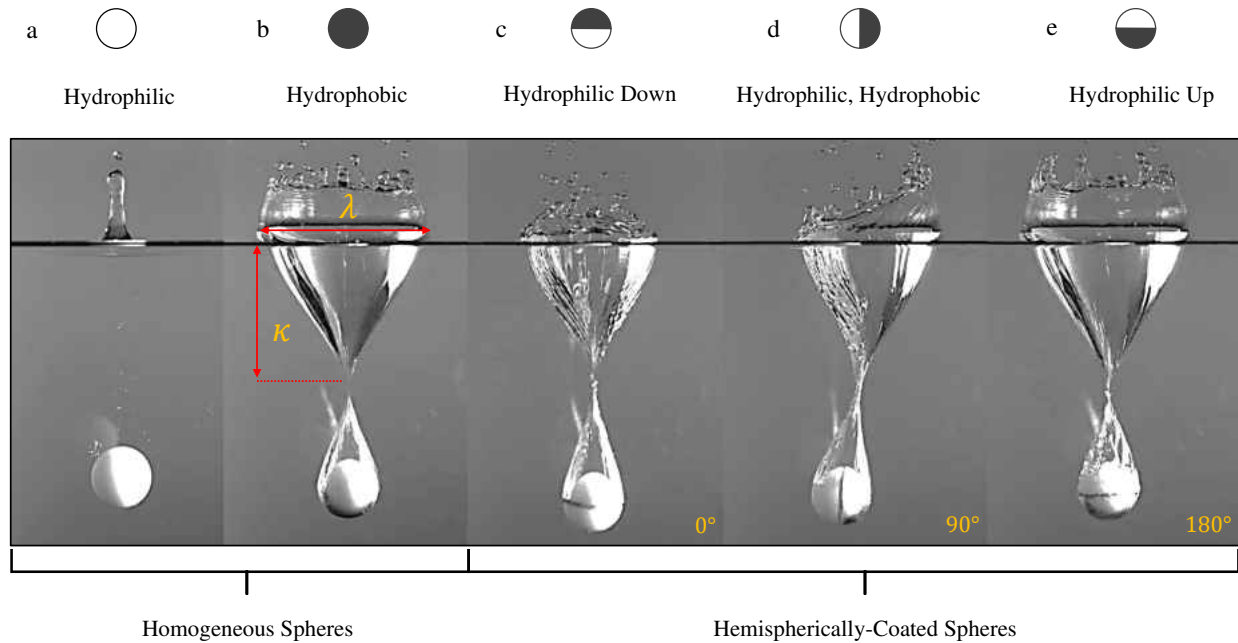


Figure 1.3: Cavity formation and splash crown ascension for the water entry of a (a) fully hydrophilic sphere, (b) fully hydrophobic sphere, (c) heterogeneous sphere, $\alpha = 0.50$, $\beta = 0^\circ$; (d) heterogeneous sphere, $\alpha = 0.50$, $\beta = 90^\circ$; and (e) heterogeneous sphere, $\alpha = 0.50$, $\beta = 180^\circ$. Grey-shaded semi-circle indicates hydrophobic region and white-shaded area indicates hydrophilic region. Spheres pictured have diameter $D = 2.54$ cm and $We = 2014$.

ter entry of stripe-coated hydrophilic cylinders [48], and hemispherically-coated spheres [22, 36]. These previous studies have not yet established the response of splash features to surface heterogeneity, given their focus primarily on impactor drag.

Chapter 4 provides the first systematic investigation of cavity depths, super-surface splash features, and sphere deceleration with respect to surface heterogeneity, in the range of Weber number $We = 591 - 3360$. Thus, we show splash dynamics during fluid entry are tunable by altering wetting properties along fractional portions of the impactor surface. A qualitative comparison of water entry for half-hydrophilic, half-hydrophobic spheres across varying impact orientations β is shown in Figure 1.3c–e. Half-cavities are produced when both the hydrophilic, and hydrophobic surfaces

make contact with the fluid simultaneously [22, 36]. As spheres descend at the relatively low impact velocities in our tests ($U \leq 3.13$ m/s), fluid separates downstream of the stagnation point along the hydrophilic surface while separating very near the stagnation point for the hydrophobic surface. Air-entrainment is thus biased toward the hydrophobic portion of hemispherically-coated spheres, effectively forming half-cavities. The pressure distribution [40] arising from this uneven cavity formation results in the lateral migration of a sphere from its straight-line trajectory [22, 36]. Numerical investigations of cavities generated by half-hydrophilic, half-hydrophobic spheres impacting quiescent fluids likewise support the confined nature of flow separation and adjustment to sphere trajectories [38].

1.2.5 Water Striders

Water striders account for approximately 0.0001% of total insect species [3], dwell and locomote atop the free surface of liquid bodies as shown in Figure 1.5a, and are the only insect group that completes a full life cycle in an aquatic environment [49, 50, 51], despite exposure to splashes during rainfall as pictured in Figure 1.5b (Movie D1). Some pelagic species spend their entire lives without contacting ground [52, 10, 11, 3]. The plan view of an adult water strider is pictured in Figure 1.4a. Oviposition typically occurs beneath floating vegetation, requiring nymphs to penetrate the air-water interface in the maturation process. Water striders are supported by surface tension given Baudoin number $Ba = Mg/\sigma L \ll 1$, where $M = 0.83$ mg \pm 0.17 mg ($N = 5$, young), and $M = 6.44$ mg \pm 1.50 mg ($N = 5$, adults) is the mass of the insect, $g = 9.81$ m/s² is acceleration due to gravity, $\sigma = 72.9$ mN/m is the surface tension of water, and $L \lesssim 5$ mm is the body length of the insect [53, 3]. This low magnitude of Ba suggests that the water strider can withstand multiple times its own body weight without sinking its legs, even though the strider's body is denser than water. Super-surface dwelling is further buttressed by the anti-fogging [54, 55, 56, 57, 58, 59, 3] characteristics of appendages (Figure 1.4b), and the superhydrophobic exoskeleton shown in Fig-

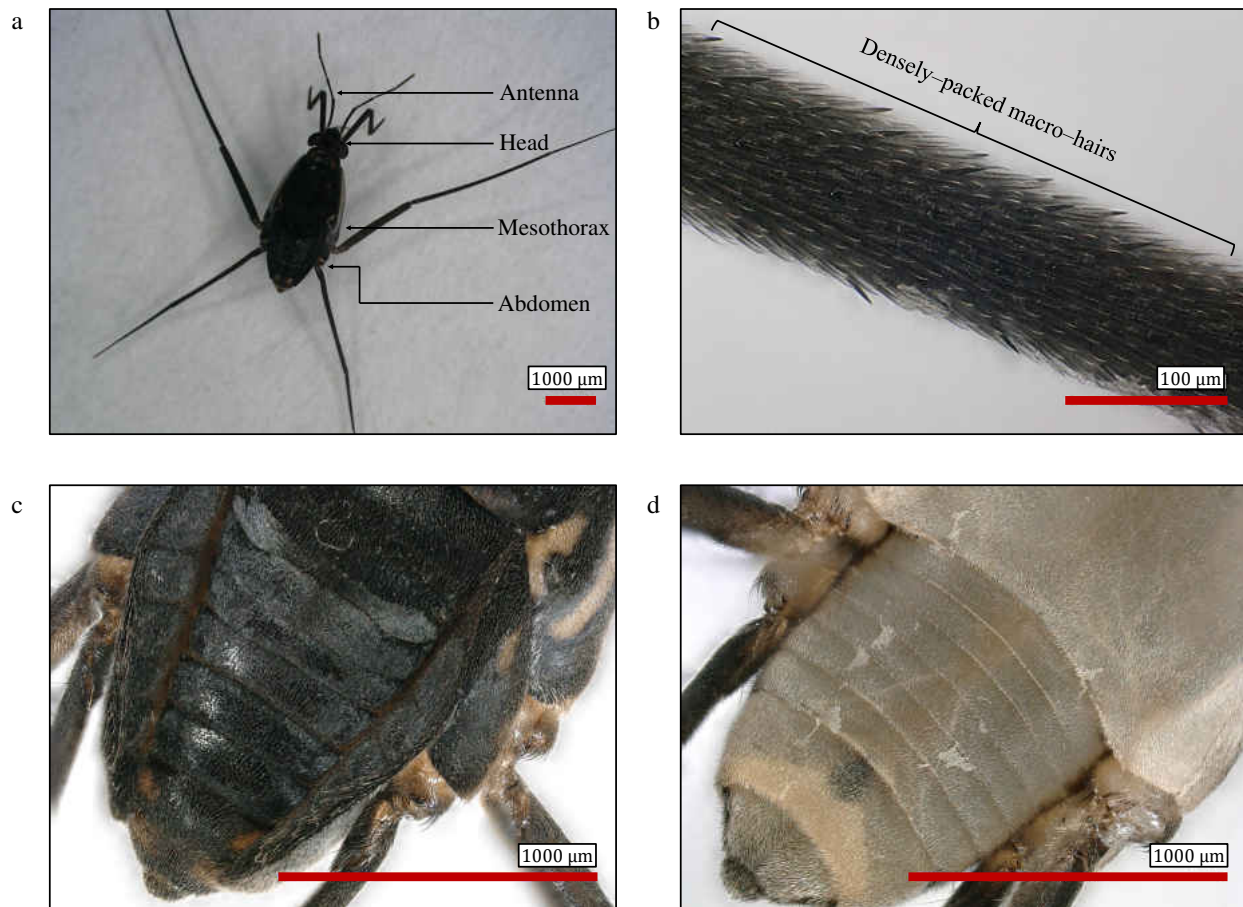


Figure 1.4: (a) Adult water strider of order-Hemiptera; family-Gerridae; genus-Trepobates; species-*subnitidus*. Microscopic images showing (b) densely-packed macrohairs along the leg of the water strider, and the (c) dorsal, and (d) ventral views of an adult's exoskeleton. The exoskeleton is populated with both micro- and macro-hairs such that water contact angle exceeds 150° .

ure 1.4c-dorsal view and Figure 1.4d-ventral view. The exoskeleton [54] is populated with both micro ($1.5 - 2.0 \mu\text{m}$ in long, $\sim 1 \mu\text{m}$ wide) and macro ($40 - 60 \mu\text{m}$ long, $3 \mu\text{m}$ wide) hairs such that water contact angle [3] exceeds 150° . During condensation tiny droplets form at the tip of the macro-hairs which are inclined 20° relative to the leg surface as shown in Figure 1.4b. As droplets grow, they move away from the tip and coalesce to spread adjacent hairs. When the diameter of droplets become comparable to the average distance between leg hairs such that deformation

occurs, droplets are expunged by the resulting elastic forces [59].

1.2.6 Raindrop Impacts

Marine environments experience some of the most violent storms Earth offers, resulting in surface perturbations that generate ripples and splashes, exposing water striders to the threats of saturation and submersion [60, 12, 3, 61]. The reaction of water striders to surface perturbation has been studied with respect to escape jumping atop deep liquid pools, but responses to direct impacts by drops are not yet understood [62, 63, 64, 65, 66, 12]. Rain consisting of water drops with diameter $D = 2 - 8$ mm, mass $m = 4 - 270$ mg and terminal velocity $U = 6 - 9$ m/s, is likely perceived by the water strider as the periodic deformation of the fluid surface [67, 6, 68]. In this combined experimental and theoretical study, we systematically investigate how such small, aquatic-dwelling creatures survive the onslaught of impacting drops at Weber number $We = \rho U^2 D / \sigma \approx 2150$, and Reynolds number $Re = \rho D U / \mu \approx 29,000$. The density of the drop and liquid water bath is $\rho = 999$ kg/m³, $U \approx (2 \cdot g \cdot h)^{1/2} = 6.01$ m/s ± 0.34 m/s ($N = 10$) is the drop velocity, $h = 1.75$ m is the height from which drops are released, $D = 4.34$ mm ± 0.04 mm ($N = 10$), and $\mu = 8.90 \times 10^{-4}$ Pa·s is the dynamic viscosity of water. Drops weigh $m = \rho V \approx 43$ mg, where $V = \pi D^3 / 6$ is the volume of the drop. A median drop size D is chosen such that our value of We is just beyond the range for light rain [61] $We = 15 - 2000$. Thus, we elucidate the robustness of water striders to adverse super-surface conditions during torrential downpour.

Free-falling drops striking an aqueous pool of similar fluid properties will coalesce with the receiving fluid, or create a splash [69, 39, 70, 71, 72, 73, 74] as shown in Figure 1.5b–c (Movie D2). Drops coalesce with the water bath when gently deposited onto the free surface ($We \lesssim 81$), while for increasing Weber number, drops create air-entraining cavities followed by the propulsion of super-surface axisymmetric jets that subsequently break up into secondary droplets due

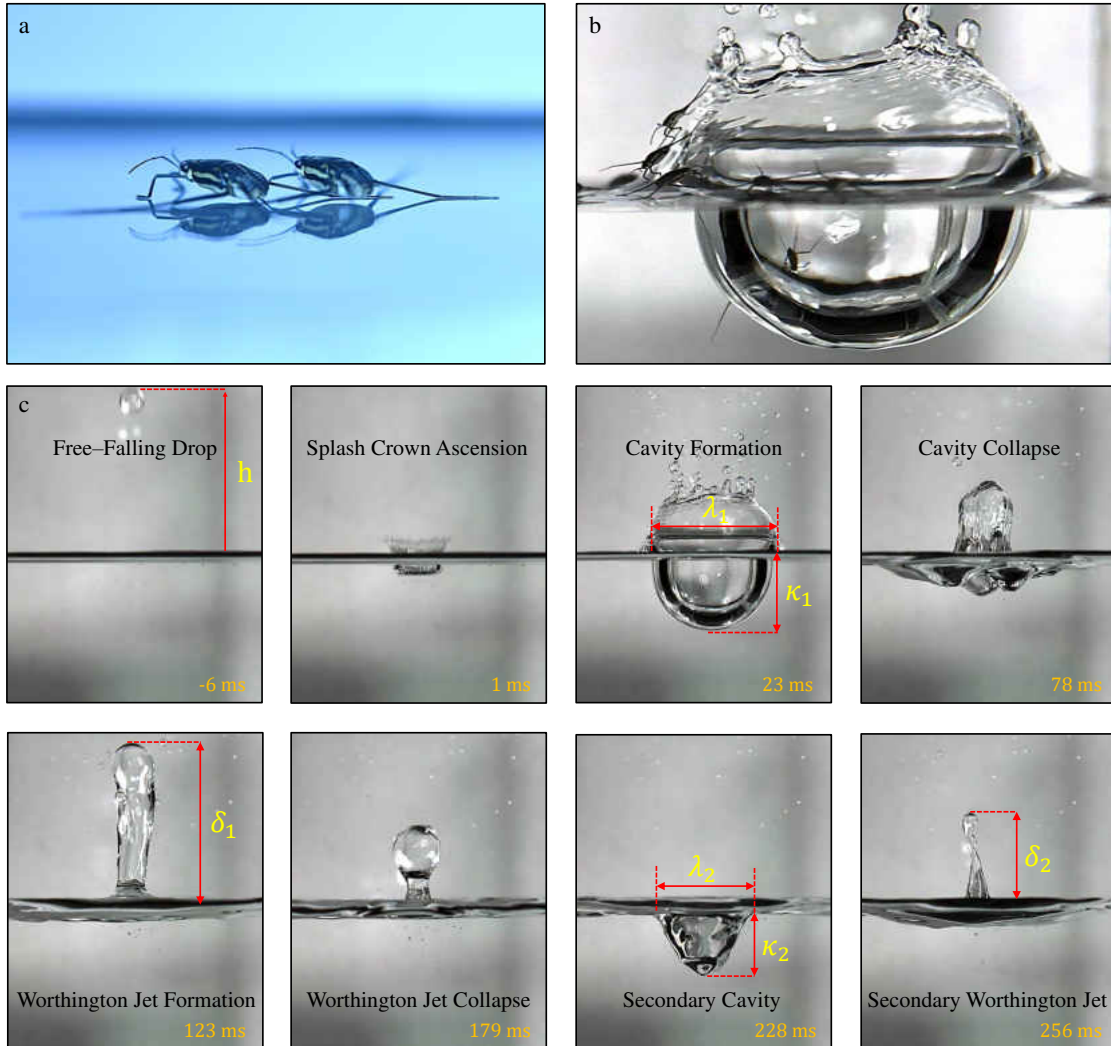


Figure 1.5: (a) Water striders resting atop the free surface with torsal regions elevated, and fluid contact limited to superhydrophobic appendages. Some pelagic species spend their entire lives without contacting ground. (b) Striders submerged during cavity formation, and dispersed with the ascending splash crown after drop impact onto the free surface of a deep liquid pool. Corresponding video is Movie D1. (c) Temporal evolution of a drop impacting the quiescent liquid bath at $We \approx 2150$. Upon impact, an air-entraining cavity is generated simultaneously with the ascending splash crown. This sequence is followed by the ejection of a super-surface axisymmetric jet that subsequently recedes into the fluid. The retraction in-turn produces a secondary air-entraining cavity with a narrower expansion $\lambda_2 < \lambda_1$, and a more rapid collapse than the primary cavity. As such, a narrower, less voluminous secondary Worthington jet protrudes the free surface. Corresponding video is Movie D2.

to Rayleigh-Plateau instabilities [75, 72, 76, 77, 73, 74, 17, 18, 19]. These droplets then strike the free surface and produce secondary air-entraining cavities and Worthington jets as pictured in Figure 1.5c for $t \geq 179$ ms. Given real-life drop interactions with water striders involve high-speed impacts, the mass ratios of raindrops to water striders, $m/M = 5 - 325$ for the young, and $m/M = 0.6 - 42$ for adults, suggest that striders should not survive raindrop collisions. To date, only a few studies from the compendium of bio-inspired engineering research have investigated the interaction between superhydrophobic insects and impacting drops. One such study showed mosquitoes surviving raindrop impacts by virtue of their low mass [6, 68]. Chapter 5 provides the first documented investigation on the physics involved in the splashing of semi-aquatic insects and particulate matter atop deep liquid pools.

1.3 Thesis Outline

In this body of work we investigate the influence of interfacial properties on the water entry dynamics of spherical projectiles ranging in size from 1-inch spheres for water entry experiments, to raindrops impacting water striders resting atop a liquid bath. We develop novel experimental and theoretical techniques to discover mechanisms by which splash characteristics such as the ascending splash crown, air-entraining cavity, and Worthington jet can be tuned. Most of this thesis is compiled from recent journal articles and preprints. Scientific journals publishing aspects of our work include *Physics of Fluids* [17], *Journal of Visualized Experiments* [18], and *Journal of Fluids and Structures* [19]. A manuscript portraying the results of Chapter 4 is currently under review. Our research has also been presented at numerous conferences hosted by the American Physics Society: Division of Fluid Dynamics [78, 79, 80] and the Society for Integrative and Comparative Biology [81]. The far-reaching dissemination and peer-reviewed critique of our work augurs well for our contribution to the compendium of fluid engineering research.

In Chapter 2, we begin with an experimental investigation of flow separation and splash metrics arising from the impacts of smooth, hydrophilic Delrin spheres with thin, non-woven fabrics resting atop a deep liquid pool. By considering pools of water with depths and widths many times the diameter of spheres on test, we mitigate the influence of floor [16] and wall [35] effects such that cavity expansion and Worthington jet formation are unabated. Flow separation is visualized using high-speed videography and splash metrics measured graphically. We give particular attention to evaluating sphere deceleration and the number of layered fabric sheets required to mitigate splash-back. In Chapter 3, we extend the study by again employing thin fabrics atop the free surface to reveal the physics at the transition between fabrics which are punctured and those remaining intact after impacts. Hydrophilic steel spheres of varying diameters and four commercial-grade household fabrics are employed in impact experiments.

In Chapter 4, we examine the water entry dynamics of spheres with heterogeneous wetting properties, otherwise referred to as ‘heterogeneous’ and ‘hemispherically-coated’ spheres. By studying spheres with alternating surface roughness, we show passive, lateral translation of projectiles only previously observed for the water entry of spinning spheres [22] and in cases where tiny droplets are placed near the equator of free-falling hydrophilic spheres [47].

In Chapter 5, we replace solid impactors with liquid drops to uncover the survival mechanisms of water striders during rainfall. Upon impact, the insect is pushed below the free surface along the cavity wall and subsequently ejected above surface with the ascending Worthington jet. Contact with the Worthington jet during descension pulls the strider beneath the free surface, at which point the insect may remain submerged, or is ejected, depending on its location along the secondary cavity. Analyzing these impacts incite new questions and research ideas, and warrant further investigations into drop impacts on floating particles. However, these investigations are extraneous to the scope of the current body of work and will be pursued beyond this thesis. In Chapter 6, we conclude by discussing the implications of our work and suggesting directions for future research.

CHAPTER 2: JET AMPLIFICATION AND CAVITY FORMATION INDUCED BY PENETRABLE FABRICS IN HYDROPHILIC SPHERE ENTRY

Previously published in *Physics of Fluids* [17].

Studies of solid impact with fluid surfaces have traditionally considered splashing in the context of impactor shape and surface texture. However, it is not always possible to tune impactor properties for desired splash characteristics. In this chapter, smooth, hydrophilic, free-falling spheres are allowed to impact a quiescent liquid surface for Weber numbers in the range of 400 – 1580. The liquid surface is modified by the inclusion of a thin fabric upon which a falling sphere strikes and penetrates at water entry. With respect to clean water, inclusion of a single layer of fabric on the surface increases Worthington jet height across all entry speeds tested. As the sphere penetrates, the fabric is drawn inward, providing a fabric funnel through which a Worthington jet subsequently passes. We show the presence of fabric increases the drag at entry and enables air-entraining cavities otherwise unattainable by hydrophilic spheres for the impact speeds tested. Such cavity formation is made possible by alteration of flow separation angle, analogous to greater values of advancing contact angle.

2.1 Experimental Techniques

2.1.1 Impact Experiments

We conduct impact experiments using a 20×20 cm² aquarium and four smooth Delrin spheres of masses 2.07, 4.90, 7.68, and 11.51 g and diameters of 1.43, 1.90, 2.20 and 2.54 cm respectively.

The contact angles of water on Delrin, both equilibrium $\theta_e = 78^\circ$ and advancing $\theta_a = 105^\circ$, are measured photographically, using a syringe to deposit water onto the sphere's surface. The release mechanism consists of a hinged platform suspended over the liquid pool (Figure 2.1a). Elastic bands rapidly retract the platform such that the spheres' motion is purely vertical, irrotational, and generates an impact velocity of $U \approx (2 \cdot g \cdot h)^{1/2}$, where $g = 9.81 \text{ m/s}^2$ is the acceleration due to gravity. We clean and dry spheres with 99% isopropyl alcohol before each trial to preclude the influence of impurities, and retrieve spheres from the pool with a sterile scoop.

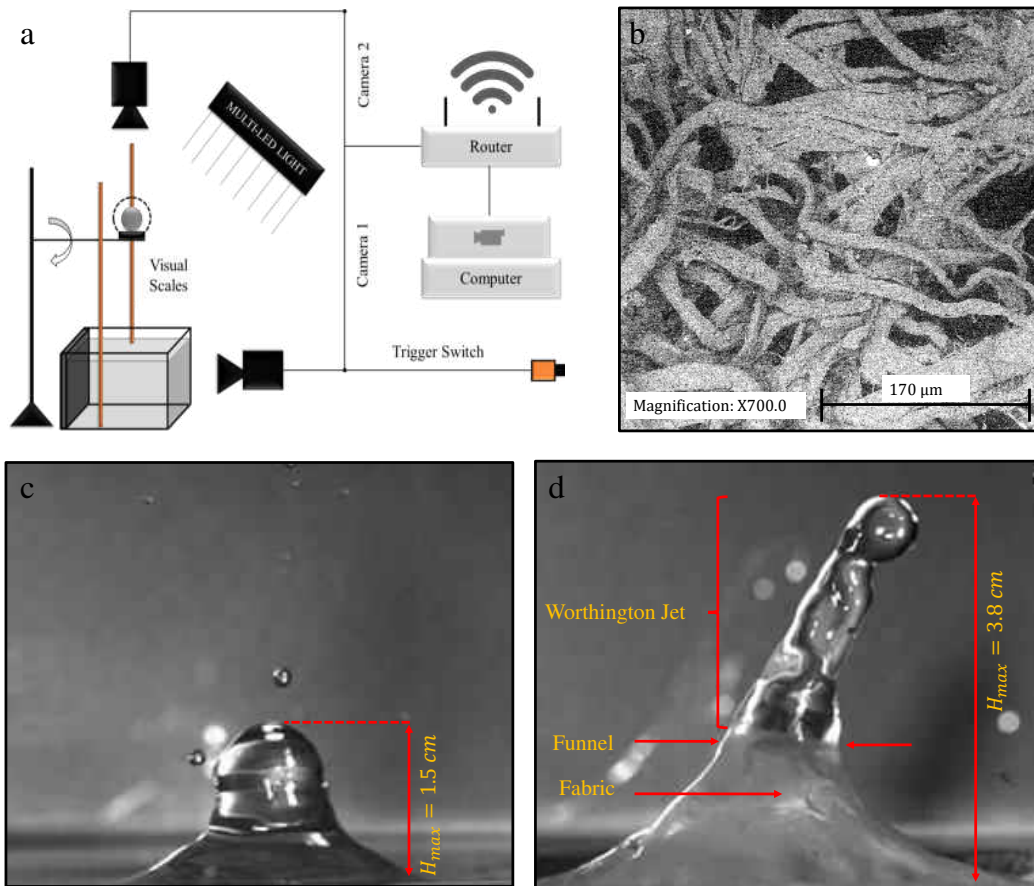


Figure 2.1: (a) Experimental setup showing the Photron Mini AX-100 (Camera 1) for front views, and the Photron Mini UX-100 (Camera 2) for overhead views. (b) SEM image of the non-woven fibers comprising the fabric used in experiments. Fibers have a width of approximately $11 \mu\text{m}$. Impact outcomes for $We = 716$ on (c) an unaltered surface, and (d) a surface with a single layer of non-woven fabric, where the fabric is drawn upward by the protruding jet.

2.1.2 *Surface Alteration*

For surface alteration, we use Georgia Pacific Compact coreless toilet paper with a compressed thickness of $\sim 80 \mu\text{m}$ and comprised of chopped fibers $11 \mu\text{m}$ in diameter, shown in the SEM image of Figure 2.1b. We gently rest square plies ($\rho = 0.355 \text{ g/cm}^3$, dry) atop the water such that the impacting sphere will strike the approximate center of the ply. The paper rests slightly subsurface due to the volumetric absorption of water, and does not dissolve, breakup, or otherwise soil water during trials. Each drop condition is repeated at least 5 times to reduce the influence of experimental inconsistencies and water absorbed by the fabric replenished before each trial. The entire volume of the bath was replaced at least once daily.

2.1.3 *Splash Visualization*

We film impacts with a Photron Mini AX–100 high-speed camera at 1000 frames per second using a 55–mm Nikor lens (Figure 2.1a). In select trials, a Photron Mini UX–100 high-speed camera is added to the experiment to provide a top-down view of impacts on the fabric. We extract kinematic and geometric measurements from videos using Tracker, an open source image analysis software. When reporting splash height H_{max} , we consider the tallest point of the coherent Worthington jet, and not satellite droplets, as demonstrated in Figure 2.1c–d.

2.2 Experimental Results

We impact a thin penetrable fabric atop the surface of a deep pool of water with four hydrophilic spheres from various heights and compare changes in the splashing dynamics with respect to an unaltered, clean surface. Spheres strike the center of a $10.5 \times 10.5 \text{ cm}$ square, and tear through the fabric at sufficiently high speeds. We observe the presence of the fabric results in changes to

splash height, cavity formation, and a splash crown.

2.2.1 Jet Height Control by Layered Fabric

We begin by measuring splash heights for hydrophilic spheres impacting clean water, as seen in Figure 2.2a. For the range of $We = 400 - 1580$ tested, we observe splashes are on average amplified by the inclusion of a single ply, or layer, of fabric onto the splash domain, and amplified by the inclusion of a double-layer of paper for $We > 800$. With three and four layers, the sphere does not penetrate the fabric for $We < 1100$ and $We < 1500$ respectively, and results in slower entry and no Worthington jet, represented by the points lying on the axis in Figure 2.2a. A plot of H_{\max}/D vs. We is shown in Figure A.1.

A pictorial comparison of the Worthington jet resulting from 0- and 1-ply of fabric for $We = 716$ is shown in Figure 2.1c-d. As expected with no fabric present, the hydrophilic Delrin sphere produces an axisymmetric Worthington jet and no cavity (Movie A1). With the inclusion of fabric, an air-entraining cavity follows the sphere, so long as the sphere penetrates the fabric (Movie A2). As the cavity retracts, the jet propagates through the hole torn in the fabric by the passing sphere as seen in Figure 2.1d and Figure 2.2b, resulting in amorphous jets (Movie A3) that are narrower for higher numbers of fabric plies. In some cases, this action results in greater jet heights, as evidenced by the rightmost points of Figure 2.2a.

As seen in Figure 2.2a, splash height increases with We . For the range of $Re = 17,000 - 54,000$ tested, inertial effects dominate viscous effects for impacts absent of fabric. In the limit of an inviscid fluid, the kinetic energy of the impacting sphere $E_{k,s} = \rho_s V_s g h$ will be converted to potential energy of the jet $E_{p,j} = \rho g V_j H_{\max}$ where ρ_s and V_s are the density and volume of the sphere

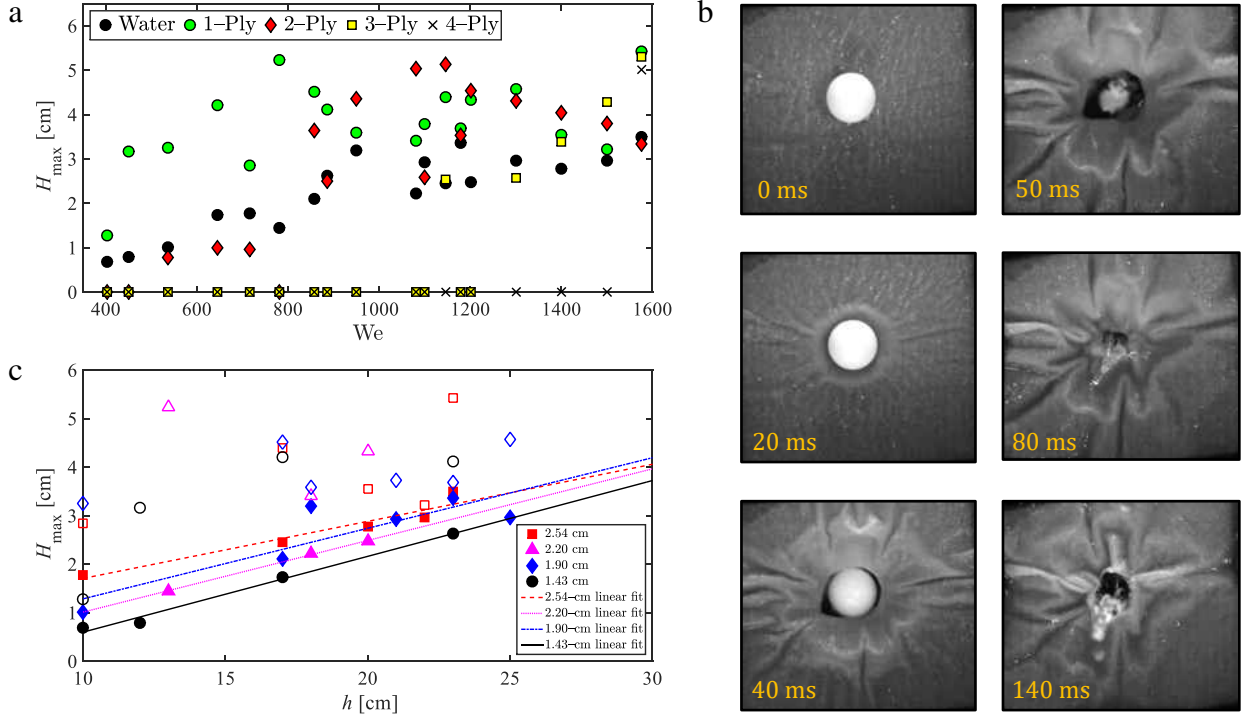


Figure 2.2: (a) Worthington jet height H_{\max} versus Weber number We . The number preceding ‘ply’ denotes layers of fabric. The presence of fabric creates greater jet heights for We sufficient to penetrate the fabric plies. (b) Time-sequence of a 2.54–cm sphere impact from an overhead view for $We = 1580$. (c) Worthington jet height H_{\max} versus sphere release height h . Filled symbols denote impacts onto clean water, while open symbols denote impacts onto 1–ply of fabric. Linear fits are applied to clean water impacts only with $R^2 = 0.931$ (2.54–cm linear fit), 0.9984 (2.20–cm linear fit), 0.766 (1.90–cm linear fit) and 0.995 (1.43–cm linear fit). The presence of fabric disrupts a linear progression of splash height, with $R^2 < 0.65$ for all spheres.

respectively, and V_j is the volume of the jet. Accordingly,

$$\rho_s V_s g h \sim \rho V_j g H_{\max}. \quad (2.1)$$

Although not tested, we expect that $V_j \sim V_s$. When an hydrophilic sphere strikes the fluid, an ascension film spans the diameter as seen in Figure 1.1a. With this assumption and noting that

$\rho_s/\rho = \text{constant}$ in our experiments, Eq.(2.1) becomes

$$H_{\max} \sim h. \quad (2.2)$$

The linear relationship predicted by Eq.(2.2) is confirmed by the filled points in Figure 2.2c for impacts onto clean water. We find disruption of this linear trend by the addition of fabric.

2.2.2 Artificial Increase in Water Repellency

The application of the thin fabric atop the water surface not only amplifies jet height with respect to hydrophilic impactors on clean water, but also facilitates the formation of an air-entraining cavity (Movie A4). The fabric alters separation characteristics (angle Θ and location ϕ) as defined in Figure 2.3a, due to prevention of the ascending film seen in Figure 1.1a, such that the water cannot flow toward the top of the sphere. The resulting flow separation is characteristically similar to impactors that have greater advancing contact angles [1], θ_a , inducing separation through hydrophobicity alone.

We vary the drop height and observe the punctured fabric acting as a barrier between the sphere and fluid as subsurface cavities develop. An increase of this separation angle Θ from a low of 143° , $We = 716$ to a high of 151° , $We = 1441$ can be seen in Figure 2.3c using a sphere of fixed $D = 2.20$ cm and 1-ply of fabric. The increase in Θ with U indicates the impactor produces steeper cavity walls, overcoming the tensile influences of the fabric with greater momentum values. Cavities formed by this process are characterized as quasi-static seals as pinch-off occurs at or near the sphere [21, 26]. After about 60 ms, the sphere exits the cavity which retracts, leading to the formation of the primary Worthington jet.

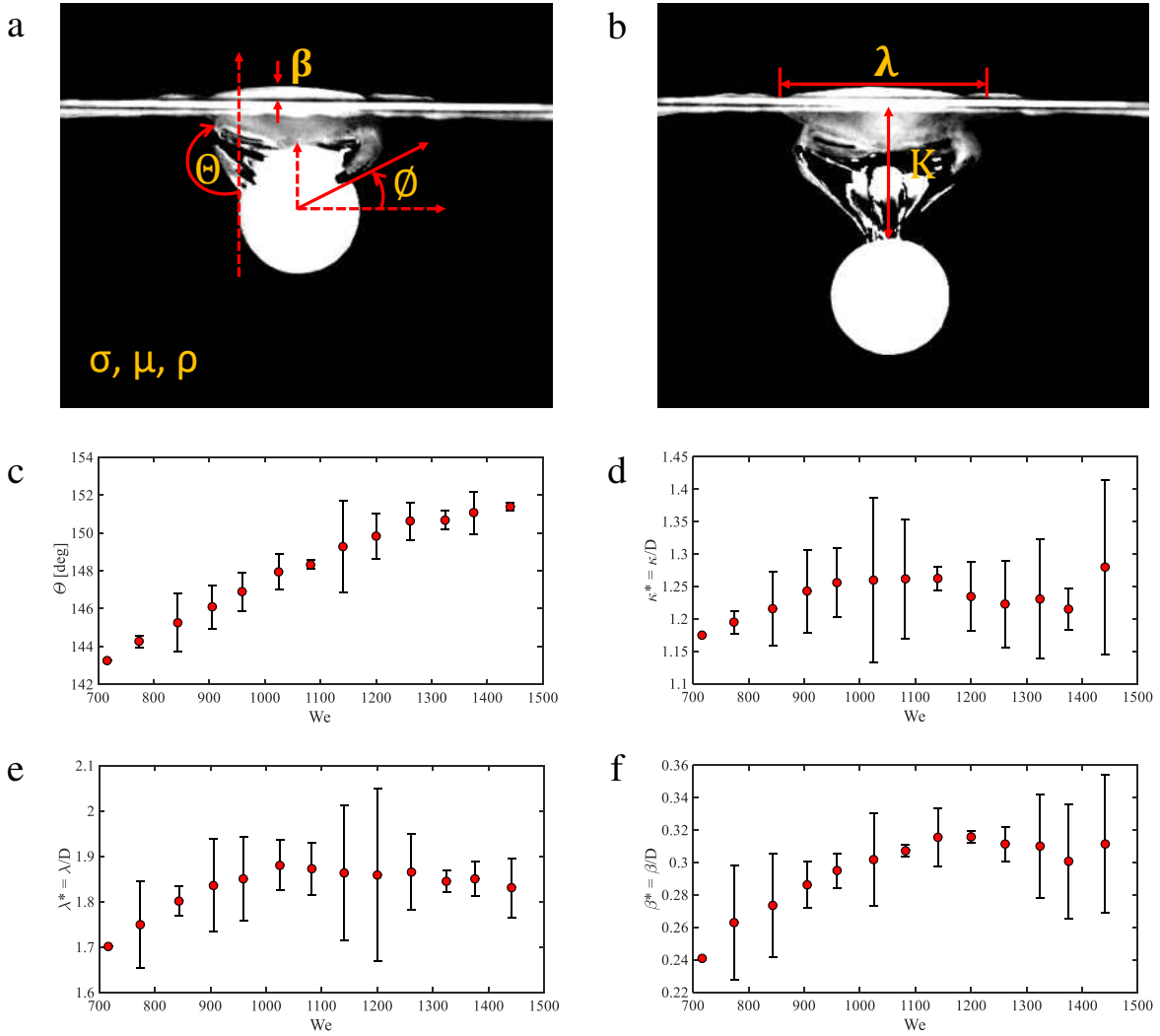


Figure 2.3: Diagrams depicting (a) the separation angle Θ , separation location ϕ , and impact wave height β , and (b) cavity width λ and depth κ for a cone-shaped quasi-static seal. Θ is measured from the location of flow separation ϕ and β is measured from the free surface. The relation between Weber number and the (c) separation angle Θ , (d) cavity depth κ , (e) cavity width λ , and (f) impact wave height β . Properties are non-dimensionalized in terms of the sphere diameter, $D = 2.20$ cm.

Across the range of experimental We , we find dimensions of cavities created by a sphere of fixed $D = 2.20$ cm and 1-ply of fabric show little variation. The non-dimensional cavity depth $\kappa^* = \kappa/D$ increases by less than 8% and non-dimensional cavity diameter $\lambda^* = \lambda/D$ increases by less than 15% with increasing We , as seen in Figure 2.3d–f. The existence of an impact wave (Figure 1.1d)

is a result of the inhibition of a splash crown by the fabric. We likewise measure little change in the non-dimensional impact wave height $\beta^* = \beta/D$ as We increases. The weak dependence of cavity size to U is rationalized by noting that after the sphere ends contact with the fabric, its hydrophilic nature prevails, such that the sphere is no longer able to propagate the cavity further. Therefore, we posit that cavity properties are only a strong function of sphere size. For an unaltered surface a cavity forming impact must exceed a critical velocity U_c given by [1]

$$U_c = \begin{cases} \varepsilon\sigma/\mu & \text{if } \theta_a \leq 90^\circ \\ \psi\sigma[\pi - \theta_a]^3/9\mu & \text{if } \theta_a \geq 90^\circ \end{cases} \quad (2.3)$$

where $\varepsilon = 0.1$ and $\psi = 7/30$ are numerical pre-factors set to match previous results [1]. The solid curve in Figure 2.4 represents the value of U_c for unaltered conditions and corresponds to 8.1 m/s, $We = 23,763$, for $\theta_a \leq 90^\circ$ and $\mu = 0.89$ cP. The onset of cavity formation [1, 26] for spherical impactors can be accomplished by either an increase in θ_a or μ . For the case of fabric placement onto the impact plane, we have an increase in separation angle, which has the same dynamical effects as an increase in θ_a which provokes cavity formation over the range of U on test.

The circle in Figure 2.4 shows the impacting Delrin sphere firmly outside the cavity-forming region, consistent with our experiments with 0-ply. This sphere can be found inside the cavity-forming region by conservatively setting $\theta_a = \Theta$ as denoted by the square in Figure 2.4, the result of impacting 1-ply of fabric. We note that in trials with a hydrophobic sphere with $\theta_a = 135 \pm 3^\circ$ impacting clean water (0-ply), the separation angle $\Theta = 168 \pm 1^\circ$, $N = 6$.

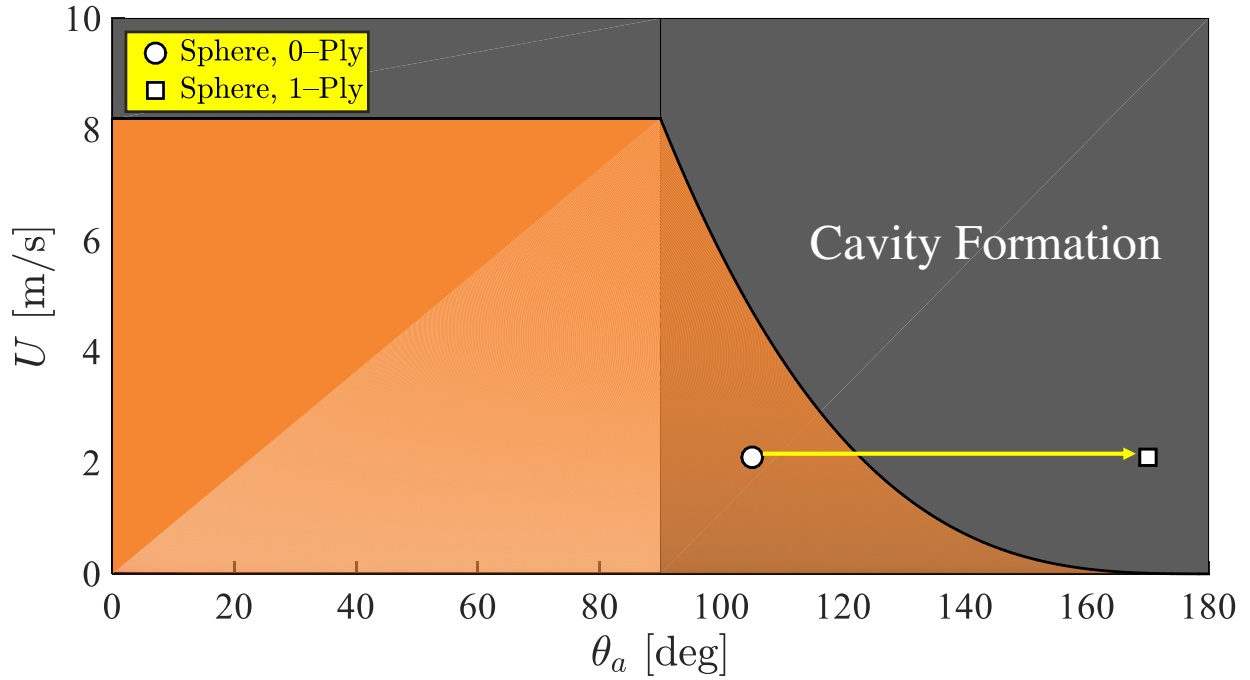


Figure 2.4: Threshold velocity for cavity formation as a function of the advancing contact angle. For impacts onto clean water, spheres can be found in non-cavity forming region. The introduction of fabric increases separation angle, comparable to increasing θ_a , thereby shifting impacts into the cavity-forming region.

2.2.3 Fabric Increases Drag Force at Fluid Entry

The presence of penetrable fabric plies increases drag force at entry. We determine the additional drag force from the addition of fabric layers by tracking the position of a 2.54-cm diameter sphere released from 24 cm as it impacts the liquid/fabric interface as seen in Figure 2.5a. A force balance for a sphere of mass m falling vertically into a quiescent liquid bath is given by,

$$(m + m_a)a = mg - F_B - F_D, \quad (2.4)$$

where a is the acceleration of the sphere. The buoyant force due to hydrostatic pressure $F_B =$

$\rho g \left(\frac{\pi}{12} D^3 + A(y)y \right)$, where y is the coordinate into the fluid depth, and $A(y)$ is the wetted area of the sphere entering the bath. This form of buoyant force follows conventions established by previous work [24] and assumes the cavity adjoins the equator for simplicity. For further simplification, we treat buoyant force as constant such that

$$F_B = \rho g \pi \left(\frac{D^3}{12} + \frac{D^2 \kappa}{4 \cdot 2} \right), \quad (2.5)$$

where we treat $\kappa = D$ according to Figure 2.3d. In our experiment and model, we consider only the period of time the sphere is interacting with the fabric and maintains an air-entraining cavity. Drag force [24, 82, 83] is given by $F_D = \pi \rho D^2 C_D u^2 / 8$, where C_D is the drag coefficient and $u = u(t)$ is the time-varying velocity. The effect of accelerating fluid by the falling sphere is accounted for by the added mass $m_a = \pi \rho D^3 C_m / 6$, where $C_m = 0.5$ is the added mass coefficient, treated as constant [24, 25] across all cases. It is noteworthy that our model is not sensitive [24] to the value of C_m . Eq.(2.4) can be rewritten as

$$m' a = mg - \frac{5}{24} \rho g \pi D^3 - \frac{1}{8} \rho \pi D^2 C_D u^2, \quad (2.6)$$

where $m' = m + m_a$. We transform Eq.(2.6) into a first order non-linear differential equation. Accordingly,

$$\frac{du}{dt} = \frac{mg}{m'} - \frac{\rho g \pi D^2}{8m'} \left(\frac{5}{3} D + \frac{C_D}{g} u^2 \right). \quad (2.7)$$

We smooth position track data with a Savitzky-Golay filter [84] (Figure 2.5a) to remove the effects of experimental error prior to numerical differentiation. The resulting velocity curves, $u(t)$, are

again smoothed prior to a second and final numerical differentiation, providing du/dt . Using Eq.(2.7), we solve for values of C_D , which are plotted against instantaneous Re in (Figure 2.5b). Greater numbers of fabric plies slow the sphere's motion more rapidly and result in greater values of C_D .

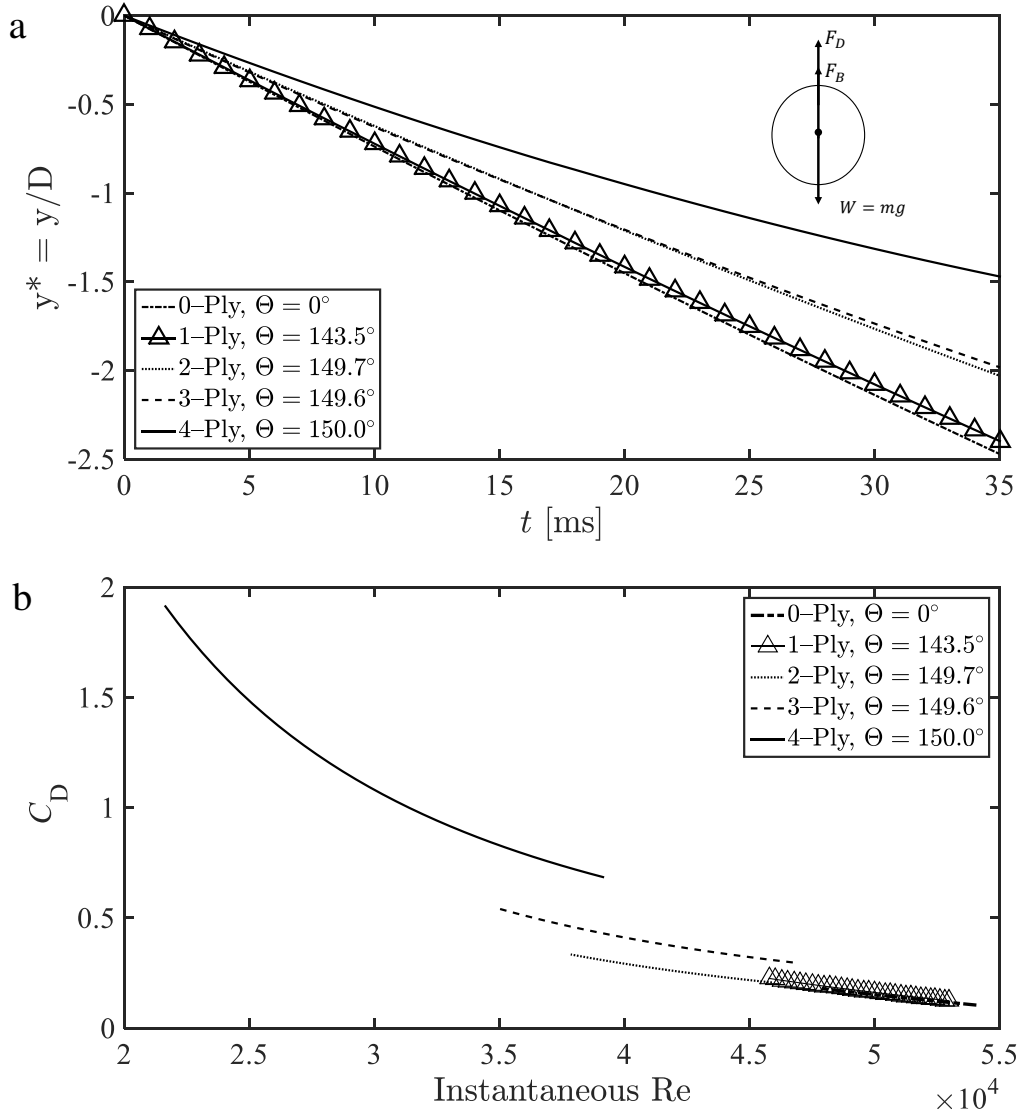


Figure 2.5: (a) Temporal tracks of vertical position for impacting spheres with 0- to 4- layers of fabric atop the water. Trajectories are non-dimensionalized in terms of the sphere diameter, $D = 2.54$ cm. (b) Relation between the coefficient of drag C_d and the Reynolds number Re for impacting spheres with 0- to 4- layers of fabric atop the water. Addition of fabric increases drag on impacting spheres.

The average values of $C_D = 0.14, 0.17, 0.26, 0.40,$ and 1.15 for 0-, 1-, 2-, 3- and 4-plyes respectively. By treating C_D as constant throughout the duration of impact, we can solve for an equivalent change in sphere diameter D_d , increasing form drag, that corresponds to each impact scenario. We include a plot of a non-dimensionalized form drag diameter $D^* = D_d/D$ vs. instantaneous Re in Figure A.3.

2.3 Discussion

Our study shows that vertical impacts by hydrophilic spheres on a thin fabric placed atop a deep pool of water experience amplified jet heights and cavity formation, as compared with pure water. In our observations, these behaviors exist only when spheres penetrate the fabric. Those impacts which do not penetrate fabric sit on the axis in Figure 2.2a and do not achieve a sufficient impact momentum to create a cavity. For these non-penetrating impacts the theoretical considerations discussed in §2.2.2 do not apply. The reaction of spheres to 3- and 4-plyes of fabric at $We < 1500$ we expect are qualitatively similar to using any thickness woven fabric, which maintain their tensile integrity when wet.

When using fabric to allay splash-back, it is imperative that falling objects are unable to puncture the fabric, either by excessive layering or sufficient tensile strength. Though we made no attempt to customize the height of Worthington jets, careful selection of fabric may enable tunable jet height with this method. However, as evidenced by Figure 2.2c it is unknown how fabric properties affect splashing dynamics. We rationalize disruption to our splash height scaling prediction of Eq.(2.2) by the unpredictable nature of energy dissipation imposed by fabric at impact. The spheres' kinetic energy is converted to tearing and mobilizing the fabric, and creating a cavity (Figure 2.2b).

The ability to continue to draw inward after sphere passes enables the narrowing of the Worthington

jet. A sheet of fabric which has a much greater area will possess sufficient inertia to prohibit mobilization towards the puncture, while a sheet approaching the diameter of the sphere will have insufficient material to remain wider than λ . In either case, we expect wider jets. Likewise, in cases where a fluid surface coating is stiff and cannot retract towards a puncture, if the surface is covered by a thin sheet of ice for example, we expect wider jets. The sensitivity of jet characteristics to fabric size and mobility is therefore an area requiring further investigation.

Fabrics which are functionally impenetrable by impacting spheres, but impacted at higher We than reported in Figure 2.2a form cavities and splash, as seen in Movie A5. In these cases, the falling sphere will have sufficient momentum to fully submerge a fabric sheet. In doing so, the edges of the sheet generate the most dominant splashing feature. The properties of fabric and sphere for such a transition from non-splashing to splashing is an avenue of further study. In this study we were not concerned with fabric elasticity, which will likewise affect impact dynamics and fabric puncture. Accordingly, the transition between a penetrated and intact fabric, and how this transition is related to fabric strength, elasticity, and sphere dynamics is a topic of future consideration.

Fabric sheets with precut holes larger than the impacting sphere allow passage as if not present, producing a splash characteristic to that seen in Figure 1.1a, so long as the sphere does not contact any portion of the fabric at entry. We provide an example in Movie A6 with a precut circle with diameter $3D/2$. In this case, there is no evident mobilization of the fabric. In the case where the precut is smaller than the sphere diameter, interaction with the fabric produces a cavity at entry, similar to the impact depicted in Figure 1.1c. We provide an example of such an impact in Movie A7, where the precut hole has diameter $D/2$.

2.4 Chapter Summary

Here we have shown hydrophilic spheres impacting a thin layer of penetrable fabric atop a water bath experience Worthington jet height amplification and air-entraining cavities for Weber numbers 400 – 1580 with respect to impacts on clean water. We layer the fabric from 1– to 4–plies which creates greater drag on spheres at entry and induces flow separation, creating a cavity. Punctured fabric draws inward as a cavity is formed subsurface, providing a constricted opening through which the protruding Worthington jet issues. With a growing number of plies, spheres must impact at greater Weber numbers to puncture the fabric. Those impacts that leave fabric intact do not create cavities or Worthington jets and are effective at splash mitigation. The use of a single layer of fabric, which is easily penetrated, allows hydrophilic spheres to form cavities at minute entry velocities. Across the range of entry velocities tested, separation angles for single layers increase with increasing velocity, whereas cavity geometry exhibits no strong correlation.

CHAPTER 3: MAKING A SPLASH WITH FABRICS IN HYDROPHILIC SPHERE ENTRY

Previously published in Journal of Fluids and Structures [19].

Splash dynamics associated with impacts of solid projectiles into aqueous pools are traditionally investigated with respect to impactor geometry, velocity, and surface roughness. Fluid surface alteration in some instances, may be more easily accomplished for the tuning of splashes. In this chapter, smooth, free-falling, hydrophilic steel spheres impact a quiescent liquid pool for Weber numbers in the range of 430 – 2700. Spheres strike fabrics resting atop the fluid surface which are either punctured or remain intact. As spheres strike fabrics, flow separation is tripped at low speeds which would otherwise not produce air-entraining cavities. Punctured fabrics suppress splash crowns normally seen for cavity-producing impacts while intact fabrics generate deeper cavities, higher Worthington jets, and pronounced splash crowns. Some fabrics, both punctured and intact reduce drag with respect to clean surface impacts by providing the drag-reducing benefits of flow separation while not offering a high inertial penalty. Such observations augur well for interfacial fluid-structure interactions where splashes warrant control.

3.1 Experimental Techniques

3.1.1 Impact Experiments

Smooth steel hydrophilic spheres of masses $m = 16.6, 28.6$ g and diameters $D = 1.6, 2.0$ cm are released into a 65-L, 36-cm deep aquarium, filled to a depth of 18 cm with tap water. The equilibrium and advancing contact angles on the impactors are $\theta_e = 63^\circ$ and $\theta_a = 68^\circ$, respectively,

and are measured photographically using a syringe to deposit water onto the spheres' surface. A pair of meter rulers are mounted vertically inside the tank such that the base of one rests adjacent to the free surface and the second rests on the aquarium floor as seen in Figure 3.1a. Square plies of fabric with dimensions $10.5 \text{ cm} \times 10.5 \text{ cm}$ are placed atop the fluid surface such that impacting spheres strike the approximate center of fabrics. Rulers fixed in the plane of impact act as visual scales for calibrating the digital tracking tool [18]. We clean and dry spheres with 99% isopropyl alcohol before each trial to preclude the influence of surface impurities. Spheres are released from drop heights in the range $h = 10 - 50 \text{ cm}$ without the influence of external forces such that motion is purely vertical, irrotational, and generates impact velocity of $U \approx (2 \cdot g \cdot h)^{1/2}$, where $g = 9.81 \text{ m/s}^2$ is the acceleration due to gravity. The sizes of our impactors consume very little fabric area, $1 - 2.8\%$, and permit an impact Weber number range of $430 - 2700$ while remaining well below the threshold of cavity formation for clean surfaces [1], $U \approx 8 \text{ m/s}$. Trials are replicated at least 3 times to reduce experimental variance and statistical errors included in our plots to show reproducibility of results [18]. We film impacts with a Photron Mini AX-100 high-speed camera at 2000 frames per second using a 120 mm Nikon lens. In select trials, a Photron Mini UX-100 is added to the experiment to provide a top-down view [18] of impacts on fabrics. Examples of top-down views for impacts onto punctured and intact fabrics are included in Figure 3.1b. We extract position track data and geometric measurements from videos using Open-Source Tracker.

Table 3.1: Measured fabric properties and curve fitting correlation values. Curve fitting values for Fabric A corresponds to non-dimensionalized trailing cavity depths κ_t/D as the independent variable, and are thus shown in red to distinguish this uniqueness.

Fabric	χ [μm]	ρ''_{dry} [mg/cm^2]	ρ''_{wet} [mg/cm^2]	$\sigma_{\text{f,dry}}$ [MPa]	$\sigma_{\text{f,wet}}$ [MPa]	Linear Fit R^2	Best Fit, α	Best Fit R^2
A	80	2.88	23.00	1.20	0.09	0.89	1.63	0.89
B	120	3.24	21.81	1.25	0.33	0.59	1.28	0.59
C	220	5.28	27.19	1.64	0.44	0.90	0.72	0.90
D	40	1.52	1.52	28.84	1.15	0.55	-3.1	0.69

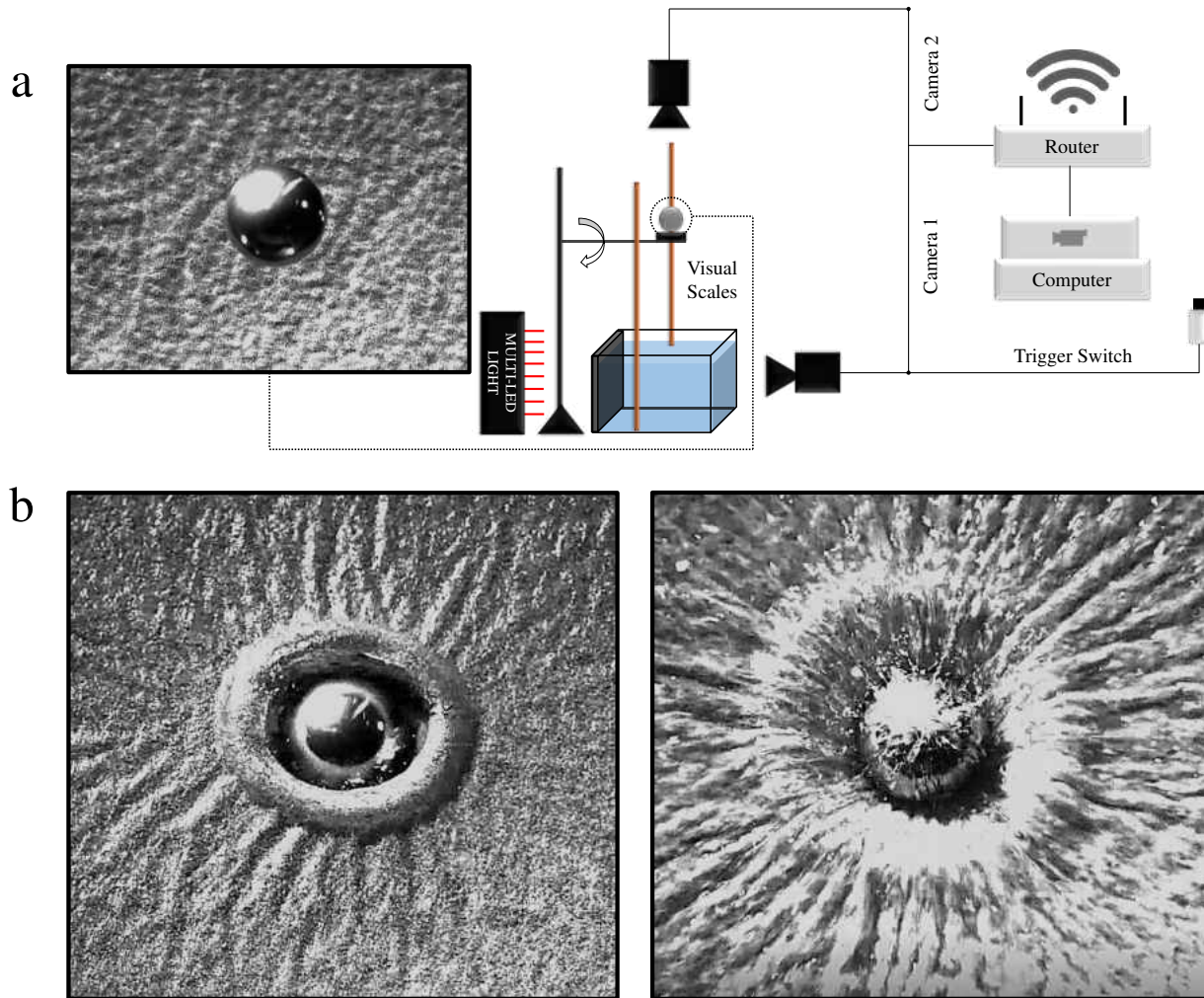


Figure 3.1: (a) Schematic of experimental setup. High-speed cameras capture frontal (Photron Mini AX–100) and overhead (Photron Mini UX–100) views with diffuse lighting positioned behind the tank. A wireless router enables multi-camera synchronization. (b) Sphere impact onto punctured (left) and intact (right) fabrics from an overhead view for $We = 2688$.

3.1.2 Material Property Measurements

We employ several brands of household fabric for surface alteration including: Georgia Pacific Compact Coreless 2–Ply Toilet Paper (Fabric A); Kleenex Trusted Care Facial 2–Ply Tissue (Fabric B); Georgia Pacific Sparkle Professional Series 2–Ply Perforated Roll Paper Towel (Fabric C); and

Darice Assorted Colors Tissue Paper (Fabric D). Microscopic images of fabric fibers are shown in the topmost panels of Figure 1.2. Failure stresses σ_f are measured with an MTS Criterion 42 tensile tester for dry and wet fabrics [85, 86, 87, 88, 89, 90, 91, 92, 93, 94, 95, 96]. To wet fabrics, we spray 3 cm \times 5 cm rectangular sheets with tap water once, using a 60–mL spray bottle, after placement between 5–kN load cells. Examples of stress-strain curves are included in the Online Supplement. Dry ρ''_{dry} and wet ρ''_{wet} area densities are measured by weighing fabrics on a Sartorius 225D–1S microbalance. To measure wet mass, we gently rest one edge of fabric rectangles in a small pool of water for 1 minute and allow capillary motion to completely wet the material. This method ensures that fabrics are not over-saturated before placement on the analytical balance.

3.2 Experimental Results

We impact four consumer-grade fabrics atop the free surface of a deep aqueous pool with two smooth, free-falling, hydrophilic steel spheres from various drop heights in the range $h = 10 - 50$ cm and compare changes in cavity dimensions, splash heights and drag coefficients with respect to impacts on an unaltered, clean surface (Figure 1.2a, Movie B1). Fabric squares measure 10.5 cm per side, a dimension chosen to match the manufactured dimensions of Fabric A. This choice of sheet size permits the penetration of Fabrics A & B, and the entrainment of Fabrics C & D. Fabric properties are measured and shown in Table 3.1. With sufficiently high impact velocities, spheres puncture fabrics and trigger flow separation; otherwise, fabrics remain intact and are pushed sub-surface ahead of descending spheres to form large air-entraining cavities.

Table 3.2: Single-factor analysis of variance (ANOVA) test for cavity depths and jet height with respect to Weber number.

Measurements	Fabric	Mean	Standard Deviation	Standard Error	p-Value
κ_f/D	A	1.23	0.1129	0.0652	0.2256
	B	2.20	0.3370	0.1945	9.29×10^{-5}
	C	2.38	0.2617	0.1511	2.40×10^{-5}
	D	2.92	0.2719	0.1570	2.60×10^{-5}
κ_t/D	A	1.51	0.4171	0.2408	0.2763
H_{max}/D	Water	2.42	0.1365	0.0788	4.37×10^{-11}
	A	2.48	0.5841	0.3372	6.39×10^{-4}
	B	3.12	0.5638	0.3255	9.27×10^{-8}
	C	3.45	0.5843	0.3374	1.20×10^{-6}
	D	3.42	0.6214	0.3588	3.05×10^{-6}

3.2.1 Fabric Properties Determine Cavity Shape

We begin by pictorially comparing cavity formation arising from the inclusion of thin, non-woven fabrics atop the fluid surface. Spheres impacting puncturable fabrics such as Fabrics A and B produce no splash crowns and prior to cavity seal [26], the presence of the fabric creates a discontinuity in the cavity wall, such that we may describe two distinct regions (Movie B2), as labeled in Figure 1.2. The shallower region is a conical cavity characterized by contact with the fabric, which we denote as the ‘fabric cavity.’ The deeper region is smoother and vertically-aligned behind the sphere, dubbed the ‘trailing cavity.’ Fabric A offers the least resistance to puncture across the four test fabrics with $\sigma_{f,wet} = 0.09$ MPa. A typical cavity produced by Fabric A is shown in Figure 1.2b, and displays a shallow seal which arises from pressure imbalances close to the free surface [26]. The trailing cavity of Figure 1.2b remains attached until impact with the container floor. Fabric cavity depths κ_f show minimal variation across the range of Weber number tested for Fabric A (p-value = 0.2256, Table 4.1) as shown in Figure 3.2b. The lengths of trailing cavities κ_t attached to descending spheres at the moment when the fabric and trailing cavities are sealed from one another likewise shows a weak correlation with Weber number (p-value = 0.2763) as shown

in Figure 3.2d. For $We > 860$, trailing cavities pinch-off approximately 20 ms after fabric cavities form, creating deeper seals [35] as pictured in Figure 3.2a.

A typical cavity produced by Fabric B is shown in Figure 3.3a, and shares the same cavity regions as Fabric A. However, Fabric B offers greater puncture resistance by way of a greater failure stress, $\sigma_{f,wet} = 0.33$ MPa, nearly 4X that of Fabric A. The impacting sphere forces Fabric B 25% further below the free surface than Fabric A prior to puncture, as shown in the photos of Figure 3.3a. The result is a fabric cavity that is on average, twice as deep, creating a longer transition region to the trailing cavity (Movie B3). The depth of the fabric cavity grows mildly with increasing Weber number (p -value < 0.0001), as shown in Figure 3.3b. Hydrophilic steel sphere impacts onto intact Fabrics C and D generate time-variant flow separation, ascending splash crowns and greater cavity depths κ_f when compared to their punctured counterparts. This comparison is seen qualitatively in Figure 3.4a and Figure 3.5a, and quantitatively in Figure 3.4b and Figure 3.5b. Despite fabrics obscuring the visibility of flow around spheres, we observe the formation of trailing cavities after pinch-off. As spheres descend, fabrics are pulled inward and deep seal [26] cavities generated. For such impacts, pinch-off occurs much closer to the spheres, typically greater than $2/3$ the distance between spheres and the modified free surface (Movies B4 and B5). In Figure 3.6a, we plot non-dimensionalized fabric cavity depths κ_f/D versus We for all fabrics on test.

3.2.2 Greater Puncture Resistance Promote Higher Worthington Jets

Flow separation from spheres descending through fabric creates air-entraining cavities [17]. Following the collapse of these cavities, Worthington jets protrude above the free surface. We measure the heights H_{max} of these jets above the free surface and show the inclusion of thin fabrics that are punctured or remain intact amplifies splash heights with respect to an unaltered surface (Figure 3.6b), as seen in Figure 3.6c. Disaggregated plots with error bars for the data presented in Fig-

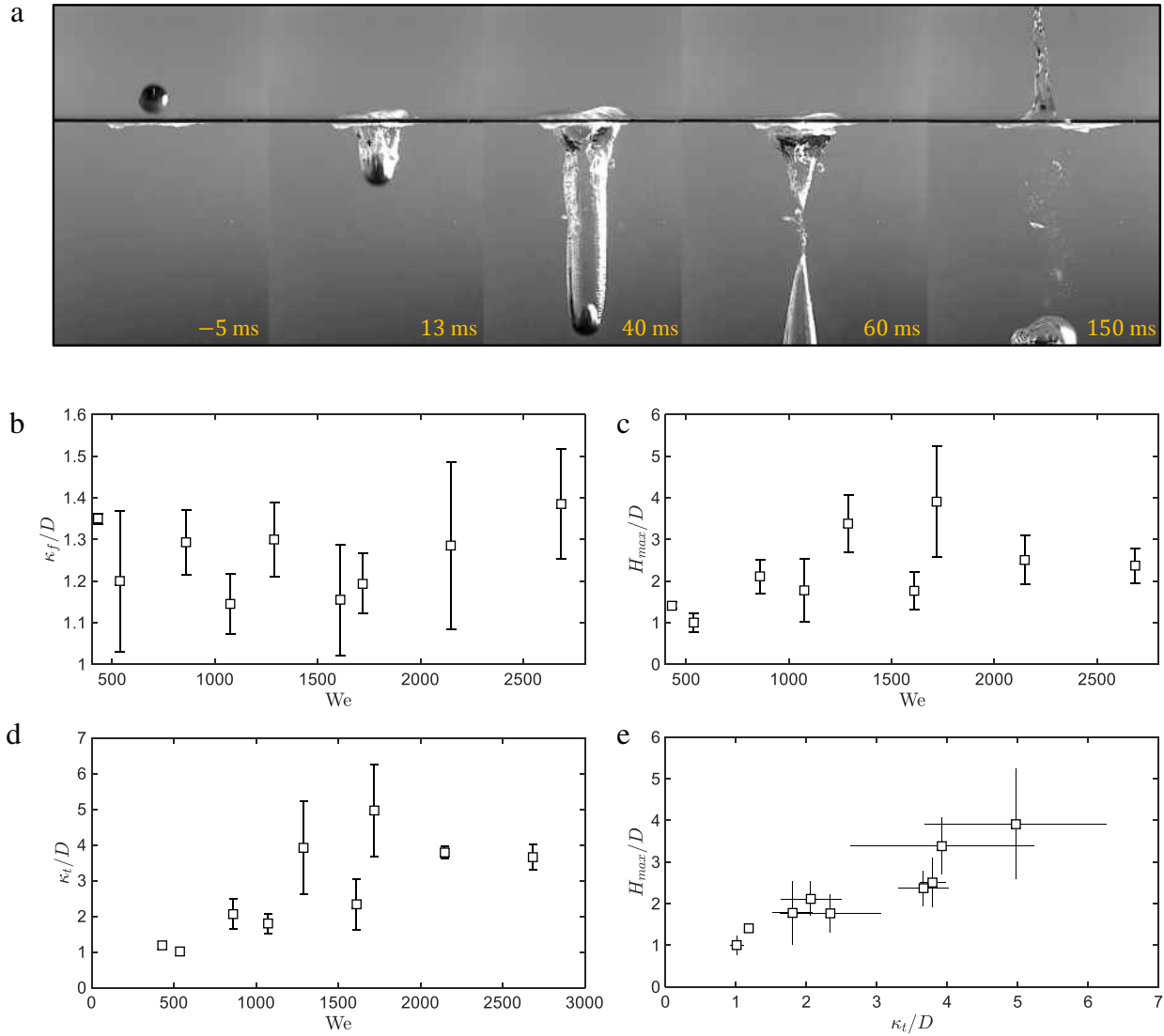


Figure 3.2: Fabric A. (a) Time-sequence of a 2-cm hydrophilic steel sphere impacting a single sheet for $We = 2688$ (Movie C2). Upon impact, a fabric-dependent cavity is formed and collapses near the free surface due to pressure imbalances. As sphere descend, a deeper, smoother, vertically-aligned cavity develops. The trailing cavity again pinches off and adds inertia to the retracting mass of fluid prior to the formation of a Worthington jet. (b) Non-dimensionalized fabric cavity depths κ_f/D versus Weber number We . (c) Non-dimensionalized Worthington jet height H_{max}/D versus Weber number We . (d) Non-dimensionalized trailing cavity lengths κ_t/D versus Weber number We . (e) Non-dimensionalized Worthington jet height H_{max}/D versus non-dimensionalized trailing cavity lengths κ_t/D .

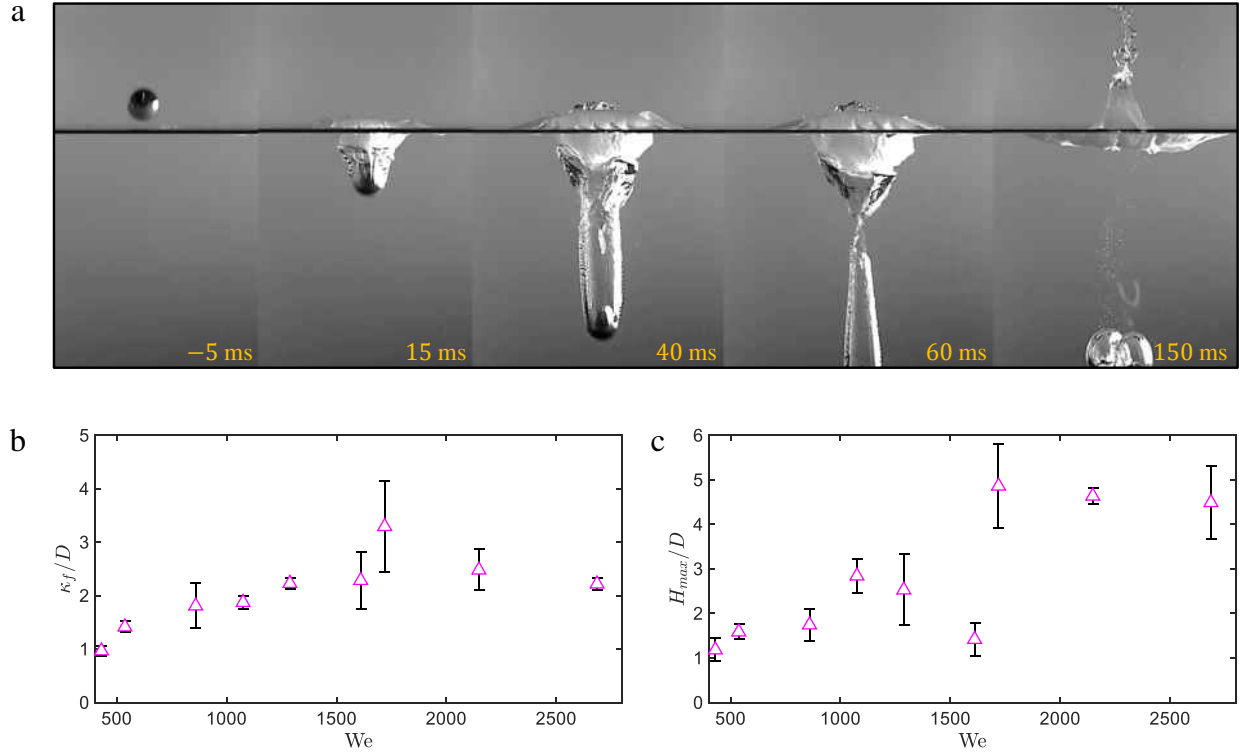


Figure 3.3: Fabric B. (a) Time-sequence of a 2-cm hydrophilic steel sphere impacting a single sheet for $We = 2688$ (Movie B3). Upon impact, a fabric-dependent cavity is formed and collapses near the free surface due to pressure imbalances. As sphere descends, a deeper, smoother, vertically-aligned cavity develops. (b) Non-dimensionalized fabric cavity depths κ_f/D versus Weber number We . (c) Non-dimensionalized Worthington jet height H_{max}/D versus Weber number We .

ure 3.6c are provided in Figure 3.2c, Figure 3.3c, Figure 3.4c, and Figure 3.5c for Fabrics A–D, respectively. We plot non-dimensionalized splash heights H_{max}/D against non-dimensionalized cavity depths κ_f/D in Figure 3.6d for all test fabrics to show how the relationship between cavity depths and splash heights changes with fabric strength. Disaggregated plots are included in the Online Supplement. Generally, as fabric failure stress σ_f increases, so does κ_f for a given H_{max} as the deformable interface becomes more difficult to penetrate for larger values of σ_f . The threshold for puncture for our impactors within the test range of We lies between the strengths of Fabrics B and C, $\sigma_{f,wet} = 0.33$ and 0.44 MPa, respectively.

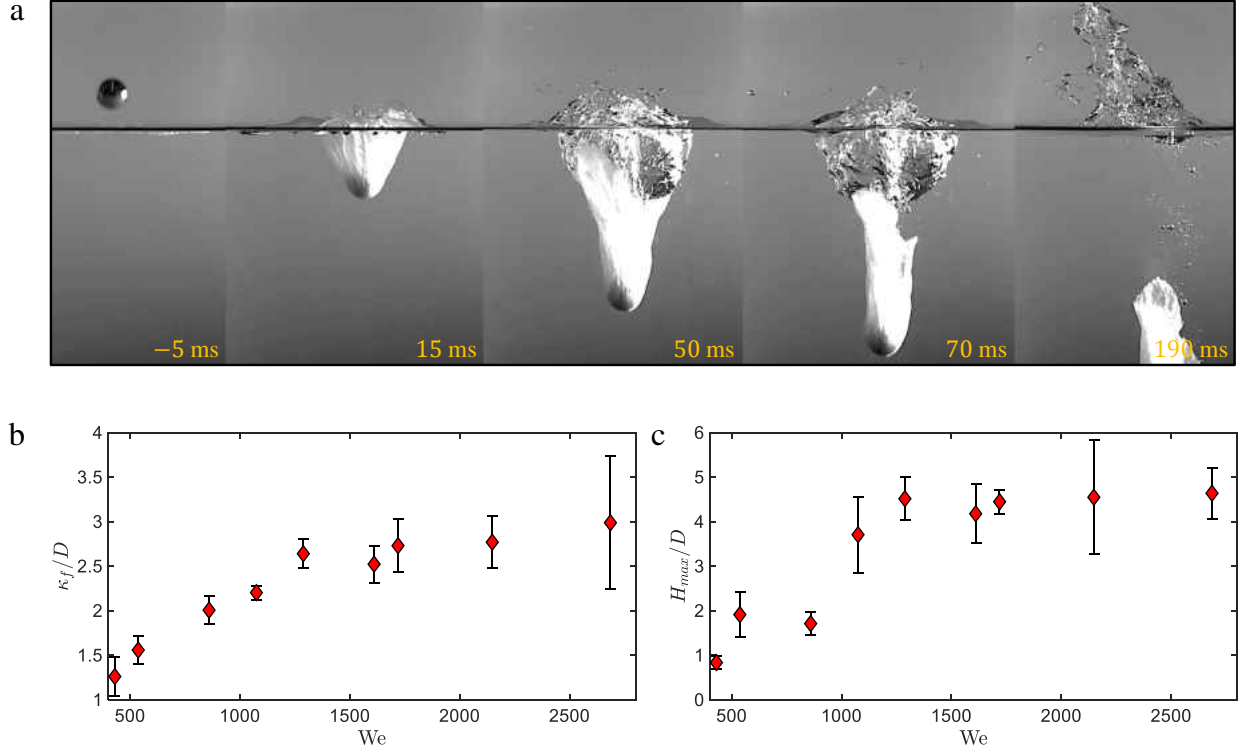


Figure 3.4: Fabric C. (a) Time-sequence of a 2-cm hydrophilic steel sphere impacting a single sheet for $We = 2688$ (Movie B4). Upon impact, fabrics are pulled inward and form deep seal cavities, with pinch-off occurring close to spheres, typically $2/3$ the distance between spheres and the modified free surface. (b) Non-dimensionalized fabric cavity depths κ_f/D versus Weber number We . (c) Non-dimensionalized Worthington jet height H_{max}/D versus Weber number We .

We rationalize the trends for H_{max}/D in Figure 3.6d by considering a conical cavity that seals behind a descending sphere, ultimately collapsing to produce a Worthington jet of diameter D_j . A cavity of diameter D_c and volume $V_c \sim D_c^2 \kappa_f$ is subject to a buoyant force $F_{B,c} \sim \rho g V_c$, and upon collapse experiences boundary work $W_{B,c} \sim F_{B,c} \kappa_f$. The influence of surface tension on cavity collapse is negligible given that Bond number $Bo = \Delta \rho g \kappa_f^2 / \sigma \gg 1$, where $\Delta \rho$ is the difference between water and air density. As the cavity retracts, the work of the collapsing cavity is converted to gravitational potential energy in the jet $W_{B,c} \sim E_{p,j} \sim \rho g V_j H_{max}$, where $V_j \sim D_j^2 H_{max}$ is the volume of the protruding fluid [17]. For simplicity, we assume geometric similarity of Worthington

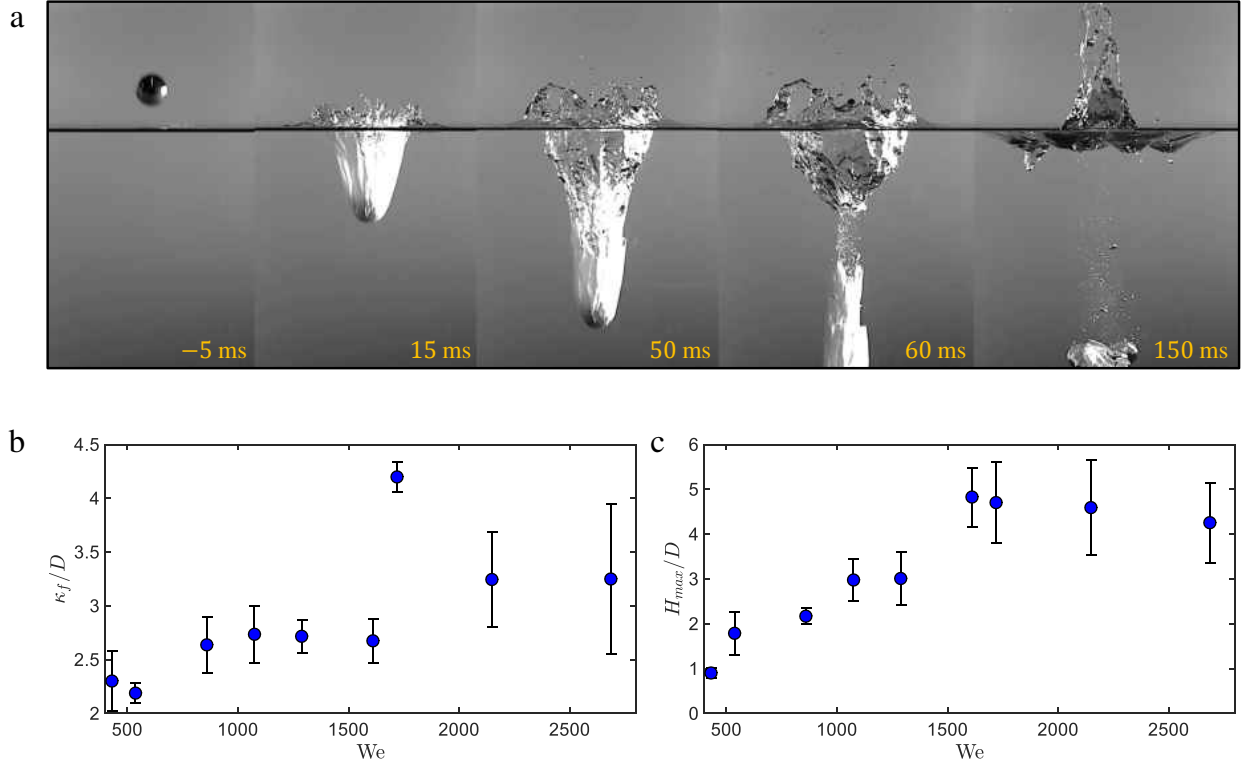


Figure 3.5: Fabric D. (a) Time-sequence of a 2-cm hydrophilic steel sphere impacting a single sheet for $We = 2688$ (Movie B5). Upon impact, fabrics are pulled inward and form deep seal cavities, with pinch-off occurring close to spheres, typically $2/3$ the distance between spheres and the modified free surface. (b) Non-dimensionalized fabric cavity depths κ_f/D versus Weber number We . (c) Non-dimensionalized Worthington jet height H_{max}/D versus Weber number We .

jets across impact trials. We neglect viscous dissipation during cavity collapse and jet ascension given $Re > 26,000$. Therefore we may write $\rho g D_c^2 \kappa_f^2 \sim \rho g D_j^2 H_{max}^2$. Experience mandates the diameter of a disturbance in a compliant fluid surface is approximately equal to the diameter of the ensuing response, $D_c \sim D_j$. Accordingly,

$$H_{max} \sim \kappa_f. \quad (3.1)$$

We fit Eq.(3.1) to our experimental data and find linear fit correlation values in the range $R^2 = 0.69 - 0.88$ for Fabrics B–D. Individual correlation values are given in Table 3.1 alongside best fit exponents according to $H_{\max} \sim \kappa_f^\alpha$. We note an insignificant change in correlation values when the exponent α deviates from unity for Fabrics B and C. By contrast, $\alpha = -3.1$ for Fabric D, a stark deviation from unity, producing a small correlation value improvement of 0.14. The cause for this contrast is unknown, but it is noteworthy that Fabric D is anomalous in ρ_{wet}'' and $\sigma_{\text{f,dry}}$ compared to the other fabrics.

Fabric A does not fit well to the scaling argument given in Eq.(3.1), $\alpha = -72$, because the collapse and ascension of trailing cavities is the primary contributor to Worthington jet creation (Figure 3.2e, Movie B2). For impacts onto Fabric A, the work done by cavity collapse scales with κ_t , and using the aforementioned arguments, the jet height for impacts through Fabric A obeys,

$$H_{\max} \sim \kappa_t. \quad (3.2)$$

We fit Eq.(3.2) to our experimental data and find linear fit correlation value $R^2 = 0.89$ for Fabric A. For non-cavity producing impacts [17], the gravitational potential energy of a sphere of density ρ_s and volume V_s is converted to gravitational potential in the jet, $\rho_s V_s g h \sim \rho V_j g H_{\max}$. We rationalize $V_j \sim V_s$ by noting that the volume of fluid displaced by the sphere should be that thrown airborne into the jet. Thus, the heights of Worthington jets arising from impacts with free surface conditions are more suitably described by

$$H_{\max} \sim h, \quad (3.3)$$

as shown in Figure 3.6d and verified in previous work [17]. Best fits and linear fits as discussed

above are shown in Figure A.5.

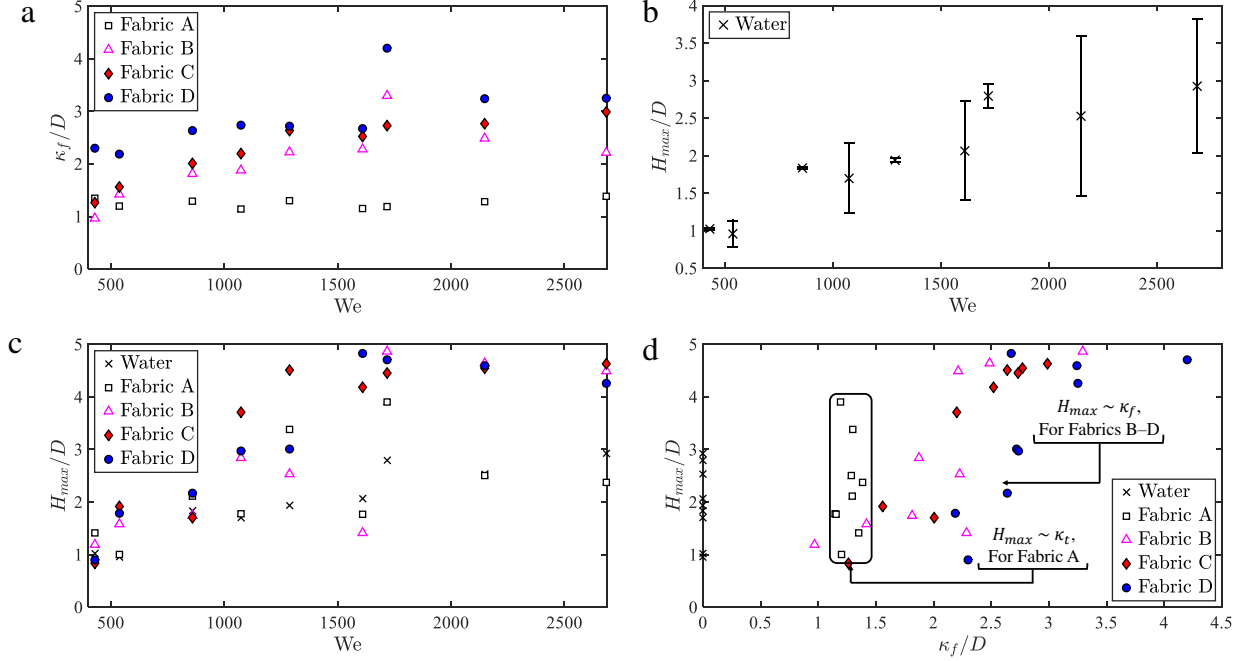


Figure 3.6: (a) Aggregated plot of non-dimensionalized fabric cavity depths κ_f/D versus Weber number We for all fabrics on test. (b) Non-dimensionalized Worthington jet height H_{max}/D versus Weber number We for sphere impacts onto an unmodified free surface. (c) Aggregated plot of non-dimensionalized Worthington jet height H_{max}/D versus Weber number We for all fabrics on test. (d) Aggregated plot of non-dimensionalized Worthington jet height H_{max}/D versus non-dimensionalized fabric cavity depths κ_f/D for all fabrics on test.

3.2.3 Fabrics Amplify and Attenuate Hydrodynamic Drag

To compare the hydrodynamic drag force induced by test fabrics, we fix drop height $h = 50$ cm such that $U = 3.13$ m/s and track the center of mass of 2–cm steel spheres, as seen in Figure 3.7a. Position track data is initialized ($t = 0$ s) when spheres strike the fluid surface and terminated just before impact with the floor of the liquid pool. A force balance for a sphere of mass m falling

vertically into a quiescent liquid bath is given by [17]

$$F_D = mg - (m + m_a)a - F_B - F_\sigma, \quad (3.4)$$

where $F_D = \pi\rho U^2 C_D D^2/8$ is the drag force acting on the sphere, a is the linear acceleration of the sphere, $m_a = \pi\rho D^3 C_m/6$ is the added mass, accounting for the effect of accelerating fluid by the falling sphere [17], and $C_m = 0.5$ is the added mass coefficient, treated as a constant across all cases [21, 24]. We note that while C_m increases from zero at impact [21, 24], our model is not highly sensitive to this change given $m/m_a \sim O(10)$, producing a 13% variance in the calculated value of C_D over a range of $C_m = 0 - 1$. Buoyancy force [17] is given by $F_B = \rho g(\frac{\pi}{6}D^3 + A(y)y)$, where y is the position track and $A(y)$ is cross-sectional area of the sphere at the plane of flow separation [17]. For further simplification, we treat $A(y)$ as constant by assuming separation at the equator such that $F_B = \rho g\pi(\frac{D^3}{6} + \frac{D^2}{4}y)$. We may neglect the force due to surface tension $F_\sigma = \sigma D$ in the range of Weber number on test. Thus, Eq.(3.4) can be rewritten as

$$\frac{du}{dt} = \frac{mg}{m'} - \frac{\rho g\pi D^2}{8m'} \left(\frac{4}{3}D + 2y + \frac{C_D}{g}u^2 \right), \quad (3.5)$$

where $m' = m + m_a$. Position track data is smoothed with a Savitzky-Golay filter [84] to remove the effects of experimental error prior to numerical differentiation to obtain $u(t)$, and then smoothed once more prior to the final differentiation to obtain $a(t)$. The smoothing filter is a generalized moving average spanning the entire dataset with coefficients determined by an unweighted linear least-squares regression and a polynomial model of specified degree. Figures B3–B6 demonstrate the effect of various filtering options on experimental and differentiated data, and C_D . Filter options were chosen to maintain the physical integrity of the data throughout processing. Other smoothing and differentiation techniques are available, such as that provided by Epps *et al.* (2010) [97], but

such techniques did not provide us with physically relevant data due to limitations in measuring sphere position precisely when shrouded by fabric.

A numerical solution of Eq.(3.5) provides values of C_D for each fabric in the range of instantaneous Reynolds number $Re = \rho Du(t)/\mu = 45,000 - 71,000$, where $\mu = 8.90 \times 10^{-4}$ Pa·s is the dynamic viscosity of water, as plotted in Figure 3.7b. As a further comparison of drag coefficients C_D imposed by each fabric, consider the following values for $Re = 70,000$: 0.30 – free surface; 0.27 – Fabric A; 0.40 – Fabric B; 0.68 – Fabric C; and 0.27 – Fabric D. The increase in C_D from Fabric A through C corresponds with increasing ρ''_{wet} and $\sigma_{f,wet}$. Though the most resistant to puncture, Fabric D's relatively low ρ''_{wet} allows the sphere to enter against relatively little inertial resistance.

Our calculated drag coefficients $C_D \approx 0.1 - 0.3$ for clean water align with those of steadily-translating spheres in the same Reynolds number range, $Re \approx 10^4 - 10^5$, and have positive slope with increasing Re [98, 99, 100, 101]. With respect to clean water producing non-cavity forming impacts Fabric A (punctured) and Fabric D (intact) reduce drag force during descent as seen in Figure 3.7b. This surprising result may be interpreted in the context of the work of Truscott *et al.* (2012) [25], who explored the unsteady forces on free-falling hydrophilic and hydrophobic spheres traversing the liquid bath. In their study, non-cavity forming impacts by 2.54-cm steel spheres with $Re = 12,500 - 87,500$ and entry velocity $U = 3.43$ m/s, had higher drag coefficients $C_D = 0.20 - 1.00$ than their cavity forming ($\theta_e = 120^\circ$) counterparts $C_D = 0.35 - 0.40$ due to pressure recovery in the wake and the initiation of vortex shedding [25]. Although the inertial resistance or mechanical failure of the fabric acts to increase drag, the suppression of trailing vortices by the air-entraining cavity results in a net reduction in entry resistance.

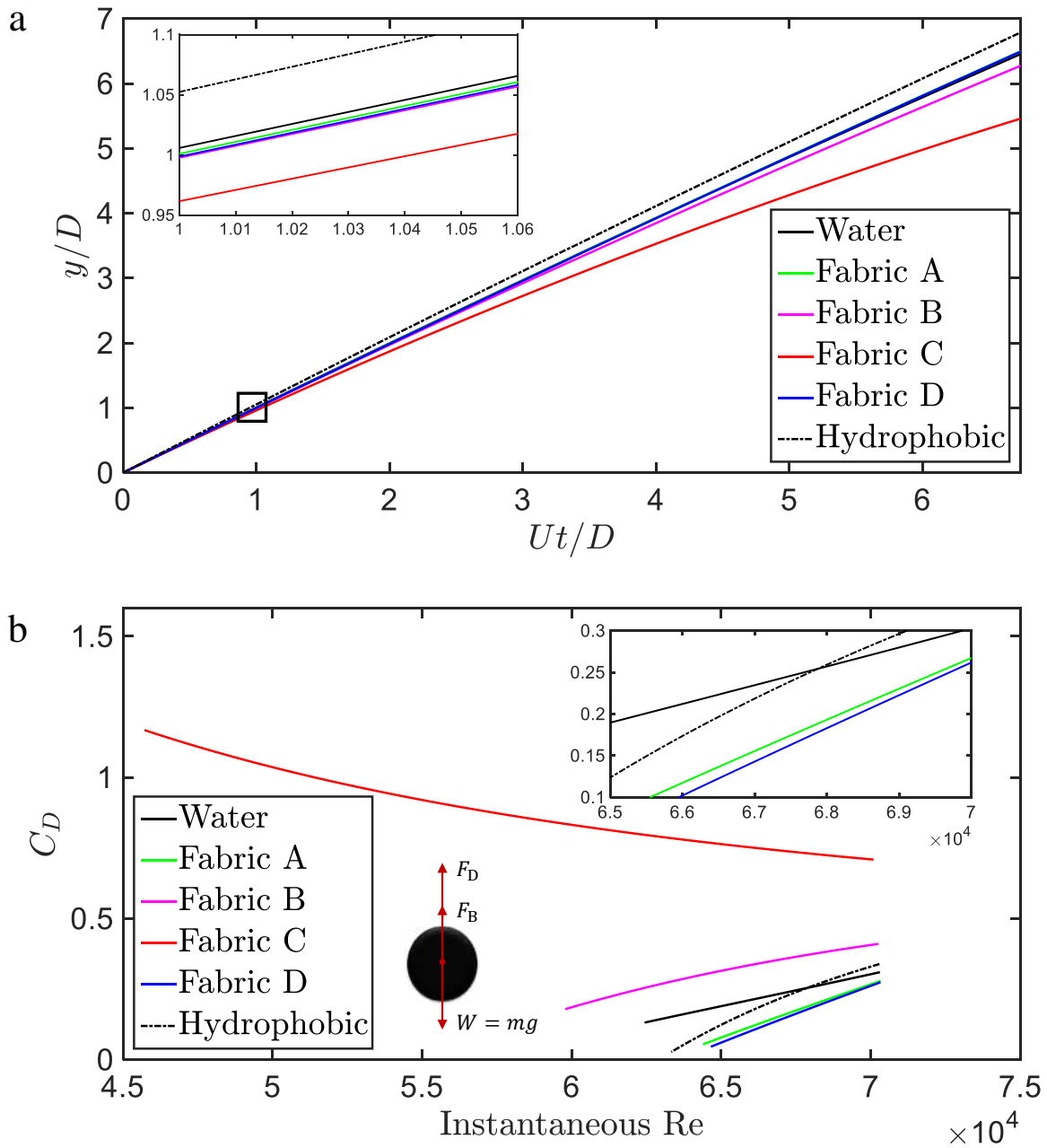


Figure 3.7: (a) Non-dimensionalized vertical position versus dimensionless time. Trajectories are smoothed with a Savitzky-Golay filter to remove the effects of experimental error. (b) The relation between hydrodynamic drag coefficient C_D and instantaneous Reynolds number Re .

3.3 Discussion

This study shows that hydrophilic steel spheres impacting a liquid bath modified by the placement of thin, non-woven fabric sheets atop the fluid surface experience fabric dependent cavity shapes and Worthington jet heights. Splashes from spherical projectiles colliding with the compliant fabric interface generate greater jet heights compared to impacts with an unmodified free surface. In contrast to jet amplification, impacts onto punctured fabric sheets attenuate splash crowns. Intact impacts amplify splash crowns as fabrics ride ahead of spheres during descent through the aqueous pool. Below the surface, cavity-producing impacts induced by fabric sheets are unable to generate smooth, uniform cavity walls normally seen for the water entry of smooth hydrophobic spheres [26] (Movie B6). Instead, surface waves appear on cavity walls due to the inherent jaggedness that accompanies torn fabric, creating localized variation in flow separation, and confirming the coupling of fabric properties to cavity behavior. This inherent jaggedness is a likely cause of the random, and in some places, severe variation in splash characteristics of Figure 3.6.

The chosen size and shape of our impacted fabrics determine their status as punctured or intact, and the ability of the impactor to partially or fully entrain the fabric. If the fabrics were infinite in size, punctured Fabrics A & B would remain so, while Fabrics C & D may become punctured at some value of We in our experimental range. The status of Fabrics C & D as intact is reliant on their compliance. We do not expect changing the profile of fabric, i.e. to a circle (Movie B7), to substantially influence puncture or cavity dynamics, but instead expect changes to fabric buckling (Figure 3.1b) at impact. The absorbency of fabrics on test is accounted for by the area density ρ'' and failure stress σ_f as shown in Table 3.1. As such, the use of non-wetting fabrics would provide a greater range of ρ'' and σ_f that remain unchanged when wet.

The complex nature of fabric buckling and tearing as shown by the collision in Figure 3.1b, makes the prediction of Worthington jet alignment with the vertical axis intractable. Jet direction variance

from vertical is reflected in the experimental noise of Figure 3.6. An example of jet deviation from vertical can be seen in Movie B3. To further highlight the role of buckling on splash directionality, we substitute fabrics with thin, layers of ice. The falling sphere punches an opening in the ice, tripping flow separation, followed by a vertically ascending jet with no horizontal velocity, likely due to the absence of buckling during the brittle fracture of the interface (Movie B8). In contrast to ice, the physical properties of the interface will, in many cases, not be isotropic. While all our non-woven fabrics exhibit isotropic properties, woven fabric weaves can provide anisotropic stiffness [102, 103, 104] and substantially different buckling patterns. Thus, the relation between fabric buckling and splash dynamics is an area requiring further investigation.

The square profile of our fabrics ensures of intact fabrics, such that the corners will trail furthest behind the impactor. Deviation from perfectly centric impacts, which are inevitable, will likewise produce variations in buckling, which we do not expect to significantly bias results. We justify this notion by observation of Figure 3.4a (Movie B4) and Figure 3.5a (Movie B5), in which the non-axisymmetric buckling does not appear to have a large effect on splash features, such as the crowns. We add robustness against eccentric impacts by repeating trials three times and choosing impactors with diameters $\leq 19\%$ the length of our fabric squares. At the extreme of eccentricity, spheres strike edge of the fabric, producing localized half-cavities at low entry velocities. We drop a 2-cm Delrin sphere with mass $m = 7.7$ g from $h = 10$ cm and ensure water entry along the fabric edge (Movie B9). Upon impact, flow separation is tripped only along the portion contacted by fabric. The partial obstruction by compliant films is thus another means to tune splash dynamics that requires further investigation.

3.4 Chapter Summary

Punctured fabrics create two cavity regions as the impactor descends. The shallower cavity is approximately cone-shaped, while the deeper cavity is elongated has a diameter approximately equal to impactor width. The shape of cavities induced by punctured fabrics is a result of tripping flow separation at velocities which would otherwise not produce air-entrainment. Punctured fabrics remain near the free surface, suppressing the splash crown, but allowing passage of a Worthington jet whose height increases with Weber number. Intact fabrics create cavities by veiling the descending impactor, amplifying the splash crown and producing Worthington jets which likewise increase in height with Weber number. Generally, increases in fabric wet area-density and puncture resistance promote greater air-entraining cavity depths. The collapse of deeper cavities produces higher Worthington jets. Fabrics with high area-density slow impactor speed via dominant inertial effects, but when compared to impacts that produce no cavities, air-entraining cavities reduce drag, as evidenced by employment of lightweight and easily punctured fabrics. Splash height and impactor motion may thus be tuned by fabric properties.

CHAPTER 4: WATER ENTRY DYNAMICS OF SPHERES WITH HETEROGENEOUS WETTING PROPERTIES

Water entry studies traditionally employ homogeneous projectiles of varying impactor shape, entry speed, and surface roughness. Surface heterogeneity is yet another means to manipulate splash dynamics. In this chapter, we systematically investigate the water entry of smooth, free-falling, hemispherically-coated spheres for Weber numbers in the range of 591 – 3360. Hydrophilic spheres are hemispherically-coated with a hydrophobic compound and in-turn produce deep seal cavities, provoke changes in super-surface splash features, and alter sphere trajectories. Generally, flow separation is initialized when hydrophobic surfaces make contact with the fluid, leading to air-entrainment across the range of entry speeds and impact orientations on test. Cavity formation induced by the hydrophobic portion of a coated sphere promotes flow separation across the hydrophilic surface at impact velocities well below the threshold required for air-entrainment by completely hydrophilic spheres. Spheres having hydrophilic and hydrophobic surfaces entering the fluid simultaneously, experience asymmetric cavities and lift forces that result in lateral migration from straight-line trajectories. Such observations augur well for water entry applications where the coupled dynamics of flow separation and passive trajectory control are desirable.

4.1 Experimental Techniques

4.1.1 *Impactor Surface Treatment*

Delrin spheres of masses $m = 4.9, 7.7,$ and 11.5 g and diameters $D = 1.9, 2.2,$ and 2.5 cm are cleaned in their entirety with 99% isopropyl alcohol and allowed to dry in a closed container. The surface of the spheres that are to remain hydrophilic are masked with tape and rested in cir-

cular cutouts on an acrylic sheet which holds spheres in place. The portion of the spheres left exposed atop the acrylic sheet are sprayed with Rustoleum NeverWet. We henceforth refer to these hemispherically-coated spheres as $\alpha = 0.33$ and $\alpha = 0.50$, as depicted in Figure 4.1a. The coated portion of the sphere may be described as if the sphere had been submerged in the hydrophobic compound to $1/3$ or $1/2$ its diameter, respectively. With spray nozzle $15 - 30$ cm from the exposed surfaces, spheres are sprayed twice with the Base Coat and allowed to dry for 30 -min, before twice applying the Top Coat [18]. Coated impactors are allowed to cure for at least 12 -hrs before use in experiments. Just prior to each impact trial, we again clean the hydrophilic surface with 99% isopropyl alcohol. The equilibrium and advancing contact angles of coated surfaces are $\theta_e = 105^\circ \pm 2^\circ$ and $\theta_a = 128^\circ \pm 4^\circ$ ($N = 6$), respectively, measured photographically [17, 18, 19] using a syringe to deposit water onto the sphere's surface. In contrast, the equilibrium and advancing contact angles on the uncoated surfaces are $\theta_e = 75^\circ \pm 4^\circ$ and $\theta_a = 87^\circ \pm 3^\circ$ ($N = 6$), respectively. These advancing contact angles, and the interaction of fluid with spheres of similar wetting properties are shown in Figure 4.1b, according to the predictions of Duez *et al.* (2007) [1]. A 'line of demarcation' is drawn circumferentially with a fine-tip permanent marker to visually separate hydrophilic and hydrophobic zones on the spheres. The marker ink does not substantially influence the wetting properties of an untreated surface. After no more than 15 impact trials, a sphere is cleaned by a soak in 100% acetone for 1 -min, followed by the aforementioned cleaning with 99% isopropyl alcohol. This treatment removes the NeverWet Coating so that spheres may be re-coated.

4.1.2 Impact Experiments

Spheres are released from drop heights $h = 10 - 50$ cm into a 65 -L, 36 -cm deep tempered-glass aquarium, filled halfway with tap water as shown in Figure 4.1a. The drop apparatus and experimental protocols used for impact trials are detailed in our previous works [17, 18, 19]. For splash

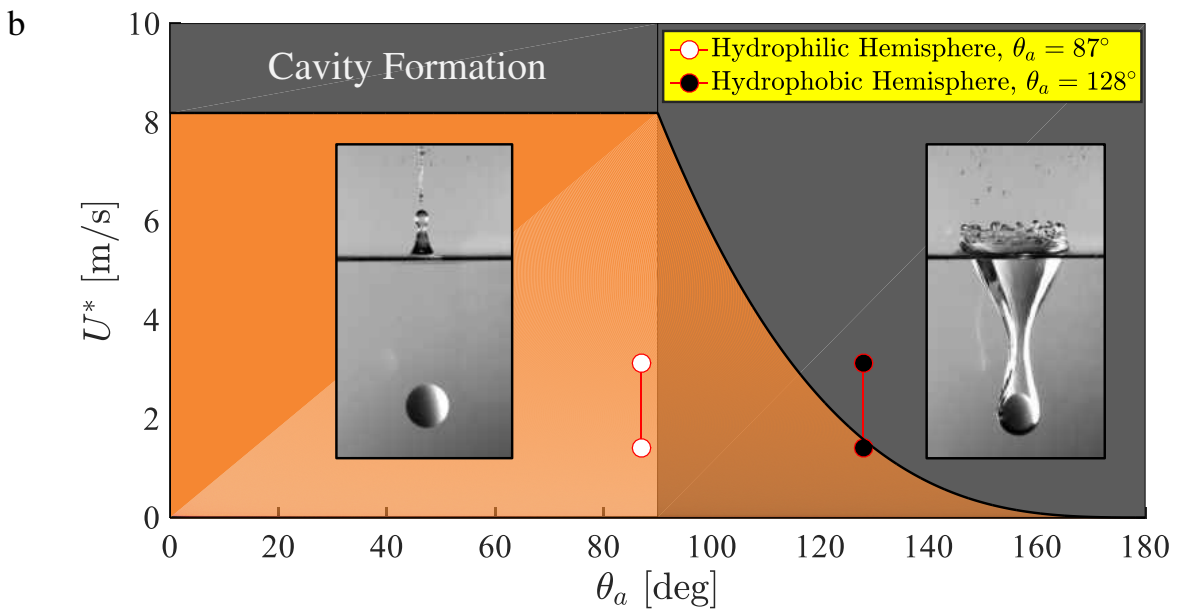
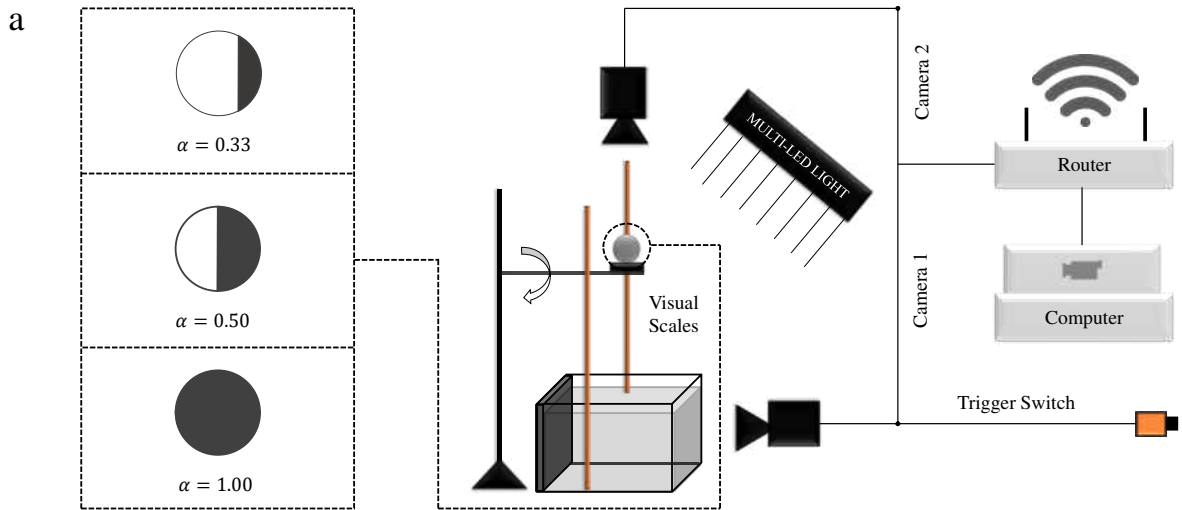


Figure 4.1: (a) Schematic of experimental setup. High-speed cameras capture frontal (Photron Mini AX-100) and overhead (Photron Mini UX-100) views with diffuse lighting positioned behind the glass tank and above the frontal camera. Optional trigger switch complements manual controls in video recording software on computer. Wireless router enables multi-camera synchronization. (b) Threshold velocity U^* for cavity formation as a function of the advancing contact angle θ_a . Solid lines are theoretical predictions based on the seminal work of Duez *et al.* (2007) [1].

visualization and tracking, we film water entry with a Photron Mini AX–100 high-speed camera at 1000 frames per second with resolution of 1028×1028 pixels using a 120–mm Nikon lens. Our chosen field of view is $21.5 \times 21.5 \text{ cm}^2$, yielding a 47.8 pixel/cm magnification. Geometric measurements such as cavity depths κ and widths λ pictured in Figure 1.3b, are extracted from captured videos using Tracker, an open source image analysis software [18].

4.2 Experimental Results

The water entry of cavity-producing projectiles can be summarized in stages, namely: collision with the free surface; air-entrainment; splash crown ascension; cavity closure and collapse; and Worthington jet projection. In this study, water entry stages are influenced by the arrangement of spheres on test. We impact the quiescent, unbounded free surface of a deep aqueous pool with hemispherically-coated spheres from various drop heights in the range $h = 10 - 50 \text{ cm}$. Four cavity-producing entry scenarios are considered: (i) fully hydrophobic sphere ($\alpha = 1.00$, Figure 1.3b, Movie C1); (ii) heterogeneous sphere, impacting the free surface along the hydrophilic hemisphere, $\beta = 0^\circ$ (Figure 1.3c, Movie C2); (iii) heterogeneous sphere, impacting the free surface along the line of demarcation, $\beta = 90^\circ$ (Figure 1.3d, Movie C3); and (iv) heterogeneous sphere, impacting the free surface along the hydrophobic hemisphere, $\beta = 180^\circ$ (Figure 1.3e, Movie C4). These four impact scenarios are graphically depicted in Figure 1.3. Flow separation is achieved for all water entry permutations (i)–(iv), on test, which stands in contrast to their purely hydrophilic counterparts (Figure 1.3a, Movie C5). We discuss these in turn.

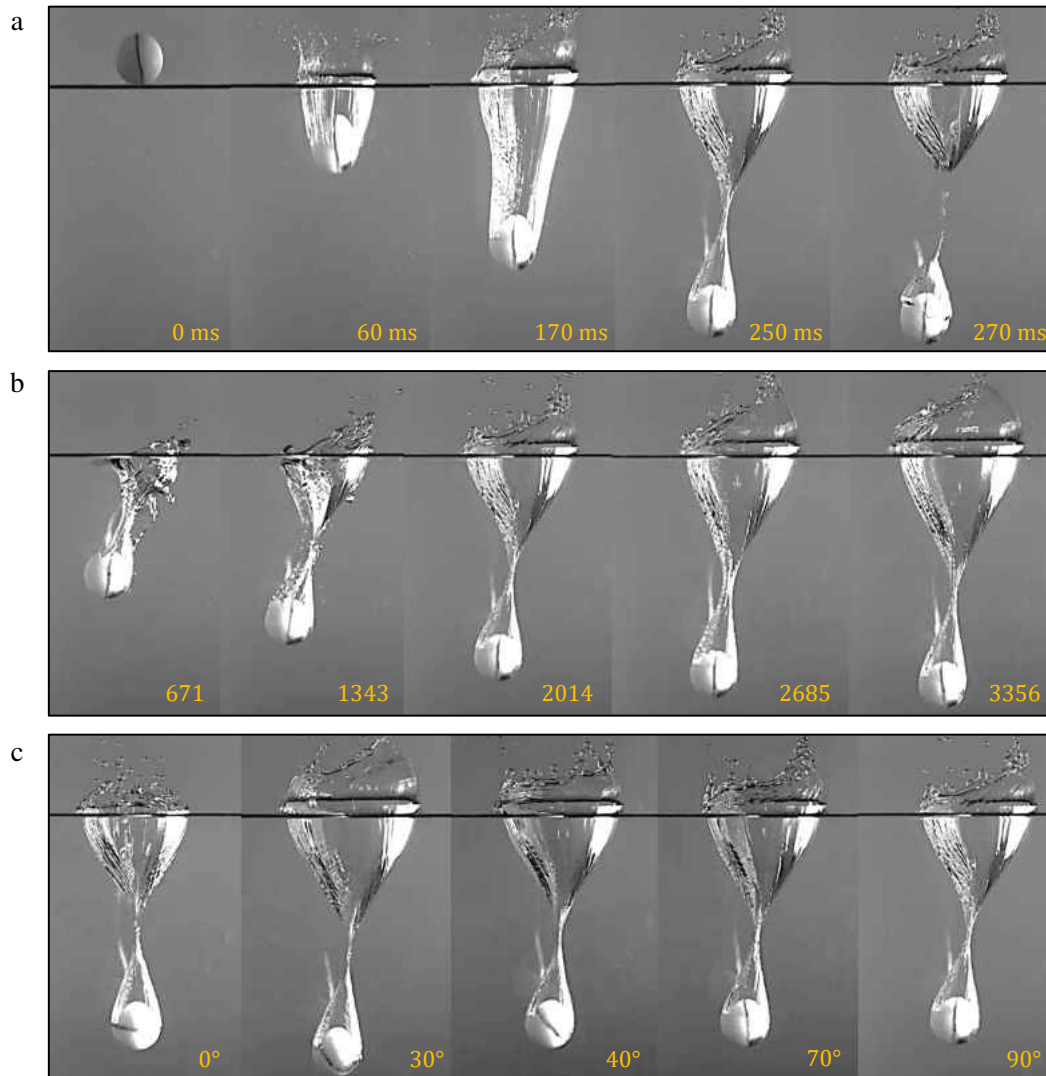


Figure 4.2: (a) Temporal evolution of an air-entraining cavity and ascending splash crown for the water entry of a heterogeneous sphere, $\alpha = 0.50$, $\beta = 90^\circ$. A smooth cavity wall develops on the hydrophobic side of sphere, whereas a rough cavity wall envelopes the sphere along the hydrophilic hemisphere prior to cavity pinch-off. Cavity formation and splash crown ascension for the water entry of a half-coated hydrophilic sphere making impact across the range of (b) Weber numbers We and, (c) impact orientations β on test. Spheres have diameter $D = 2.54$ cm. We choose $We = 2014$ when iterating impact angles in (c).

4.2.1 *Impactor Surface Treatments Modulate Splash Features*

We pictorially compare cavity formation for the aforementioned water entry scenarios in Figure 1.3. Fully hydrophobic spheres impacting the liquid bath entrain air to form deep seal cavities [26] characterized by smooth cavity walls as shown in Figure 1.3b. A typical splash generated by orientation (ii), $\alpha = 0.50$ and $\beta = 0^\circ$, is pictured in Figure 1.3c. Cavities are visually distinguishable from $\alpha = 1.00$ by the jaggedness of cavity walls. In this case, flow separation is delayed until the fluid makes contact with the upward-facing hydrophobic surface of the sphere. Hence, the three-phase contact line [13] coincides with the line of demarcation. For impacts below $We \approx 1250$ pinch-off occurs at depths shallower than the sphere diameter D and stable-streamlined [14] trailing cavities remain attached to descending spheres until impact with the container floor, as shown in Figure 4.3a. We decrease the span of hydrophobicity on spheres from $\alpha = 0.50$ to $\alpha = 0.33$ and observe the depths κ and widths λ of cavities are proportional to the coated-diameter αD , as shown in Figure 4.3c and Figure 4.3d, respectively. We elucidate through the derivation of a scaling argument, the relation between coated-diameter αD and cavity depths κ in Section 4.2.2. Spheres coated hydrophobic $\alpha = 0.33$ entering the fluid with hydrophobic surface upward-facing produce surface seals for impacts below $We \approx 1800$, and deep seals above.

Rotating impact orientation of spheres $\beta = 90^\circ$ clockwise such that the line of demarcation is perpendicular to the free surface generates asymmetric deep seal cavities and nonlinear subsurface sphere trajectories, as seen in Figure 1.3d. Spheres migrate from straight-line entry due to the generation of lift forces \mathcal{L} acting perpendicular to gravity. The displacement produced by this uneven cavity formation is more pronounced for impacts below $We \approx 1800$. The role of the hydrodynamic force associated with the lift \mathcal{L} experienced by spheres is further discussed in Section 4.2.3. As spheres descend, air-entrainment is concentrated along hydrophobic hemispheres [25], shifting spheres laterally by up to 2–diameters for impacts below $We \approx 1800$. For increasing

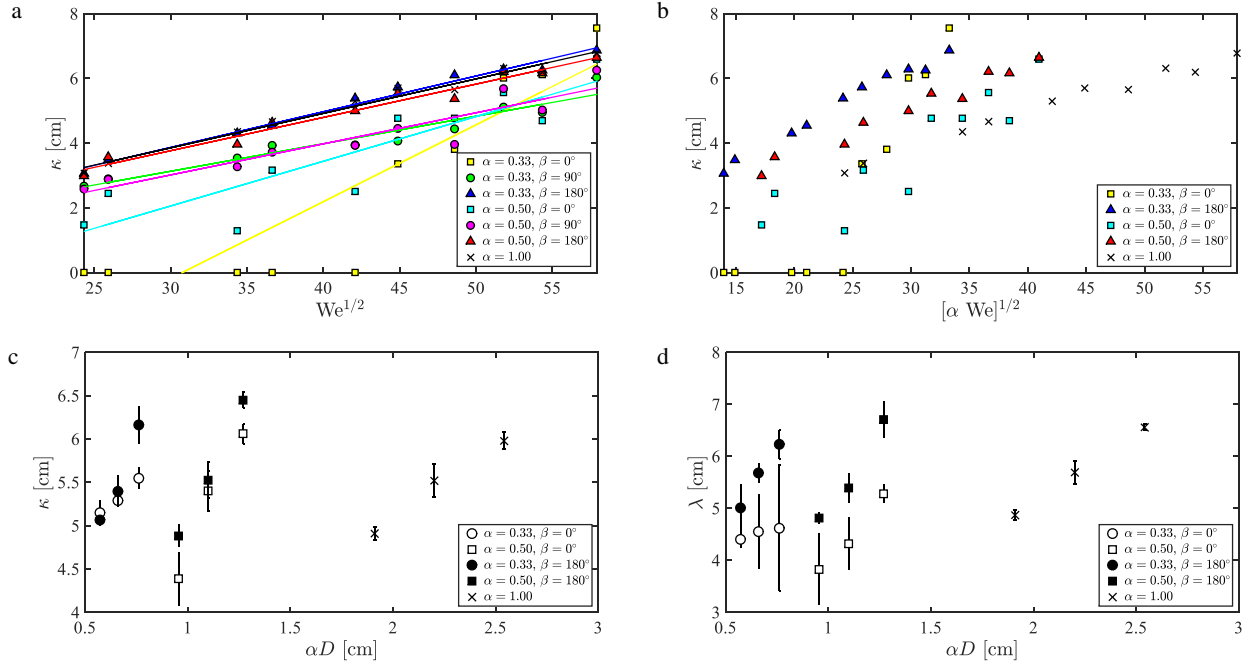


Figure 4.3: Aggregated plots of cavity depths κ versus (a) $We^{1/2}$ and, (b) $(\alpha We)^{1/2}$. Cavities arising from the water entry of hemispherically-coated spheres may be described by $\kappa \sim (\alpha We)^{1/2}$ for low impact velocities, and $\kappa \sim We^{1/2}$ for increasing entry speeds. Cavity (b) depths κ , and (c) widths λ versus coated-sphere diameter αD for heterogeneous spheres with the line of demarcation parallel to the free surface at water entry. Spheres tested have impact velocity $U = 2.4$ m/s.

We, inertial effects dominate hydrodynamic forces imposed by an anisotropic pressure distribution with spheres maintaining a nearly vertical descent as seen in Figure 4.2b. The temporal evolution of an $\alpha = 0.50, \beta = 90^\circ$ sphere experiencing lateral translation is displayed in Figure 4.2a. After pinch-off, cavity lift forces diminish. Smooth cavity walls develop on the hydrophobic portions of descending spheres whereas cavity walls with surface waves emanate from hydrophilic hemispheres prior to cavity collapse. The curvature of sphere trajectories during air-entrainment reduces deep seal cavity depths κ relative to homogeneous cavity-producing impactors traveling along the straight-line axis, as seen in Figure 4.3a. Spheres with $\alpha = 0.50, \beta = 180^\circ$ (Movie C4) yield qualitatively similar results as homogeneous hydrophobic spheres shown in Figure 1.3b. However,

unlike homogeneous spheres, trailing cavities are not stable-streamlined [14] post-pinch-off.

Above the free surface, splash crowns are influenced by impact orientation β as shown in Figure 4.2c. When $\beta = 0^\circ$ a radial splash crown ascends vertically upward and an axisymmetric Worthington jet propagates along the axis of fluid entry. For $0^\circ < \beta < 180^\circ$ we note a lopsided crown, where amplification of the crown corresponds to the hydrophobic portion. We rationalize this observation by noting previous studies find that splash crowns from homogeneous hydrophobic impactors are higher than their hydrophilic counterparts [41, 28, 31]. Non-uniformity experienced during splash crown ascension indicates non-axisymmetric fluid displacement.

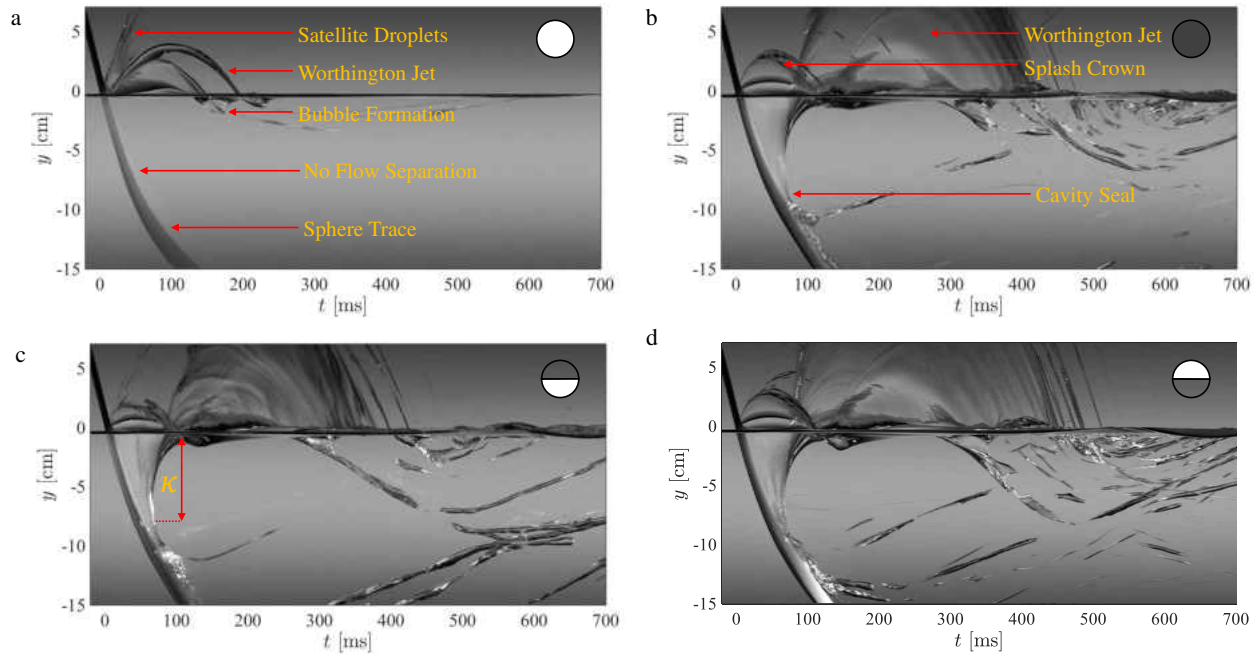


Figure 4.4: Spatiotemporal diagrams [2] showing water entry dynamics of a (a) fully hydrophilic sphere, (b) fully hydrophobic sphere, (c) heterogeneous sphere, $\alpha = 0.50$, $\beta = 0^\circ$; and (d) heterogeneous sphere, $\alpha = 0.50$, $\beta = 180^\circ$. The water entry dynamics of a heterogeneous sphere, $\alpha = 0.50$, $\beta = 90^\circ$ is shown in Figure 4.6. Spheres pictured have diameter $D = 2.54$ cm and $We = 2014$.

Flow visualization typically involves camera captures [26] as shown in Figure 1.3, and the temporal evolution of air-entraining cavities generally displayed by adjoining a few consecutive frames,

as displayed in Figure 4.2a. To better differentiate water entry dynamics of hemispherically-coated spheres, vertical slices of video sequences of 3 pixel width passing through the sphere’s centerline are placed adjacent to each other with time increasing from left to right as pictured Figure 4.4a–d. These spatiotemporal diagrams, also known as kymographs [2], display the water entry process in its entirety. The kymograph of a purely hydrophilic sphere pictured in Figure 4.4a shows the formation of satellite droplets above surface, and no spatiotemporal disturbance of fluid below surface, except for bubble formation subsequent to the collapse of the Worthington jet at $t \geq 200$ ms. In contrast, cavity-producing cases are characterized by an initial rounded protuberance showing the ascension of the splash crown, followed by a more voluminous protuberance representing Worthington jets that persist beyond $t \approx 450$ ms as shown in Figure 4.4b–d. Worthington jets are also amplified for heterogeneous spheres with downward-facing hydrophilic surfaces (Figure 4.4c) due to the onset of cavity formation at the line of demarcation. Thus, bubble formation is more pronounced when compared to their hydrophilic counterparts (Figure 4.4a) given the increased number of impacting droplets resulting from the Rayleigh-Plateau instability [34] of the Worthington jet. For $\alpha = 0.50$, $\beta = 180^\circ$ (Figure 4.4d), spatiotemporal fluid displacement is qualitatively similar to $\alpha = 1.00$ (Figure 4.4b) with splash crowns ascending beyond $t \approx 100$ ms, and Worthington jets persisting up to $t \approx 500$ ms for both cases. We note the inability to decipher differences in trailing cavities previously detailed above, from the kymographs given our 3 pixel width limitation for video sequences.

4.2.2 *Surface Roughness and Orientation Determine Cavity Depths*

Hemispherically-coated spheres striking a water bath produce air-entraining cavities for all velocities on test at any impact orientation. If the hydrophobic surface is facing downward ($\beta = 180^\circ$), the cavity behaves as if the sphere is wholly hydrophobic as separation begins near the stagnation point. For coating permutations $\alpha = 0.33, 0.50$, cavity depths reflect those of $\alpha = 1.00$, as seen by

the nearly overlapping lines of Figure 4.3a. With the hydrophobic surface facing upward ($\beta = 0^\circ$), the flow remains attached to the sphere according to the predictions of Duez *et al.* (2007) until reaching the line of demarcation, at which point the abrupt change in wetting properties triggers separation at velocities well below that reported by Duez *et al.* (2007) [1] (Figure 4.1b). A sphere coated $\alpha = 0.33$ experiences flow separation at a later time in contrast to one coated $\alpha = 0.50$, producing a narrower cavity that pinches-off at a relatively shallower depth. If the line of demarcation aligns with gravity ($\beta = 90^\circ$), the hydrophobic portion induces flow separation near the south-pole, while the flow remains attached on the hydrophilic portion before eventually separating above the equator. The resulting asymmetric cavities for $\alpha = 0.33, 0.50$, are comparable, as seen in Figure 4.3a. The presence of the cavity produced by the hydrophobic surface triggers cavity migration to the hydrophilic side well below the critical cavity-producing velocity[1], approximately 8 m/s.

Table 4.1: Single-factor analysis of variance test for measured cavity depths κ with respect to $We^{1/2}$.

Coating, α	Orientation, β	Mean [cm]	Linear Fit R^2	Standard Deviation	Standard Error
0.33	0°	2.70	0.81	0.20	0.11
	90°	4.16	0.93	0.11	0.07
	180°	5.20	0.98	0.08	0.05
0.50	0°	3.73	0.79	0.26	0.15
	90°	4.18	0.87	0.08	0.05
	180°	5.01	0.97	0.07	0.04
1.00	-	5.14	0.98	0.06	0.03

The influence of surface treatment on cavity depths can be mathematically characterized by first considering the conical cavity [17] produced behind descending spheres. We expect a scaling of cavity depth to obey $\kappa \sim We^{1/2}$ for a fixed coating and orientation scheme by considering energy conversion, as previously shown by Watson *et al.* (2020)[19]. We plot linear fits of cavity depths κ against $We^{1/2}$ for all impact scenarios in Figure 4.3a. Linear fit correlation values obtained are in the range $R^2 = 0.79 - 0.98$, with individual values, and the results of a single-factor analysis of

variance test [105, 106] given in Table 4.1. While cavity depths are linear with $We^{1/2}$ as evidenced by the convergence of cavity behavior to that of a sphere with $\alpha = 1.00$, as shown in Figure 4.3a, the influence of surface treatment is more pronounced for entry speeds below $We = 2014$. As α increases, leading to greater hydrophobic exposure, so does κ as shown in Figure 4.3c. Thus, to account for the influence of surface coating on cavity depths, we consider the coated-diameter αD and may now write $\kappa \sim (\alpha Dh)^{1/2}$. Accordingly

$$\kappa \sim (\alpha We)^{1/2} \quad (4.1)$$

as shown in Figure 4.3b. For the same $We^{1/2}$, spheres with $\beta = 180^\circ$ produce deeper cavities than those with $\beta = 0^\circ$. For non-hydrophobic-leading impactors, fluid separates based on the location of the line of demarcation such that larger values of α produce wider λ and deeper κ cavities as shown in Figure 4.3c–d.

4.2.3 Submerged Impactors Experience Lift and Drag

To compare hydrodynamic forces induced by surface heterogeneity, we fix $h = 30$ cm such that $U = 2.4$ m/s, ($We = 2014$) and track the center of mass of 2.54–cm spheres as seen in Figure 4.5a and Figure 4.5b. Tracking begins when the center of mass of spheres passes the free surface ($y = 0$) and is terminated just before impact with the floor of the liquid bath ($y > 0$). For impact scenarios where spheres experience lateral displacement, x – and y –position tracks are measured simultaneously (Figure A.9).

The hydrodynamic forces on a spherical projectile entering a liquid bath are an amalgamation of the forces associated with the form drag $F_y = \pi\rho D^2 u(t)^2 C_{Fy}/8$, lift $F_x = \pi\rho D^2 u(t)^2 C_{Fx}/8$, buoyancy $F_B = \rho g(\frac{\pi}{6}D^3 + A(\alpha)y)$, and surface tension $F_\sigma = \sigma\pi D(\alpha - \alpha^2)^{1/2}$ in the direction of travel. The

coefficients C_{F_x} and C_{F_y} are those hydrodynamic forces in the x - and y -directions respectively, $u(t) = (\dot{x}^2 + \dot{y}^2)^{1/2}$ is the instantaneous velocity, \dot{x} and \dot{y} are the first derivatives with respect to time for x - and y -position tracks respectively, and $A(\alpha) = \pi D^2 (\alpha - \alpha^2)$ is the coated cross-sectional area of the sphere at the plane of flow separation. We choose $\alpha = 1.00$ for all $\beta = 180^\circ$ impactors given flow separation at the south-poles. For all other cases, α corresponds to the cross-sectional span of the hydrophobic coating. When present, the force associated with lift F_x acts normal to form drag F_y , and is zero for symmetric pressure distributions around an impactor [22, 36]. A force balance for a sphere of mass m entering the quiescent liquid bath is given by [22]

$$F_x \hat{i} + F_y \hat{j} = mg \hat{j} - (m + m_a)(\ddot{x} \hat{i} + \ddot{y} \hat{j}) - F_B \hat{j} - F_\sigma \hat{j}, \quad (4.2)$$

where \ddot{x} and \ddot{y} are the second derivatives with respect to time for x - and y -position tracks respectively, $m_a = \pi \rho D^3 C_m / 6$ is the added mass which accounts for the effect of accelerating fluid by the descending sphere [17, 19], and $C_m = 0.50$ is the added mass coefficient, treated as a constant value across all impact scenarios [19, 20]. Accordingly, Eq.(4.2) can be decomposed and rewritten as

$$\ddot{x} = -\frac{\rho \pi D^2 C_{F_x}}{8m'} u(t)^2, \quad (4.3)$$

and

$$\ddot{y} = \frac{mg}{m'} - \frac{\rho g \pi D^2}{8m'} \left[\frac{4}{3} D + 2(\alpha - \alpha^2)y + \frac{C_{F_y}}{g} u(t)^2 \right] - \sigma \pi D (\alpha - \alpha^2)^{1/2} \quad (4.4)$$

for computing the hydrodynamic force coefficients C_{F_x} and C_{F_y} , where $m' = m + m_a$. We note the

value of F_{σ} is very small in comparison to the force associated with drag F_y , and the buoyancy force F_B .

To evaluate the derivatives of instantaneous experimental data, we employ numerical differentiation, and smoothing techniques provided by Watson *et al.* (2020)[19]. Our technique maintains the physical integrity of measurements, given our mode of capture using Tracker [18]. In the context of this study, lateral x - and vertical y -displacement measurements are first smoothed with a Savitzky-Golay filter [84] to reduce the influence of experimental error prior to numerical differentiation to obtain temporal velocity \dot{x} and \dot{y} , and then smoothed once more prior to the final differentiation to obtain temporal acceleration \ddot{x} and \ddot{y} .

Table 4.2: Hydrodynamic force coefficients at $Re = 69,000$.

Coating, α	Orientation, β	C_{Fx}	C_{Fy}
0.33	0°	0.00	0.19
	90°	0.50	0.20
	180°	0.00	0.18
0.50	0°	0.00	0.18
	90°	0.05	0.21
	180°	0.00	0.19
1.00	-	0.00	0.18

Numerically solving Eq.(4.3) yields hydrodynamic force coefficients for each entry scenario in Figure 1.3 in the range of instantaneous Reynolds number $Re = \rho Du(t)/\mu = 57,000 - 69,000$, where $\mu = 8.90 \times 10^{-4}$ Pa·s is the dynamic viscosity of water, as plotted in Figure 4.5c and Figure 4.5d. As a further comparison of the hydrodynamic forces imposed on heterogeneous spheres, consider the individual coefficient pairs for $Re = 69,000$ in Table 4.2. Our calculated mean values of $C_{Fy} \approx 0.18 - 0.21$ show that cavity-forming impacts reduce drag when compared to the non-cavity-producing case [19] $C_{Fy} \approx 0.30$. We however note variance in calculated C_{Fy} values for $\beta = 90^\circ$ and $\beta = 180^\circ$ (Table 4.2, Figure 4.5c) are so small, to the point of experimental error,

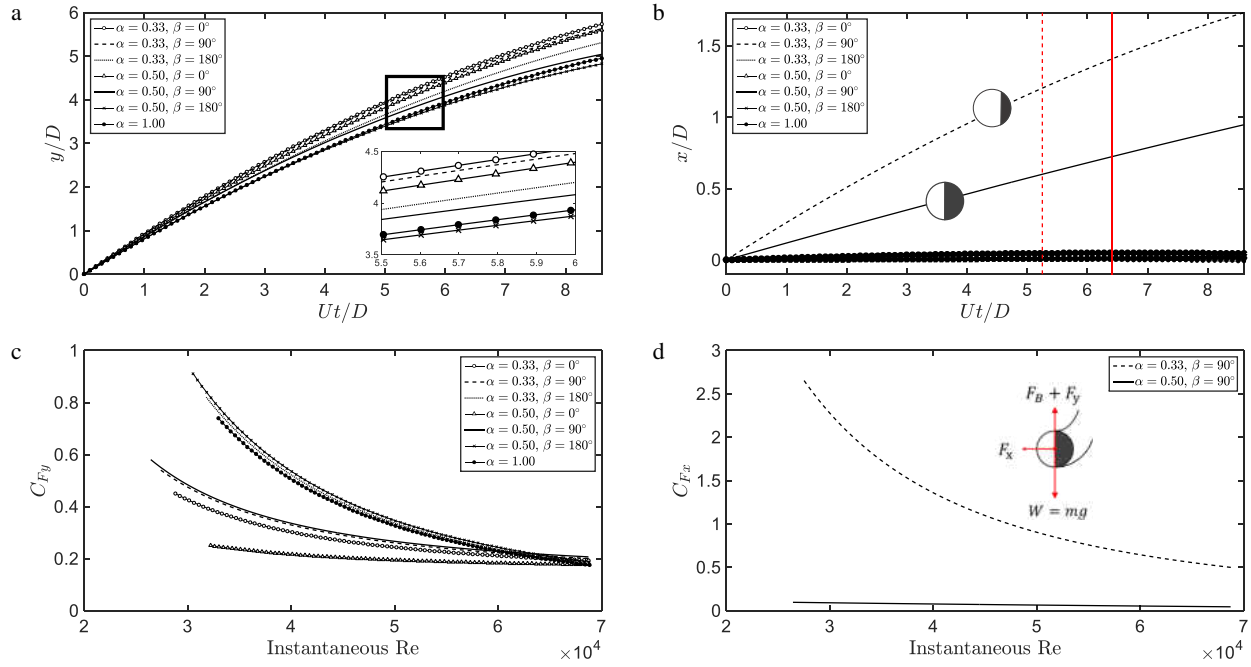


Figure 4.5: (a) Non-dimensionalized vertical y/D and (b) horizontal x/D positions versus dimensionless time. The point at which the sphere's center of mass makes contact with the free surface is chosen as $y/D = x/D = 0$. Vertical lines indicate the dimensionless time Ut/D at which cavity pinch-off occurs. (c) The relation between vertical C_{Fy} and (d) lateral C_{Fx} hydrodynamic force coefficients, and instantaneous Reynolds number Re . Spheres have an impact velocity of $U = 2.4$ m/s.

repeated tests produce slightly different results. Spheres with line of demarcation perpendicular to the free surface $\beta = 90^\circ$ deviate from straight-line trajectories. Analyzing sphere trajectory spatiotemporally (Figure 4.6), the sphere trace gets thinner over time, and super-surface splash features appear lower in height compared to all other cavity-producing cases due to a skewed splash crown and non-vertical Worthington jet. The sphere with $\alpha = 0.33$ experiences the greatest migration with $C_{Fx} \approx 0.50$ when compared to $\alpha = 0.50$ with $C_{Fx} \approx 0.05$, as shown in Figure 4.5d. Spheres with lesser coating allow the hydrophilic side's flow to remain attached over a greater portion of the sphere and thus promote increased fluid momentum over the north-pole, corresponding to more dramatic lateral migration.

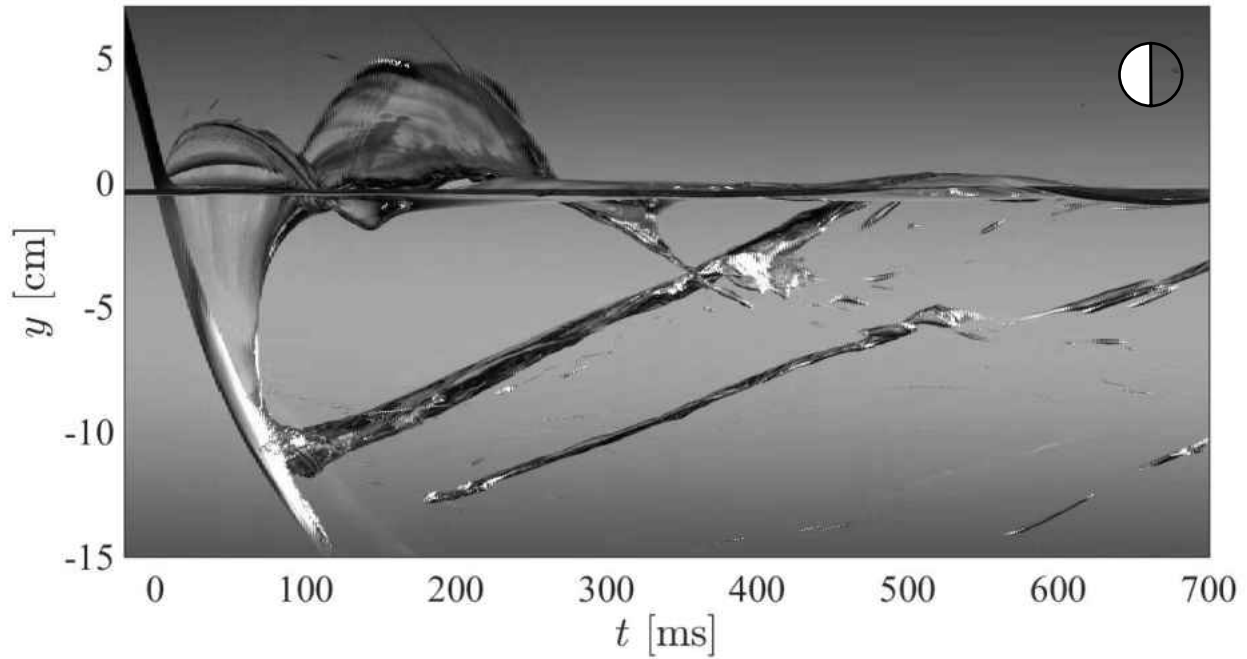


Figure 4.6: Spatiotemporal diagrams [2] showing water entry dynamics of a heterogeneous sphere, $\alpha = 0.50$, $\beta = 90^\circ$. Sphere trace gets thinner over time, and super-surface splash features appear lower in height than all other cavity-producing cases due to a skewed visual perception influenced by lateral sphere migration. Spheres have an impact velocity of $U = 2.4$ m/s.

4.3 Discussion

This study shows that heterogeneous spheres impacting a quiescent unbounded liquid pool produce impactor surface-dependent splash features, and orientation-dependent trajectories. These results may be extended to engineering applications where the drag-reducing benefits of cavity formation is desirable. Biologically, terrestrial and airborne organisms entering the water such as the water boatman [107, 108, 58], the common frog [109, 110, 111], and the American anhinga [112, 113, 114], may benefit from flow separation through surface heterogeneity, thus modulating their underwater acrobatics. Industrially, marine vessels may make use of surface treatments to tune flow separation for economy or performance.

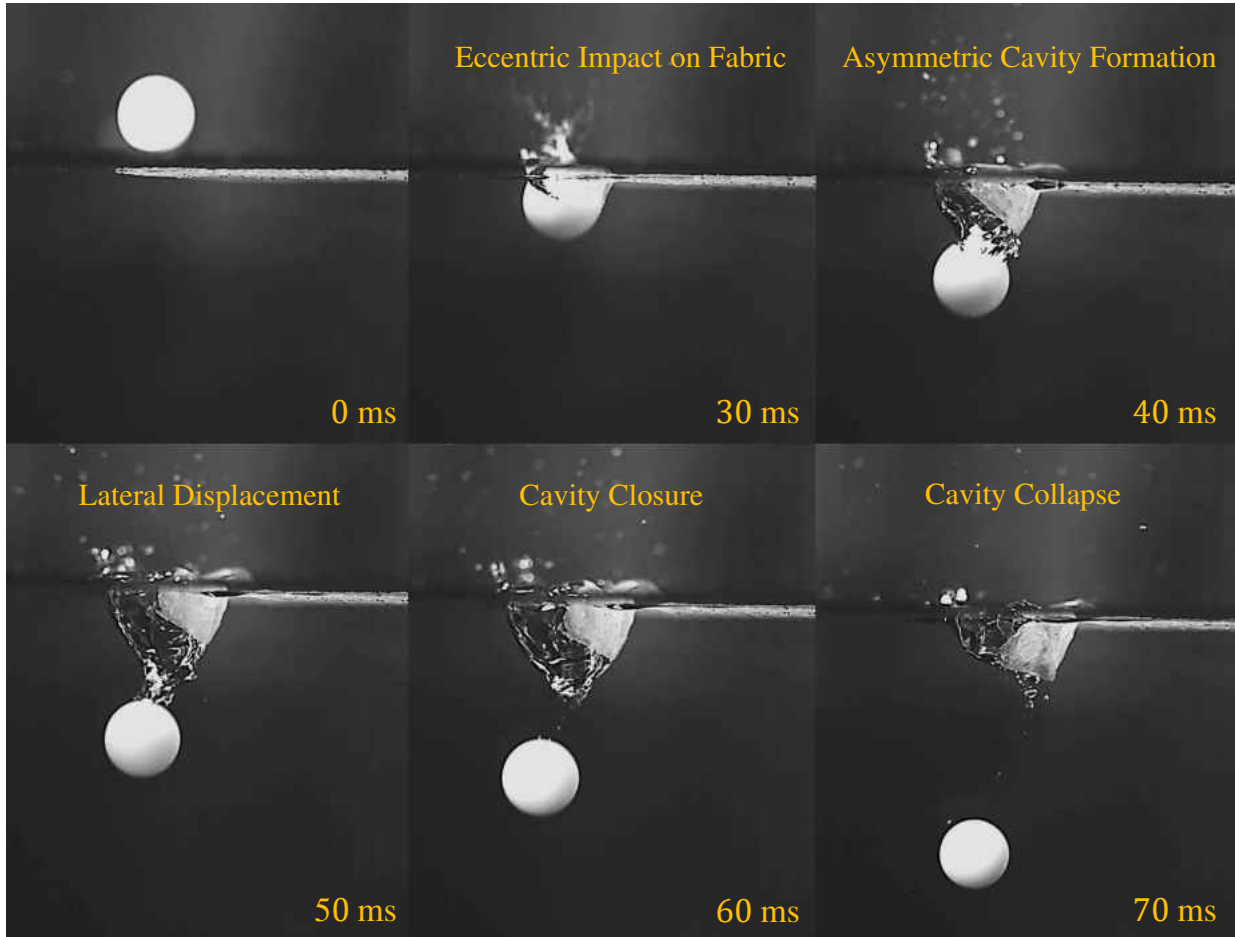


Figure 4.7: Time-sequence of a 2.20-cm hydrophilic Delrin sphere impacting the edge of a single sheet of fabric for $We = 592$. Fabric thickness $\chi = 80 \mu\text{m}$, dry density $\rho''_{\text{dry}} = 2.88 \text{ mg/cm}^2$, wet density $\rho''_{\text{wet}} = 23.00 \text{ mg/cm}^2$, dry failure stress $\sigma_{f,\text{dry}} = 1.20 \text{ MPa}$, and wet failure stress $\sigma_{f,\text{wet}} = 0.09 \text{ MPa}$. Upon sphere impact, an asymmetric cavity originates at the three-phase point of contact with the fabric sheet and promotes lateral translation of sphere trajectory. As the sphere traverses the fluid downwards, force due to buoyancy F_B and drag \mathcal{D} oppose gravitational force W acting on the sphere, and lift force \mathcal{L} acts perpendicular to the velocity U , shifting the sphere laterally from its straight-line trajectory.

Cavities are formed for all permutations of spheres on test with the limit of cavity depths being that of fully hydrophobic spheres. Although on-board measurement of impact acceleration for various coating schemes is an area of future work, we surmise the drag-reducing benefits of flow separation lessens the average impact force up to the moment of cavity pinch-off. However, the correspond-

ing impulse at the moment of liquid contact, not discernible through image analysis, may increase impulse as fluid is forced away from hydrophobic impactors through correspondingly wider cavities. Impulse is likely lower when hydrophilic surfaces first make free surface contact because the fluid is not immediately forced laterally from the stagnation point. Thus the likely optimum for impact force reduction is hydrophilic-down, with the line of demarcation at the equator. Force and drag reduction benefits are, however, not limited to large patches of surface coating. Speirs *et al.* (2018)[115] pre-wetted hydrophilic spheres with a drop of water to trigger cavity formation, thus showing air-entrainment is possible with coatings a fraction the size of ours. The extent to which very small coated areas can produce lateral motion is a topic for further work.

The lateral migration of spheres is not only achievable through impactor surface treatment, but also through the treatment of the free surface with a compliant medium. Eccentric impacts onto thin, non-woven fabrics produce similar outcomes to the those previously identified in this study. We qualitatively examine cavity evolution for a hydrophilic sphere impacting the edge of a fabric sheet at Weber number $We = 592$, as shown in Figure 4.7, and Movie C6 of Appendix A.3. The time between successive images is 10 ms. Upon fluid entry, flow separation is initialized only along the fabric side of the sphere. Impact velocity $U = 1.4$ ms is well below the threshold velocity [1] $U \approx 8$ m/s required for air-entrainment by completely hydrophilic spheres. An asymmetric cavity is fully formed after $t \approx 50$ ms, akin to localized half-cavities discussed in Section 4.2.1, and lift is generated as a result. The influence of the cavity on sphere trajectory diminishes beyond the point of pinch-off ($t \geq 60$ ms), beyond which descent is purely vertical. Similar to the water entry of hemispherically-coated spheres, an increase of the entry speeds promote greater inertial effects, and reduces the role of eccentricity on lateral migration [22, 36]. The efficacy of asymmetric cavity formation by established cavity-forming techniques warrants further comparison and investigation.

4.4 Chapter Summary

Hydrophilic spheres made heterogeneous spheres by selectively coating hydrophobic produce air-entraining cavities with textures and metrics dependent on the area of surface treatment and impact orientation. All spheres on test experience drag reduction as a result of the partial hydrophobic coating, regardless of impact orientation. Spheres with downward-facing hydrophilic surfaces experience flow separation at the line of demarcation between the north and south-poles, surface waves on cavity walls, and stable-streamlined trailing cavities. On the contrary, with downward-facing hydrophobic hemispheres, flow separates near the stagnation point while producing smooth cavity walls and unstable trailing cavities. Generally, increases in the coated-diameter and spheres hydrophobic-down promote wider and deeper cavities. Water entry with a vertical demarcation line skews super-surface splash features, and produces sphere migration from a straight-line trajectory, where a reduction in the coated-diameter yields greater lateral displacement. Splash features and impactor motion may thus be tuned by surface heterogeneity.

CHAPTER 5: LIFE ON STORMY SEAS: WATER STRIDERS ARE IMPERVIOUS TO RAINDROP IMPACTS

Water striders are abundant in areas with high humidity and rainfall. Raindrops can weigh 42 times the adult strider and some pelagic species spend their entire lives at sea, never contacting ground. In this combined experimental and theoretical study, we use high-speed videography to film drop impacts on water striders and dynamically-scaled mimics for Weber number $We \approx 2150$. Drops force the insect subsurface upon direct contact. As the ensuing cavity collapses, the water strider is shot into the air by a Worthington jet. We show the water strider's locomotive responses, low density, resistance to wetting when briefly submerged, and ability to regain super-surface rest state, render it impervious to impacting water drops. When pulled subsurface during secondary cavity formation, water striders face the threats of being ejected above surface, or submerged below surface. Striders trapped within the gas-filled cavity are expelled from the liquid bath with the ensuing Worthington jet. Water striders with center of mass below the air-water interface of the secondary cavity wall remain submerged due to the rapid collapse of the cavity causing separation from the insects. Submersion makes the water strider poised on penetrating the air-water interface from below, which appears impossible without the aid of a plastron, or proper locomotive techniques. Submerged water striders employ a series of power strokes in locomoting the aquatic environment. Drops impacting the fluid several body lengths away from water striders elicit escape jumps as striders maneuver surface perturbations. Our results show water striders are robust to adverse super-surface conditions and augur well for the development of biomimetic robots.

5.1 Experimental Techniques

5.1.1 *Insect Capture and Care*

Water striders of non-distinguished age and sex are captured from a pond at the University of Central Florida's arboretum, and housed in an 80-cm² tempered-glass aquarium with 16 hours of light and 8 hours of darkness in keeping with environmental conditions of the natural habitat. No permission is required to collect water striders as the present study does not involve regulated, endangered or protected species. Captured water striders demonstrate their typical life processes within the lab, mating, and shedding exoskeletons during maturation. The dwelling environment is maintained at $25^{\circ}\text{C} \pm 2^{\circ}\text{C}$ and striders fed with dead mosquitoes. The water bath is kept sanitary using a Cobalt Aquatics Clear Vue underwater filter to prevent the build-up and growth of bacteria. Water strider mass and compressibility are measured using a Sartorius Secura 225D-1S analytical balance, and microscopic images recorded using a Keyence VHX-900F digital microscope.

5.1.2 *Impact Trials and Visualization*

Water striders are captured from the aquarium and transferred to a 6-cm wide, 10-cm deep impact chamber affixed to a Nexus 3' x 6' optical table as shown in Figure 5.1a. Up to 20 water striders are employed per impact trial covering approximately 22% of the available free surface area which in turn increase the probability of drop collision, while allowing the insects to roam unabated. Striders are tested for the entire duration of daily experimental trials. High-speed impacts $\sim O(10^{-3})$ s render water striders non-evasive to oncoming drops. To probe drop impacts onto inanimate objects resting atop the fluid, we anesthetize water striders with carbon monoxide, and in other cases, substitute striders with floating cylindrical silicone rods of similar length and mass. Silicone rods are made hydrophobic by spraying with Rustoleum NeverWet. A 10-mL syringe connected

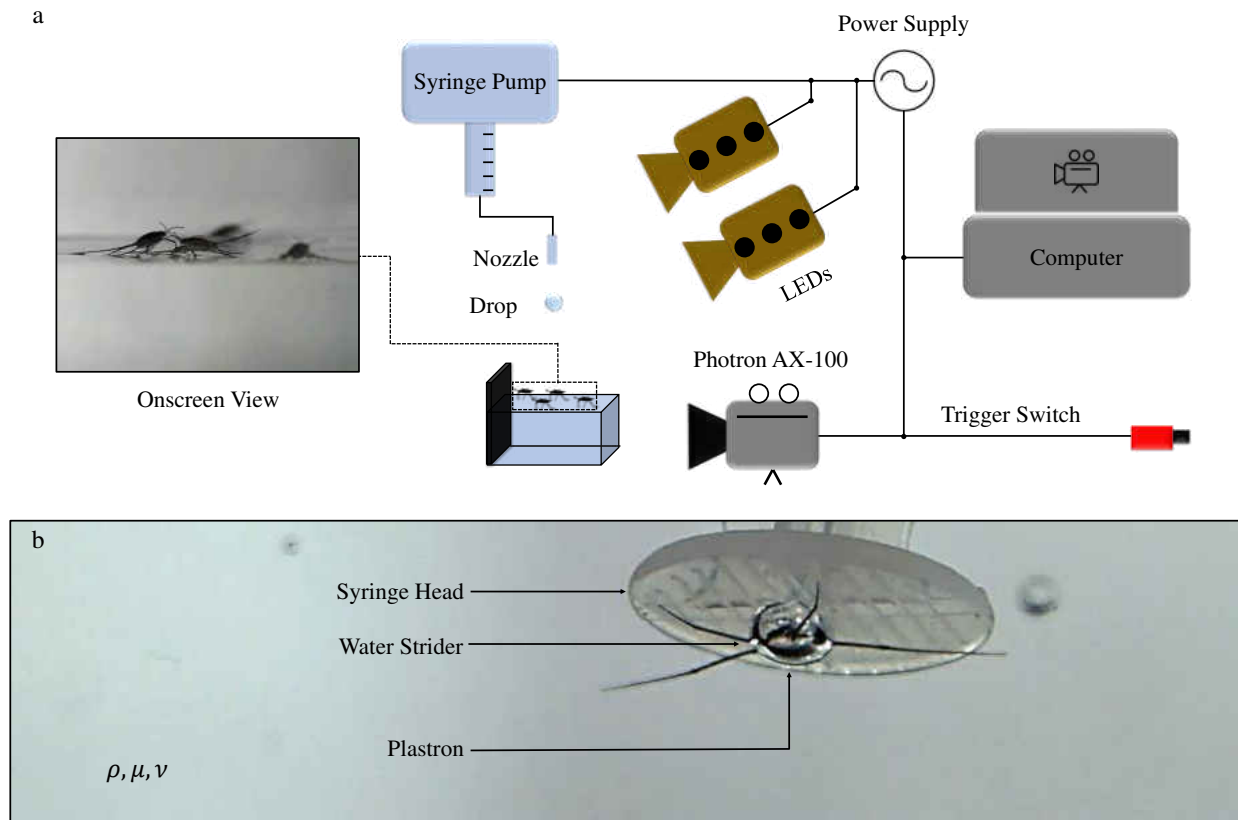


Figure 5.1: (a) Schematic of experimental setup. A Photron Mini AX–100 high-speed video-camera captures frontal views with diffuse lighting positioned behind the impact zone and above the camera. Optional trigger switch complements manual controls in video recording software on computer. (b) Plastron (air bubble) forms around water strider as syringe head pushes the insect beneath the free surface. Densely-packed micro- and macro-hairs populate the water strider exoskeleton such that water contact angle [3] exceeds 150° . Corresponding video is Movie D3.

to a New Era NE–1010 syringe pump is used to generate drops at a flow rate of 5 mL/min from a nozzle situated $h = 1.75$ m above the liquid bath. Impact force measurements are measured using a MARK–10 Series 7 M7–012 force gauge, which records force readings at 14,000 Hz. The force gauge is calibrated by conducting checks with rigid bodies of known masses. Impacts occur opportunistically, and collisions captured with a Photron Mini AX–100 high-speed video-camera at 3200 frames per second with resolution of 1280×1024 pixels using a 120–mm Nikon lens.

Our chosen field of view is $6.5 \times 6.2 \text{ cm}^2$, yielding an 180 pixel/cm magnification. Impacts are illuminated by a pair of GS Vitec Multi-LED lights. We extract geometric measurements from videos using Open-Source Physics Tracker. Cavity and strider kinematics are obtained through image processing in MATLAB [17, 18, 19]. Strider impact area assessments are conducted using the Java-based image processing program, ImageJ.

5.2 Experimental Results

We conduct drop impact trials with impact velocity $U = 6.01 \text{ m/s} \pm 0.34 \text{ m/s}$ ($N = 10$), and diameter $D = 4.34 \text{ mm} \pm 0.04 \text{ mm}$ ($N = 10$) such that $We \approx 2150$, and observe 47% direct impacts (Sections 5.2.1 to 5.2.4), and 53% near misses. We segregate impact sequence into two phases. The first phase or ‘primary splash’ begins at water strider drop contact and ends when the first Worthington jet reaches peak height δ_1 . The second phase or ‘secondary splash’ begins with the descent of the primary Worthington jet, in-turn forming a second cavity, and ends when the second Worthington jet reaches peak height δ_2 . Measurements ($N = 10$) for primary cavity depths $\kappa_1 = 14.8 \text{ mm} \pm 1.5 \text{ mm}$, primary cavity widths $\lambda_1 = 23.4 \text{ mm} \pm 3.1 \text{ mm}$, and primary Worthington jet heights $\delta_1 = 32.4 \text{ mm} \pm 3.6 \text{ mm}$ are obtained by extracting dimensions as shown in Figure 1.5c. Overall, primary splash features are more than 3X the water strider body length L . During direct impacts the low mass of water striders ensure depression with the free surface into the air-cavity, and ejection above the quiescent fluid by the subsequent Worthington jet (Movie D4). Collapse of the primary Worthington jet creates secondary splashes that eject 67% (Movie D4) and submerge 33% (Movie D1) of water striders undergoing direct impact by drops. Drops missing striders by more than a body length create surface waves and satellite droplets inciting water striders to jump away from the oncoming wave (Movie D5).

5.2.1 Raindrop Collisions

The likelihood of raindrop impacts can be predicted by considering the plan view area of water striders as seen by a falling raindrop. The strider's exoskeleton including the legs has impact area in the range $A_s = 34 - 165 \text{ mm}^2$. Impact area varies depending on drop size D , and is determined by first tracing the body of the strider with the desired drop as shown in Figure A.10. The area of the drop trace is then obtained graphically using ImageJ. Raindrop collisions within the impact area are considered direct impacts. The water strider's legs account for 80% of the impact area, while the torso only accounts for 20%. During the heaviest rainfall [4, 5] with drops of mass $m = 16 \text{ mg}$, falling with an intensity [6] $I \approx 50 \text{ mm/h}$, a resting water strider will experience impacts on average every $\Delta t = m/(I \cdot \rho \cdot A_s) \approx 7 \text{ s}$, considering the entire impact area of the insect $A_s = 165 \text{ mm}^2$, and direct torsal impacts every $\Delta t \approx 34 \text{ s}$, where $A_s = 34 \text{ mm}^2$. Thus, it is highly likely water striders will be struck by drops during rainfall.

5.2.2 Primary Cavity Formation

Upon impact, non-evasive striders are pushed downward a distance of several body lengths L at the same speed as—and along the periphery of the expanding cavity as shown in Figure 5.2a. We note the shape and dimension of air-entraining cavities are unaltered when water striders are present, and observe the formation of a plastron during subsurface transport. An example of the plastron around the body of the insect is shown in Figure 5.1b and Movie D3. Strider density $\rho_s = M/V_s \approx 410 \text{ kg/m}^3$ such that subjects remain neutrally-buoyant during free surface depression with minimal inertial penalty experienced by the growing cavity. We choose the free surface as $\lambda_1 = \kappa_1 = 0$ and track the growth of air-cavities for the first 9 ms of impact with sub-pixel accuracy of 180 pixel/cm as pictured in Figure 5.2b to determine the horizontal $\lambda_1(t)$ and vertical fluid displacements $\kappa_1(t)$ —Figure 5.2c, cavity velocity $u_{c,1}(t)$ —Figure 5.2d, and cavity acceleration $a_{c,1}(t)$ —Figure 5.2e. Thus,

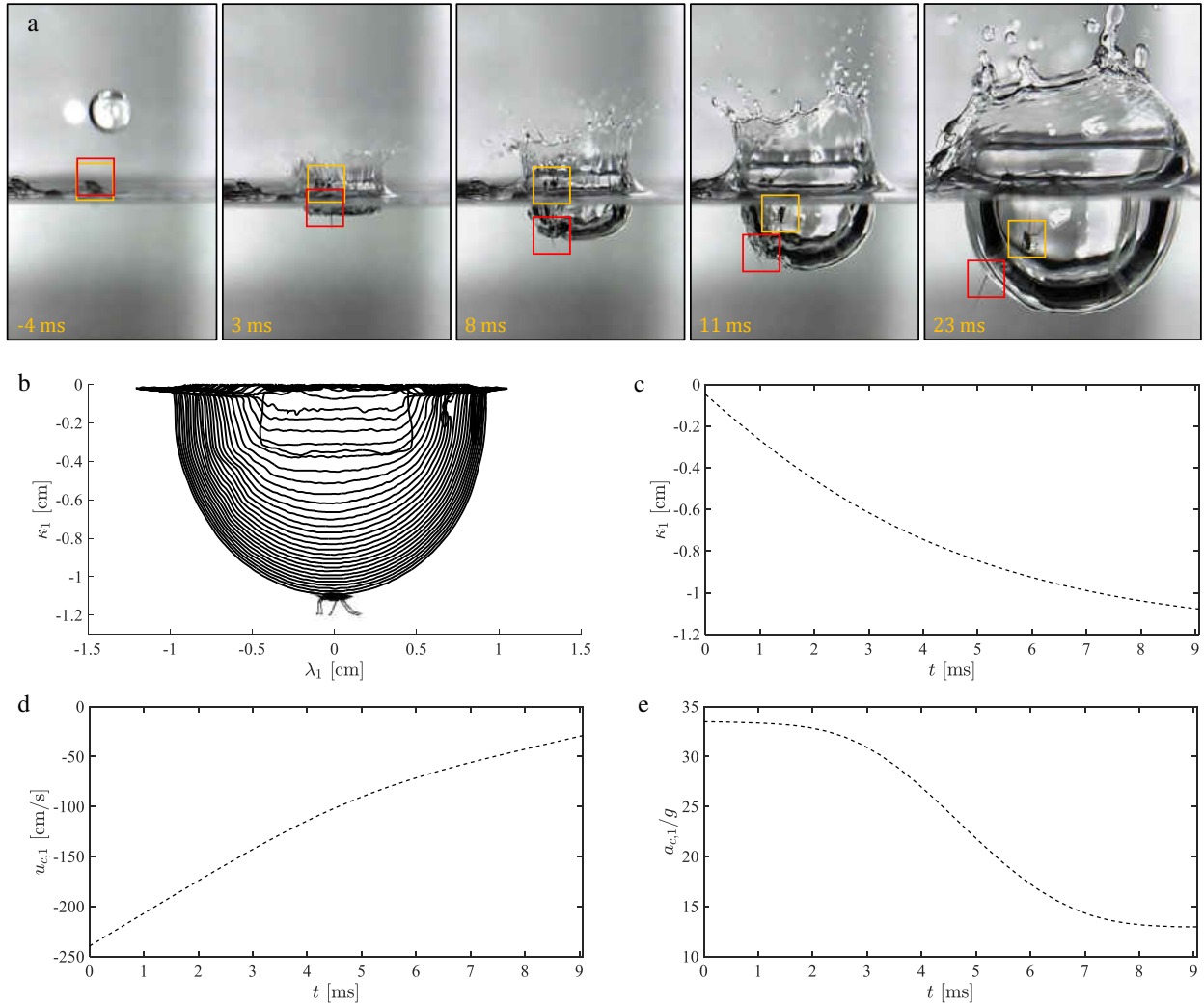


Figure 5.2: (a) Drop impact incites cavity formation. Water striders behave as passive particles due to their low inertia, and are pushed downward a distance of several body lengths at the same speed as, and along the periphery of the expanding cavity. (b) Cavity expansion subsequent to drop impact. Cavities are tracked with sub-pixel accuracy of 180 pixel/cm at 3200 frames per second. (c) Cavity depth κ_1 , (d) velocity $u_{c,1}$, and (e) acceleration $a_{c,1}$ versus time. Cavity kinematics are unaltered by the presence of water striders along the cavity, and are representative of the displacement, velocity, and acceleration of a strider impacted by a drop. Drop impact pictured has $We \approx 2150$.

we may characterize the kinematics of water striders found at the bottom-most-tip of cavities. Image subtraction is used to acquire the trace of cavities and jets from consecutive frames, and

a quintic spline used to produce smoothed first and second order derivatives. The image cross-correlation and derivative-finding procedures are explained in detail by Ruiter *et al.* (2010) [116, 117] and Epps *et al.* (2010) [97] respectively.

At the moment of drop contact with the free surface, an air-cavity is initiated with velocity $u_{c,1} \approx 2.5$ m/s as shown in Figure 5.2d. The cavity velocity represents a 58% reduction when compared to the drop impact velocity $U = 6.01$ m/s. As such, the acceleration felt by a resting water strider is $a_{c,1} = 3.3 \times 10^4$ cm/s², the equivalent of 34 gravities (Figure 5.2e), and maximum inertial force experienced during subsurface transport is $F = M \cdot a_{c,1} \approx 213$ dynes. At a first glance, it appears this force is high relative to the striders' weight of 6 dynes. However, given the compliant nature of the free surface, momentum is transferred to the liquid bath during cavity formation and a portion redirected upwards with the ascending splash crown such that the inertial force experienced by impacted water striders is reduced compared to rigid surfaces [6] and all striders on test survive initial drop collision. Striders experience less than half the inertial force $F \leq 600$ dynes felt by flying insects during rainfall [6]. The impact force of a liquid drop striking a non-compliant surface such as floating vegetation is given by $F = 2 \cdot m \cdot U^2 / D \approx 7 \times 10^4$ dynes, 329 times greater than the inertial force experienced atop the water bath. To confirm survival in the range of impact forces $F = 10^1 - 10^5$ dynes, spanning impacts atop compliant and non-compliant surfaces, we perform compression tests [6] using the analytical balance to determine the strider's threshold to force. Water striders are subjected to a sustained compressive force F_{comp} and survive the upper limit of impact forces during rainfall $F_{\text{comp}} = 1.5 \times 10^5$ dynes, beyond which striders are crippled and tend to die. As such, we confirm the strider's ability to support large loads [6]. Given these values are orders of magnitude larger than the impact forces applied by raindrops, we conclude that a resting water strider atop an aquatic habitat is impervious to initial raindrop collision.

5.2.3 Primary Cavity Collapse and Worthington Jet Formation

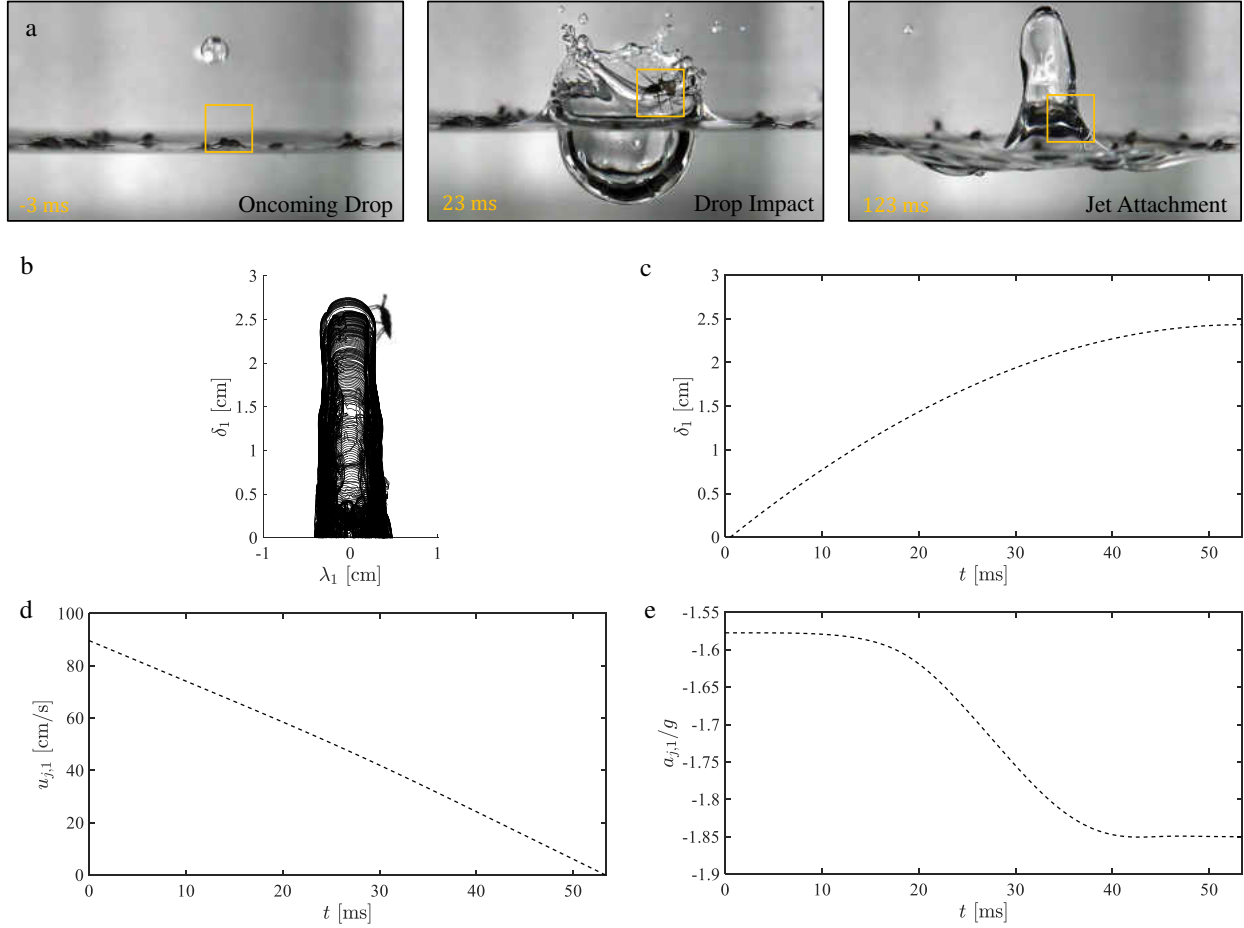


Figure 5.3: (a) Primary splash showing a free-falling drop approaching water striders atop the quiescent liquid bath. An air-entraining cavity and Worthington jet are formed after drop impact at $We \approx 2150$. The low mass of the water strider ensures resulting inertial forces are low, despite high impact accelerations, enabling the insect to survive the initial drop collision, while passively moving with the resulting splash. (b) Worthington jets are tracked with sub-pixel accuracy of 180 pixel/cm at 3200 frames per second. (c) Jet height δ_1 , (d) velocity $u_{j,1}$, and (e) acceleration $a_{j,1}$ versus time. Worthington jet kinematics are unaltered by the presence of water striders along the lamellae, and are representative of the displacement, velocity, and acceleration of a strider propelled above the free-surface.

Clearly, water striders benefit from the force-reducing characteristics of the free surface, but are also robust to raindrop impacts up to $F_{\text{comp}} < 1.5 \times 10^5$ dynes while located atop non-compliant

surfaces such as floating vegetation in marine habitats. Now that we have demonstrated that inertial force at impact (Figure 5.3a) is not a threat to survival, we turn our attention to the next phase of drop impact. Worthington jets are formed subsequent to the collapse of air-entraining cavities as shown in Figure 5.3a. Water striders just beneath the walls of gas-filled primary cavities are propelled super-surface with the ensuing primary jets as pictured in Figure 5.3b. Given energy dissipation into the surrounding fluid during cavity expansion, primary jets ascend with initial velocity $u_{j,1} = 0.9$ m/s (Figure 5.3d), representing 64% reduction compared to $u_{c,1} = 2.5$ m/s. We note that the creature's location on the jet is a function of where the drop hits the strider. Worthington jets widen during ascension as seen from the trace in Figure 5.3b, and overall characteristics unaltered by the presence of a single water strider.

Striders are generally attached to Worthington jets along the exoskeleton. In very few trials, water striders actively separate from Worthington jets by jumping as shown in Movie D6. Active separation is attainable when the legs of water striders rest on the Worthington jet, and ventral areas elevated above the fluid, akin to the striders' rest position atop horizontal surfaces. Given that water striders are in contact with the moving fluid, escape jumps detaching striders from Worthington jets differ from jumps on horizontal surfaces when escaping predators [12]. In Movie D6, upward momentum of the Worthington jet, and a single power stroke propels the water strider mid-air at approximately 18 m/s^2 , causing the insect to rotate 360° before falling to the free surface. Striders attached to the reclining Worthington jet, and those onto which jets collapse are subsequently entrapped below the free surface as shown in Figure 5.4, but maintain dryness given the superhydrophobicity of the insect [3]. Thus, while water strider escapes from primary Worthington jets occur opportunistically, this splash feature incites minimal threat to the well-being of the insect group, and serves mainly as a transitory phase for sub- and super-surface exposure.

5.2.4 Secondary Cavity Formation and Collapse

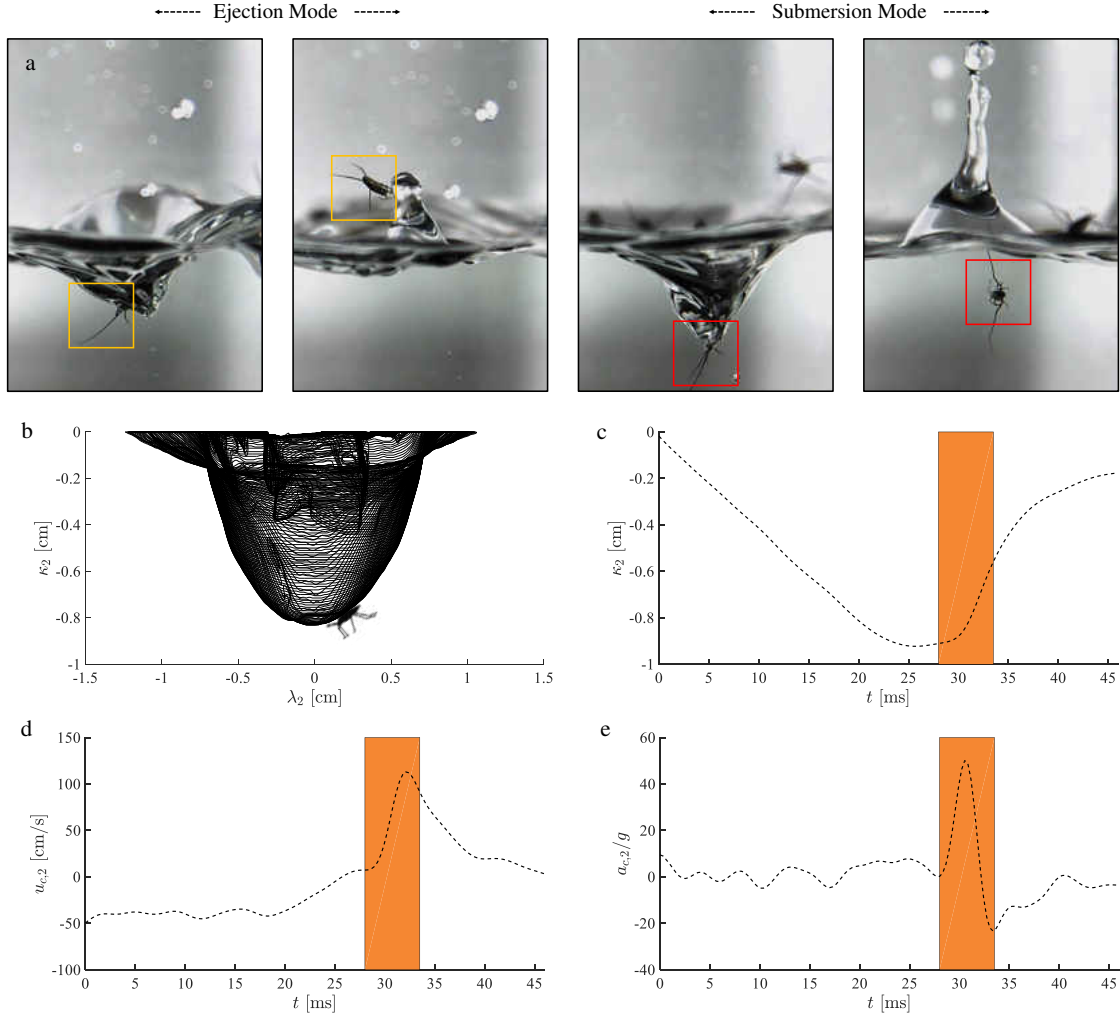


Figure 5.4: (a) Secondary splash showing an adult water strider trapped within a gas-filled cavity, ejected with the ensuing Worthington jet, pushed subsurface along the cavity wall, and submerged by the rapidly collapsing cavity for $We \approx 2150$. Water striders with center of mass above the air-water interface of gas-filled cavities are propelled above the free surface with ascending secondary Worthington jets. In contrast, striders with center of mass below the air-water interface of cavities are left submerged due to the precipitous collapse of secondary cavities. Corresponding videos are Movies D4 and D1. (b) Secondary cavities are tracked with sub-pixel accuracy of 180 pixel/cm at 3200 frames per second. (c) Cavity depth κ_2 , (d) velocity $u_{c,2}$, and (e) acceleration $a_{c,2}$ versus time.

We observe two modes of impact outcomes when water striders interact with secondary cavities as shown in Figure 5.4a, namely ejection and submersion. Water striders with center of mass above

the air-water interface of gas-filled cavities, 67% of impact trials, $N = 16$) are propelled above the free surface with ascending secondary Worthington jets. In contrast, striders with center of mass below the air-water interface of cavities, 33% of impact trials, $N = 8$) are left submerged due to the precipitous collapse of secondary cavities. This observation is made more lucid by the frame-by-frame tracking of the secondary cavity as shown in Figure 5.4b. The secondary cavity grows for $t \approx 27$ s after which it precipitously retracts back to the free surface (Figure 5.4c) with peak velocity $u_{c,2} \approx 100$ cm/s (Figure 5.4d) and peak acceleration $u_{c,2} \approx 50$ g (Figure 5.4e).

5.3 Discussion

This study shows that mesoscale organisms and floating particles can be submerged during rainfall. When water striders and their mimics retreat into the fluid during secondary cavity formation, we observe ejection with the ensuing Worthington jet for striders trapped within the gas-filled cavity, and submersion for striders with center of mass along the periphery of the cavity wall, attributed to the precipitous retraction of the fluid towards the free surface. Drop impact outcomes are influenced by the low mass, and water-repellent nature of water striders, but the probabilistic positioning of water striders relative to the secondary cavity is significant. While all striders on test are superhydrophobic, we expect purely hydrophilic particles to be more susceptible to submersion. Thus, the relation between wetting properties of floating particles and splash dynamics is an area of further investigation. Furthermore, floating debris such as micro-plastics in the ocean with greater length scales and mass tend towards the limit of objects with inertia much greater than that of a raindrop, and would therefore be void of the threat of submersion by rainfall. These large-scale debris nonetheless enter the hydrosphere due to turbulence experienced during adverse environmental conditions. The transition between the limit of raindrop-susceptible and turbulence-susceptible debris is not yet understood, and is an area of future work.

Water striders survive initial drop impact by virtue of their incompressibility to large loads, and momentum transfer between the raindrop and compliant fluid surface. Upon impact, more energy is imparted to the fluid to produce cavities and Worthington jets, than energy transferred to water striders. Given that rain consists of repeated numbers of free-falling drops, we expose water striders to higher-frequency drop impacts to test survivability (Movie D7). Torrential downpour increases the cohort of submerged water striders as insects repeatedly impacted by drops can become wetted. High-frequency drop impacts promote the deterioration of the protective plastron around the insect, and makes it difficult for water striders to regain super-surface positioning. We note the propensity of submerged water striders to remain beneath the free surface for the duration of the adverse above-surface conditions. This behavior is beneficial to water striders since peak impact acceleration of drops occur at the point of water entry. As such, striders experience increased force reduction subsurface despite increased drop frequency [47]. Speirs *et al.* (2019) [47] showed reduced impact forces on rigid spheres placed inside a stream of fluid striking the quiescent water surface. Submerged water striders survive beyond 10 minutes, and locomote just below the free surface by applying a series of power strokes (Movie D8). Super-surface positioning is regained when striders apply power strokes at acute angles relative to the free surface.

Splash dynamics are influenced by drop impact velocity, and fluid properties. In our study we observe the kinematics of secondary cavities and jets vary from their primary counterparts given energy conversion and surface elasticity. While the initial drop impact is generally understood from the compendium of fluid engineering research, the characterization of later-stage cavities and jets warrant further studies.

5.4 Chapter Summary

Water striders are impervious to raindrop collisions. Drop impacts onto and in the vicinity of water striders resting atop a free surface do not elicit an escape response likely due to the high velocity of oncoming drops. The compliant nature of the free surface and water strider mass ensure resulting inertial forces are low, despite high impact accelerations, enabling water striders to survive initial raindrop collisions, while passively moving with the resulting air-cavities and Worthington jets. When submerged, a plastron forms around the strider's body that protects the creature from saturation and drowning. The highest danger of submersion occurs upon the retraction of the secondary cavity. The characteristically rapid collapse of secondary cavities often leaves water striders submerged. Secondary cavities are narrower, and collapse more rapidly than their primary counterparts due to higher surface tension forces. As such, water striders with center of mass below the air-fluid interface of secondary cavities are separated from the precipitously retracting fluid, whereas those with center of mass above the air-fluid interface are expelled into mid-air with the protruding Worthington jet. Despite disruption of the plastron during torrential downpour, water striders are able to dwell and locomote subsurface for a relatively long period of time, and regain super-surface equilibrium by applying a series of power strokes at an acute angle relative to the air-fluid interface.

CHAPTER 6: CONCLUDING REMARKS

We have detailed the results of this combined experimental and theoretical body of work on the water entry dynamics of spherical projectiles across different initial surface conditions. In Chapter 2, we showed how small amounts of layered non-woven fabric sheets incite flow separation for hydrophilic Delrin spheres otherwise not attainable below impact velocities of 8 m/s [1]. Splash crowns were suppressed by the punctured fabrics and Worthington jets amplified as fluid flowed through punctured openings. We derived a scaling argument to show the relation between drop heights h and maximum Worthington jet heights H_{\max} such that $H_{\max} \sim h$. The inclusion of fabrics granted spheres the drag-reducing benefit of flow separation while increased layering made fabric penetration more difficult, amplified hydrodynamic drag force, and in some cases completely halted sphere descension as shown in Figure 1.1d.

In Chapter 3, we extended our work with fabrics by considering four commercial-grade household products. Fabrics varied in puncture resistance as denoted by their failure stress σ_s and wet area density ρ''_{wet} which in-turn aided our understanding of the physics at the transition between fabrics which were punctured and those that remained intact after impacts. We provided the first documented observation of air-entraining cavities bounded by the thin fabrics onto which steel spheres made impact and classified these as ‘fabric cavities’ [19]. Our results showed that as the failure stress of fabrics increased, so did fabric cavity depths κ_f and maximum Worthington jet heights H_{\max} . Accordingly, scaling arguments proved $H_{\max} \sim \kappa_f$ in all except the case of toilet paper where trailing cavities dominated Worthington jet formation such that $H_{\max} \sim \kappa_t$, where κ_t is the length of the trailing cavities. Similar to the previous chapter, we modeled sphere hydrodynamics and showed that fabrics amplified and attenuated hydrodynamic drag based on material properties.

In Chapter 4, the water entry dynamics of Delrin spheres with heterogeneous wetting proper-

ties were examined and spheres tested across a range of impact orientation β , entry speed U , and coated-diameter αD . As such, the study probed an alternative approach for tuning splashes and impactor trajectory. For impactors entering the fluid at $\beta = 90^\circ$, flow separation were induced across the hydrophilic surface at impact velocities well below the threshold required for air-entrainment by completely hydrophilic spheres due to cavity formation across the hydrophobic portion. These impactors experienced asymmetric cavities and lift forces that resulted in lateral migration from straight-line trajectories. We also showed that surface roughness and impact orientation determined cavity depths and produced a scaling argument relating cavity depths κ to the coated-diameter coefficient α . Accordingly, $\kappa \sim (\alpha We)^{1/2}$. Hydrodynamic drag and lift forces were modeled with $\alpha = 0.33$, $\beta = 90^\circ$ yielding the greatest lateral migration $C_{Fx} \approx 0.50$, and $\alpha = 0.50$, $\beta = 90^\circ$ yielding the greatest drag $C_{Fy} \approx 0.21$ when compared to all entry scenarios on test.

In Chapter 5, we moved away from the water entry of spheres to focus on drop impacts on water striders. Striders are shown to survive impact forces the equivalent of 36 times their body weight during raindrop collisions. However, compression tests reveal the insect's ability to survive larger loads up to 1.5×10^5 dynes. During Worthington jet formation, some striders opportunistically jump from the fluid to escape the splash. Water striders left attached to the reclining Worthington jet were again pulled beneath the free surface and were either submerged or ejected based on their location relative to the secondary cavity.

It is my hope that the compendium of investigations and findings in this body of work bestow perspicuity to a number of fundamental fluid mechanics problems related to the coupled-dynamics of interfacial properties and the water entry of spherical projectiles, to date left largely unexplored by fluid dynamicists. In this thesis, we have applied modern technology, specifically high-speed videography and classical fluid mechanics towards understanding novel approaches for tuning splashes.

APPENDIX A: SUPPLEMENTARY MATERIAL

A.1 JET AMPLIFICATION AND CAVITY FORMATION INDUCED BY PENETRABLE FABRICS IN HYDROPHILIC SPHERE ENTRY

A.1.1 Jet Height Control by Layered Fabric

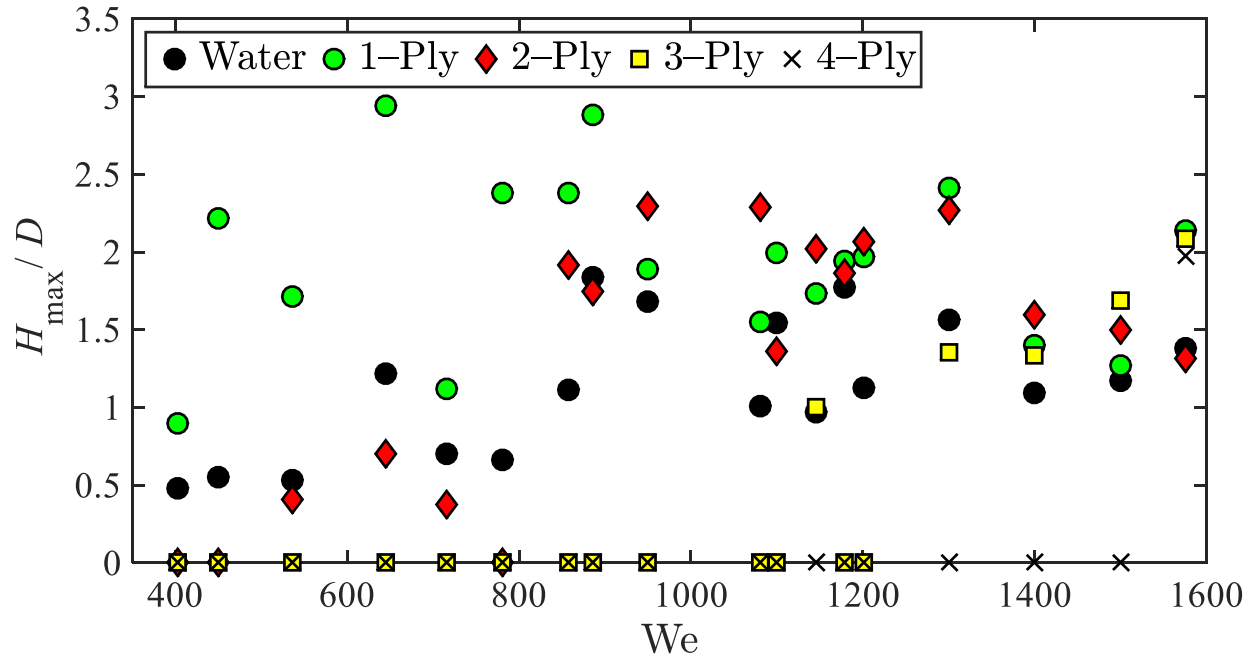


Figure A.1: Non-dimensional splash jet height H_{\max}/D versus Weber number We . Splash heights non-dimensionalized in terms of the sphere diameter, D . The number preceding 'ply' denotes layers of fabric. The presence of fabric creates greater jet heights for We sufficient to penetrate the fabric plies.

We measure splash heights for hydrophilic spheres impacting clean water and compare splash outcomes when a thin penetrable fabric is placed atop the fluid surface. We include a non-dimensionalized representation of splash height (Figure A.1) across the range of Weber numbers $We = 400 - 1580$ tested in our study and observe similar trends to the dimensional figure presented in the main text. We observe amplification by the inclusion of a single layer of fabric across all values of We . Splashes are amplified by a double layer of fabric for $We > 800$. Spheres are

unable to penetrate three and four layers of paper for $We < 1100$ and $We < 1500$ respectively.

A.1.2 Puncture Remains Constant

We include a supplementary figure to support the assertion that cavity properties are only a strong function of sphere size for the range of $We = 400 - 1580$ tested. Across the range of experimental We , we find that dimensions of the quasi-static [26] cavities created by a sphere of fixed $D = 2.20$ cm striking a single layer of fabric orthogonally show little variation. We likewise measure minimal variation in the non-dimensional areas of puncture $\alpha^* = \alpha/D^2$ as We increases (Figure A.2). We conclude that fabric tear is independent of impact velocity and is largely dependent on the diameter of the impactor (Movie A3).

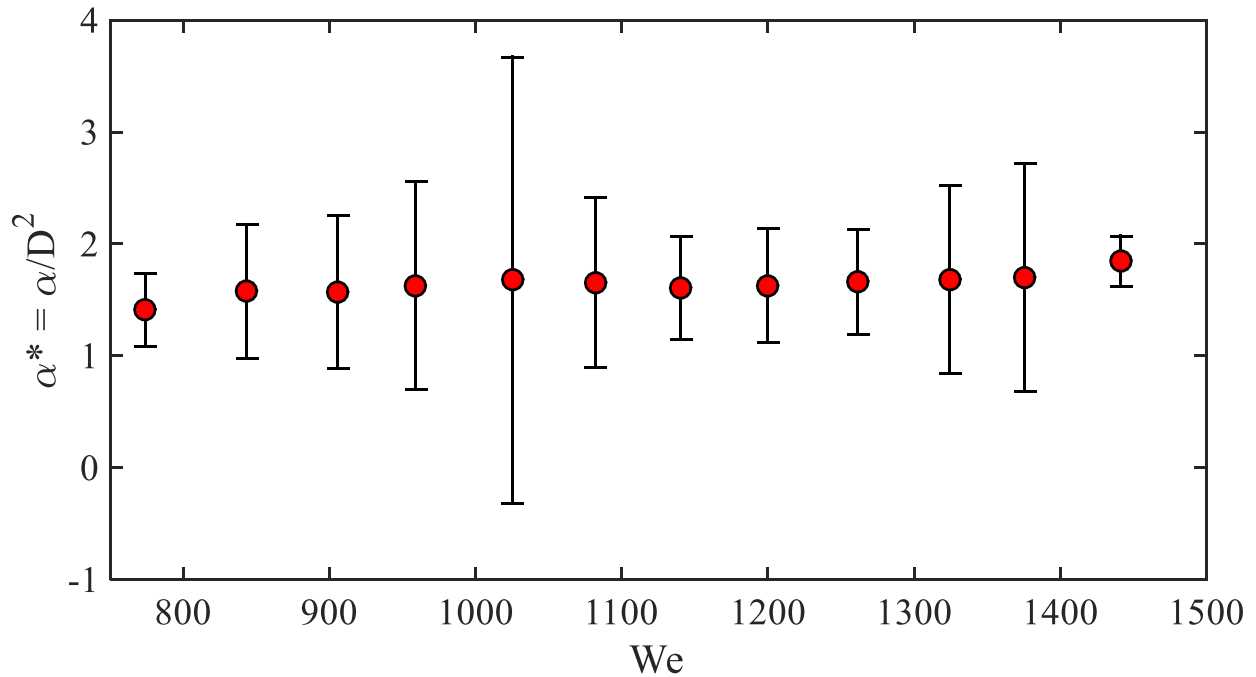


Figure A.2: The relation between Weber number and the area of the puncture α . Area non-dimensionalized in terms of the sphere diameter, $D = 2.20$ cm.

A.1.3 Fabric Increases Form Drag

The inclusion of fabric increases drag on spheres and influences the form drag diameter D_d during water entry [24, 25]. We use smoothed position data with the force balance equation from the main text and set $D_d = D$ to numerically obtain instantaneous values of C_D . We compute the mean values of C_D for impacts on 0-, 1-, 2-, 3- and 4-plyes and get 0.14, 0.17, 0.26, 0.40, and 1.15 respectively and solve for D_d , producing curves (Figure A.3) which show variation with instantaneous Re .

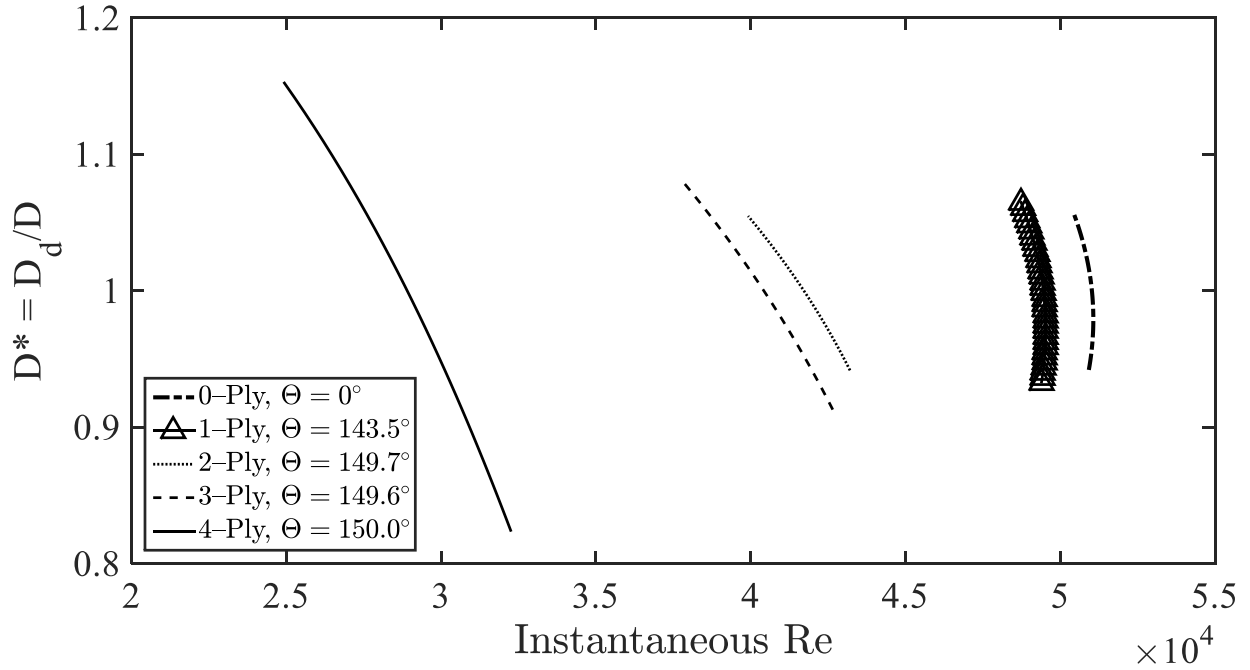


Figure A.3: Relation between the non-dimensionalized form drag diameter $D^* = D_d/D$ and the instantaneous Reynolds number Re . Form drag diameter D_d is non-dimensionalized in terms of the sphere diameter, $D = 2.54$ cm.

A.1.4 *Supplementary Movie Captions*

Supplementary movies can be accessed [here](#).

Movie A1: Hydrophilic sphere impact on an unaltered surface for $We = 1580$. Slowed 33X.

Movie A2: Hydrophilic sphere impact on a surface with a single layer of non-woven fabric for $We = 1580$. Slowed 33X.

Movie A3: Video-sequence of sphere impact from topical view showing the funneling of the Worthington jet through the puncture made by the passing sphere. Slowed 33X.

Movie A4: Hydrophilic sphere impact on a surface with a single layer of non-woven fabric for $We = 840$ showing air-entrainment. Slowed 33X.

Movie A5: Hydrophilic sphere impact on a surface with a single layer of paper towel for $We = 4445$. Slowed 33X.

Movie A6: Hydrophilic sphere impact through a pre-punctured layer of non-woven fabric for $We = 1580$, where the circular puncture has a diameter larger than the sphere ($3D/2$). Slowed 33X.

Movie A7: Hydrophilic sphere impact through a pre-punctured layer of non-woven fabric for $We = 1580$, where the circular puncture has a diameter small than the sphere ($D/2$). Slowed 33X.

A.2 MAKING A SPLASH WITH FABRICS IN HYDROPHILIC SPHERE ENTRY

A.2.1 Material Property Measurements

We include a supplementary figure to compare variation in fabric elasticity and strength when dry and wet. The ultimate failure stress σ_f of the material is considered as opposed to elastic modulus E , given our focus on fabric puncturability rather than fabric stretching [85, 86, 87, 88, 89, 90, 91, 92, 93, 94, 95, 96].

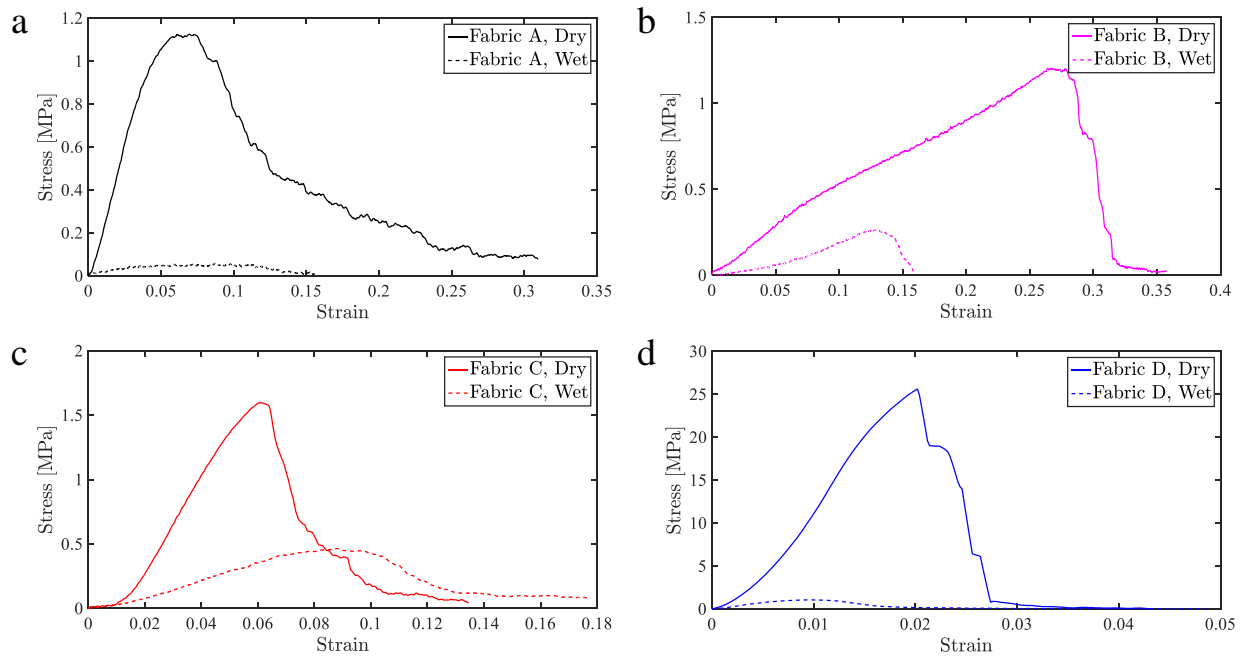


Figure A.4: Stress-strain curves showing tensile strength of fabric sheets tested, in dry and wet states. Fabrics tested are (a) Georgia Pacific Compact Coreless 2-Ply Toilet Paper, Fabric A; (b) Kleenex Trusted Care Facial 2-Ply Tissue, Fabric B; (c) Georgia Pacific Sparkle Professional Series 2-Ply Perforated Roll Paper Towel, Fabric C; and (d) Darice Assorted Colors Tissue Paper, Fabric D.

A.2.2 Greater Puncture Resistance Promote Higher Worthington Jets

The failure stress σ_f of fabric sheets resting atop a liquid bath [17, 18] influences the spheres' ability to penetrate the fluid surface during free-fall. Wetness alters stress-strain behaviour of fabrics and reduces impact force required for puncture as seen in Figure A.4. The uniqueness of fiber composition for tested fabrics is supported by the values of wet area densities ρ''_{wet} tabulated in the main manuscript. Fabrics A, B and C absorb fluid through capillary motion [118], increasing mass of rectangular sheets placed atop the free surface. In contrast, dry and wet area densities of Fabric D remain constant due to the non-wicking nature of fibers. For increasing ρ''_{wet} and $\sigma_{f,\text{wet}}$, splash height H_{max} is proportional to fabric cavity depth κ_f as seen by the fitted curves in Figure A.5. We may write, $H_{\text{max}} \sim \kappa_f^\alpha$. However, splash heights H_{max} arising from hydrophilic sphere impacts onto Fabric A show stronger correlation to the growth of trailing cavities κ_t (Figure A.5a) with a linear and exponent fit correlation value of $R^2 = 0.89$. Accordingly, $H_{\text{max}} \sim \kappa_t^\alpha$.

A.2.3 Smoothing Sphere Kinematics

A.2.3.1 Data Acquisition

In the present study, we acquire $N = 86$ frames at 2000 fps with a Photron Mini AX-100 high-speed camera to capture the water entry of hydrophilic steel spheres. Given the veiling of spheres with fabrics at impact, protocols previously established in Watson *et al.* (2018) [17] are employed for data acquisition and numerical differentiation. As such, Tracker, an open source image processing tool is used to track the sphere's center of mass and displacement as shown in Figure A.6a. While we note the existence of robust image cross-correlation procedures yielding sub-pixel accuracy in position track data [97], such techniques are more suited for experimental trials where viewing of the tracked bodies are not obscured.

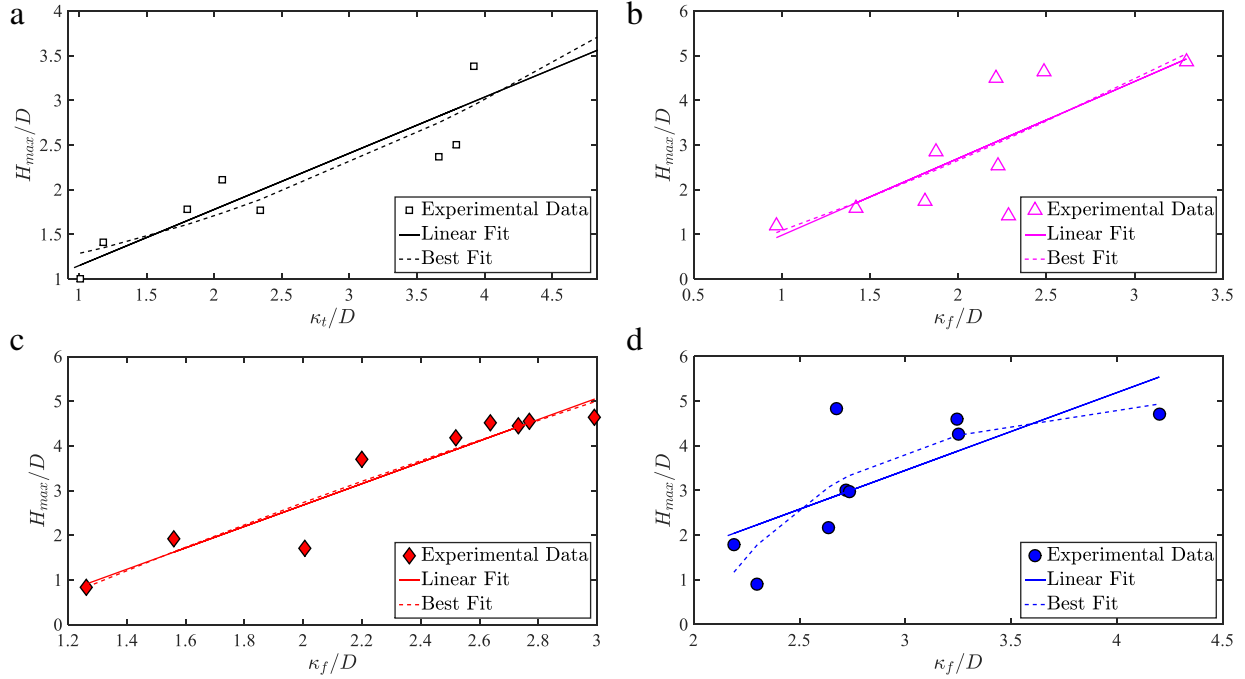


Figure A.5: Non-dimensionalized Worthington jet height H_{\max}/D versus non-dimensionalized cavity depth κ/D for hydrophilic sphere impacts onto (a) Fabric A, (b) Fabric B, (c) Fabric C, and (d) Fabric D. Individual correlation values are given in Table 3.1 alongside best fit exponents according to $H_{\max} \sim \kappa_f^\alpha$. Variables are non-dimensionalized in terms of the sphere diameter D .

A.2.3.2 Evaluating Derivatives

Position track data is initialized ($t = 0$ s) when spheres strike the fluid surface and terminated just before impact with the floor of the liquid pool. Smoothed, normalized, non-dimensionalized displacement curves y/D and experimental data are shown in Figure A.6a. We use a 2nd degree¹ Savitzky-Golay [84] filter (the ‘smooth’ function in MATLAB) and various smoothing spans² in the range $S = 0.1 - 1.0$ to determine the most suitable filter parameter which maintains the

¹Second order polynomial.

²Number of data points for calculating the smoothed value, specified as an integer or as a scalar value in the range (0,1) denoting a fraction of the total number of data points

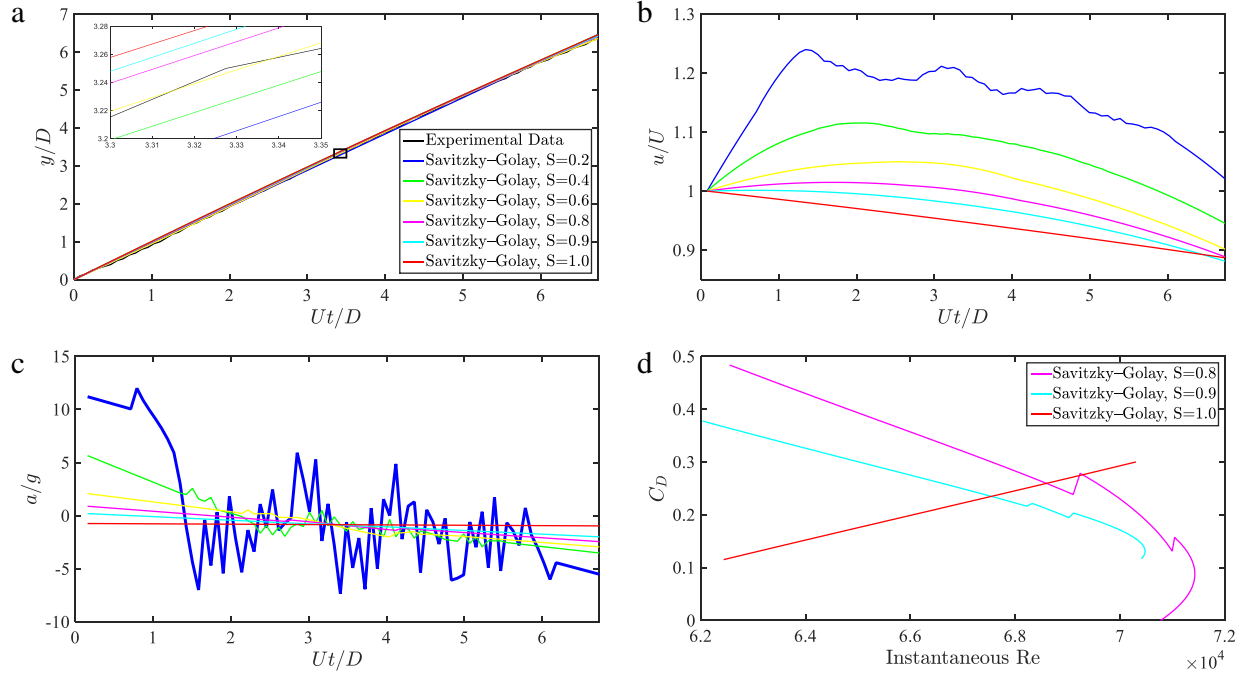


Figure A.6: Non-dimensionalized temporal tracks of (a) vertical position $y(t)/D$, (b) instantaneous velocity $u(t)/U$, and (c) instantaneous acceleration $a(t)/g$ for a hydrophilic sphere traversing an aqueous pool after impacting the unmodified free surface. Sphere trajectory is non-dimensionalized in terms of the impact velocity $U = 3.13$ m/s, sphere diameter $D = 2.0$ cm and acceleration due to gravity $g = 9.81$ m/s. We apply different smoothing spans in the range $S = 0.1 - 1.0$ to determine the most suitable filter parameter which maintains the physical integrity of experimental data. (d) The relation between hydrodynamic drag coefficient C_D and instantaneous Reynolds number Re . We apply different smoothing spans in the range $S = 0.8 - 1.0$ to determine the most suitable filter parameter which maintains the physical integrity of experimental data.

physical integrity of experimental data. Instantaneous velocity curves $u(t)$ are then evaluated by numerically differentiating position track data [17]. Results are again smoothed and normalized such that $u(0) = U$, where $U = (2 \cdot g \cdot h)^{1/2}$ is the impact velocity of the sphere, $g = 9.81$ m/s² is the acceleration due to gravity, and h is the drop height. For increasing S , non-dimensionalized sphere trajectories become smoother and steeper as shown in Figure A.6b. In the case of the experimental data on test, the minimum span required for acquisition of velocity curves in-line with sphere kinematics is $S = 1.0$. Lesser spans, for example, produce $u/U > 1$. This can be

adjudged visually in Figure A.6b. We then numerically differentiate velocity track data to obtain instantaneous acceleration curves as shown in Figure A.6c. A span $S = 1.0$ is the only span which provides a negative acceleration for the entire impact sequence. Positive accelerations mandate the sphere speeds up after impact, which does not match observation. These results are used in conjunction with the derived drag model for the calculation of drag coefficients C_D in Figure A.6d.

With a smoothing span decided at $S = 1.0$, we now evaluate various polynomials available for smoothing. In Figure A.7 we show the effect of 1–3 degree polynomials on the smoothed data. Note that the data is not fitted to a n^{th} degree polynomial. The quadratic option is the only smoothing scheme which maintains the physical integrity of the data, namely $u/U < 1$ and $a/g < 0$, as shown in Figure A.7b–c.

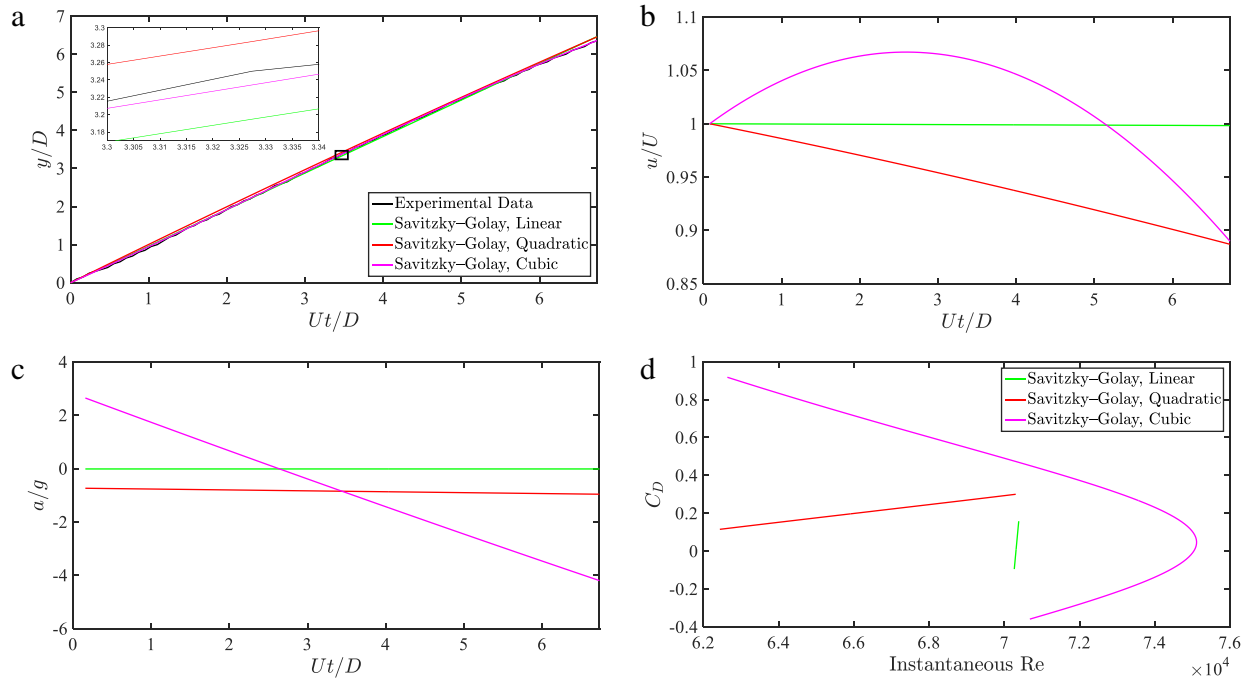


Figure A.7: Non-dimensionalized temporal tracks of (a) vertical position $y(t)/D$, (b) instantaneous velocity $u(t)/U$, and (c) instantaneous acceleration $a(t)/g$ for a hydrophilic sphere traversing an aqueous pool after impacting the unmodified free surface. Sphere trajectory is non-dimensionalized in terms of the impact velocity $U = 3.13$ m/s, sphere diameter $D = 2.0$ cm and acceleration due to gravity $g = 9.81$ m/s. We apply different degree polynomials determine the most suitable filter parameter which maintains the physical integrity of experimental data, while fixing the span $S = 1.0$. (d) The relation between hydrodynamic drag coefficient C_D and instantaneous Reynolds number Re . We apply different degree polynomials determine the most suitable filter parameter which maintains the physical integrity of experimental data.

A.2.4 *Supplementary Movie Captions*

Supplementary movies can be accessed [here](#).

Movie B1: Hydrophilic steel sphere impact on an unaltered aqueous pool for $We = 2688$. Slowed 33X.

Movie B2: Hydrophilic steel sphere impact on an aqueous pool layered with a single sheet of Fabric A for $We = 2688$. Slowed 33X.

Movie B3: Hydrophilic steel sphere impact on an aqueous pool layered with a single sheet of Fabric B for $We = 2688$. Slowed 33X.

Movie B4: Hydrophilic steel sphere impact on an aqueous pool layered with a single sheet of Fabric C for $We = 2688$. Slowed 33X.

Movie B5: Hydrophilic steel sphere impact on an aqueous pool layered with a single sheet of Fabric D for $We = 2688$. Slowed 33X.

Movie B6: Hydrophobic steel sphere impact on an unaltered aqueous pool for $We = 2688$. Slowed 66X.

Movie B7: Hydrophilic steel sphere impact on an aqueous pool layered with a single square (left) and rounded (right) sheet of Fabric B for $We = 2688$. Slowed 33X.

Movie B8: Hydrophilic steel sphere impact on an aqueous pool layered with a thin layer of ice for $We = 1615$. Slowed 66X.

Movie B9: Hydrophilic Delrin sphere impact on the edge of Fabric B during water entry into an aqueous pool for $We = 1076$. Slowed 33X.

A.3 WATER ENTRY DYNAMICS OF SPHERES WITH HETEROGENEOUS WETTING PROPERTIES

A.3.1 Surface Roughness and Orientation Determine Cavity Depths

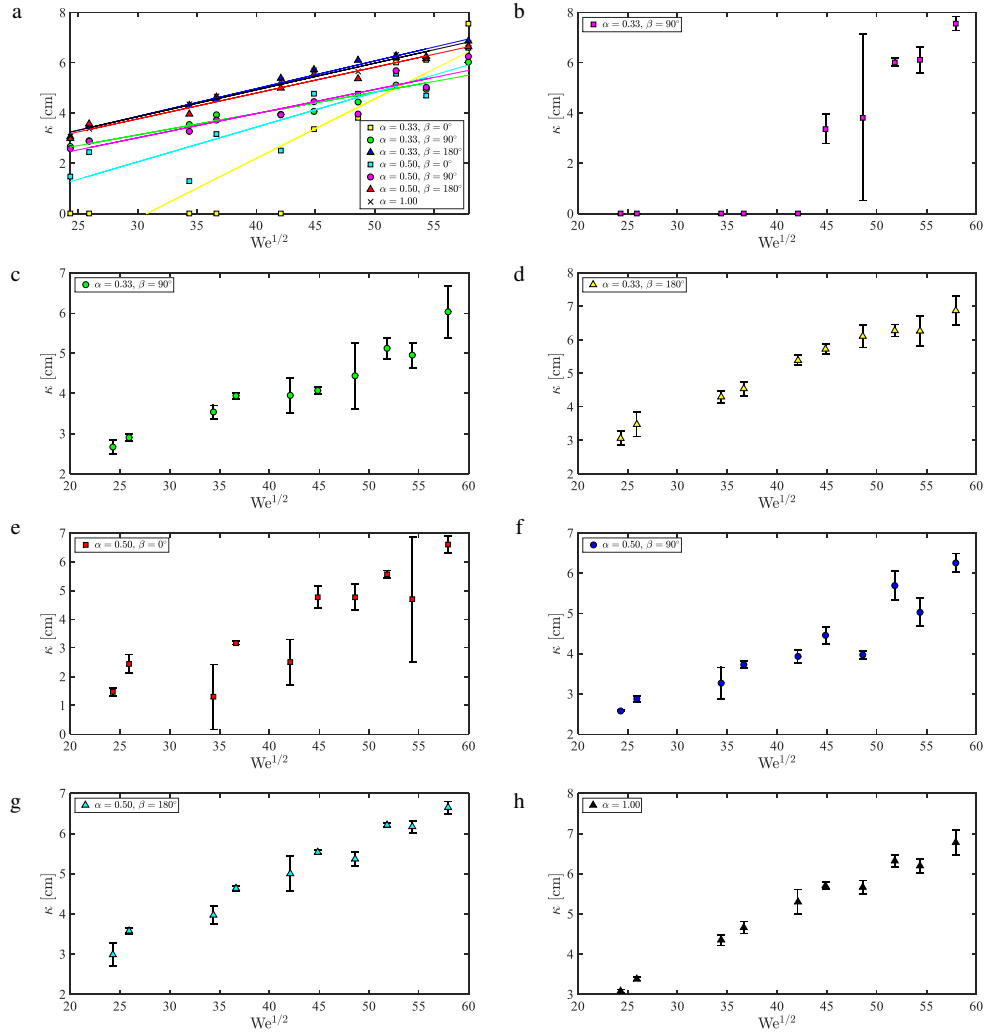


Figure A.8: (a) Measurements and linear fits of non-dimensionalized cavity depths κ/D versus Weber number We for the range of coating α and impact orientations β tested. Individual linear fit R^2 values are tabulated in the manuscript. Disaggregated plots with error bars are shown in (b)–(h). Cavities arising from the water entry of hemispherically-coated spheres may be described by $\kappa \sim (\alpha We)^{1/2}$ for low impact velocities, and $\kappa \sim We^{1/2}$ for increasing entry speeds. Variables are non-dimensionalized in terms of sphere diameter D .

A.3.2 Submerged Impactors Experience Lift and Drag

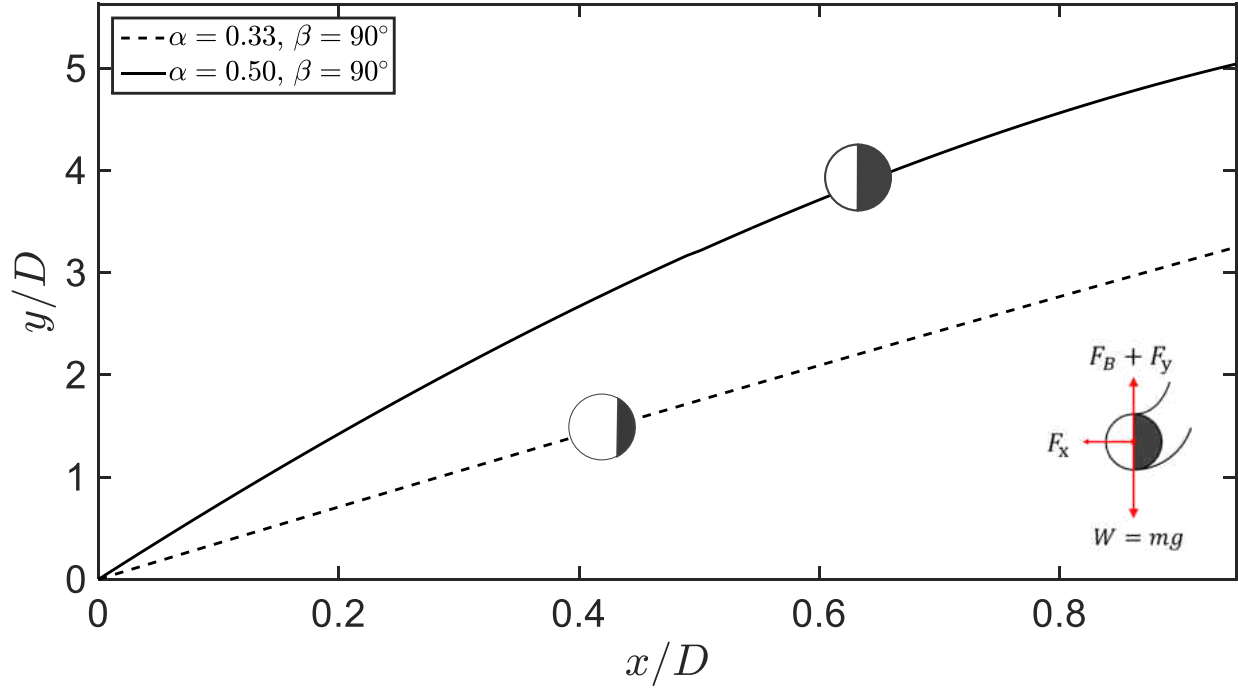


Figure A.9: Non-dimensionalized trajectories of heterogeneous spheres $\alpha = 0.33$, and $\alpha = 0.50$ with the line of demarcation perpendicular to the free surface at water entry. Trajectories are non-dimensionalized in terms of the sphere diameter, $D = 2.54$ cm, and have impact velocity $U = 2.4$ m/s.

A.3.3 *Supplementary Movie Captions*

Supplementary movies can be accessed [here](#).

Movie C1: Fully hydrophobic sphere impacting the free surface of an aqueous pool for $We = 2014$. Slowed 33X.

Movie C2: Heterogeneous sphere with upward-facing hydrophobic surface $\alpha = 0.50$, $\beta = 0^\circ$ impacting the free surface of an aqueous pool for $We = 2014$. Slowed 33X.

Movie C3: Heterogeneous sphere with line of demarcation perpendicular to gravity $\alpha = 0.50$, $\beta = 90^\circ$ impacting the free surface of an aqueous pool for $We = 2014$. Slowed 33X.

Movie C4: Heterogeneous sphere with upward-facing hydrophilic surface $\alpha = 0.50$, $\beta = 180^\circ$ impacting the free surface of an aqueous pool for $We = 2014$. Slowed 33X.

Movie C5: Fully hydrophilic sphere impacting the free surface of an aqueous pool for $We = 2014$. Slowed 33X.

Movie C6: Fully hydrophilic sphere impacting the edge of a fabric sheet placed atop the free surface of an aqueous pool for $We = 592$. Slowed 33X.

A.4 LIFE ON STORMY SEAS: WATER STRIDERS ARE IMPERVIOUS TO RAINDROP IMPACTS

A.4.1 Drop Impact Area

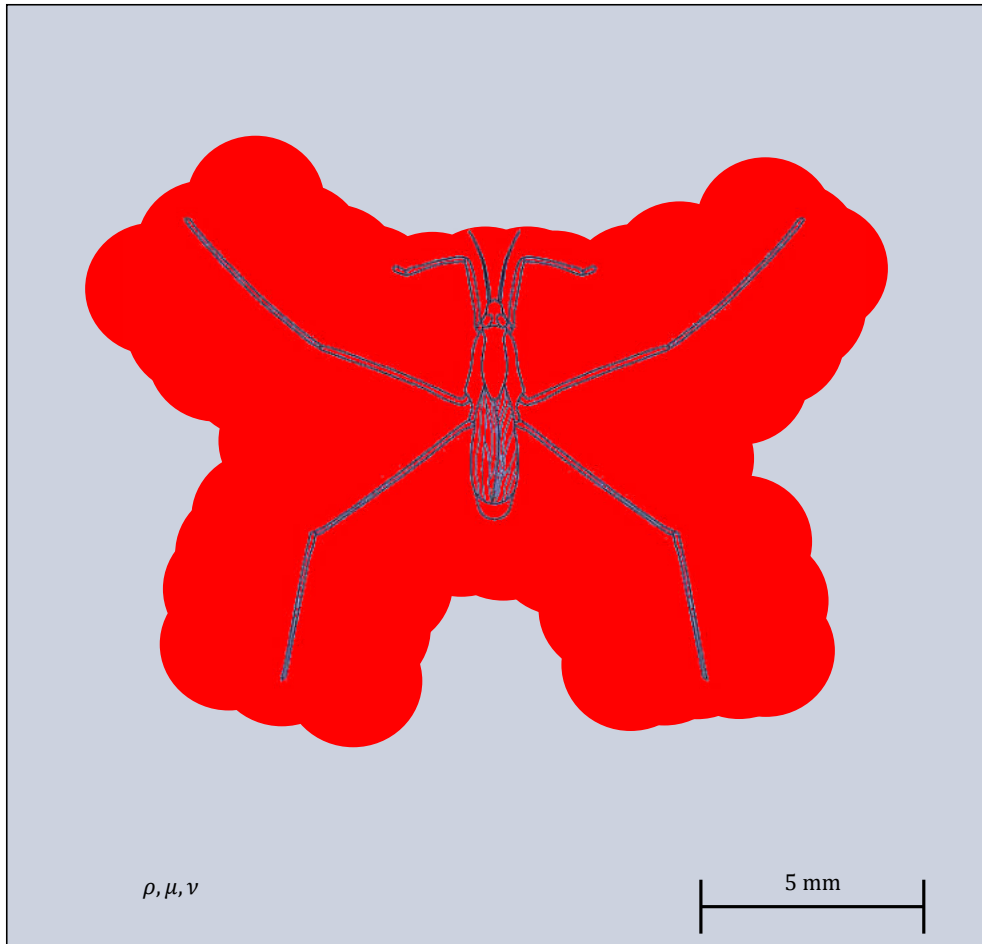


Figure A.10: Impact area of an adult water strider. The strider's exoskeleton including the legs has impact area in the range $A_s = 34 - 165 \text{ mm}^2$. Impact area varies depending on drop size D , and is determined by first tracing the body of the strider with the desired drop. The area of the drop trace is then obtained graphically using ImageJ. Raindrop collisions within the impact area are considered as direct impacts. The water strider's legs account for 80% of the impact area, while the torso only accounts for 20%. During the heaviest rainfall [4, 5] with drops of mass $m = 16 \text{ mg}$, falling with an intensity [6] $I \approx 50 \text{ mm/h}$, a resting water strider will experience impacts on average every $\Delta t = m / (I \cdot \rho \cdot A_s) \approx 7 \text{ s}$, considering the entire impact area of the insect, and direct torsal impacts every $\Delta t \approx 34 \text{ s}$.

A.4.2 *Supplementary Movie Captions*

Supplementary movies can be accessed [here](#).

Movie D1: Collapse of the primary Worthington jet creates secondary cavities and jets that in–turn submerge water striders. $We \approx 2150$. Slowed 133X.

Movie D2: Drop impact onto the free surface of an aqueous pool for $We \approx 2150$. Slowed 133X.

Movie D3: Survivability of water strider supplemented by the formation of a plastron during subsurface transport. $We \approx 2150$. Slowed 133X.

Movie D4: Collapse of the primary Worthington jet creates secondary cavities and jets that in–turn eject water striders. $We \approx 2150$. Slowed 133X.

Movie D5: Drops missing water striders create surface waves and satellite droplets inciting water striders to jump away from the oncoming wave. $We \approx 2150$. Slowed 133X.

Movie D6: Water strider actively separates from Worthington jets by jumping. $We \approx 2150$. Slowed 133X.

Movie D7: Water striders exposed to higher–frequency drop impacts to test survivability. $We \approx 2150$. Slowed 133X.

Movie D8: Water strider applies a series of power stroke during subsurface locomotion. Slowed 133X.

APPENDIX B: SCHOLARLY ACHIEVEMENTS

B.1 Journal Articles

Watson, D. A., Thornton, R., M., Khan, A. H., and Dickerson, A. K. "Life on stormy seas: water striders are impervious to raindrop impacts". In Preparation.

Watson, D. A., Bom, Weinberg, P. M., M. J., Souchik, J. C., and Dickerson, A. K. "Water entry dynamics of spheres with heterogeneous wetting properties". Under Review.

Watson, D. A., Souchik, J. C., Weinberg, P. M., Bom, M. J., and Dickerson, A. K., 2020 "Making a splash with fabrics in hydrophilic sphere entry". *Journal of Fluids and Structures*. Volume 94, 102907, doi:10.1016/j.jfluidstructs.2020.102907. March 2020.

Watson, D. A., Stephen, J. L., and Dickerson, A. K., 2019 "Impacts of free-falling spheres onto a deep liquid pool with altered fluid and impactor surface conditions". *Journal of Visualized Experiments*, Issue 144, e59300, doi:10.3791/59300, February 2019.

Watson, D. A., Stephen, J. L., and Dickerson, A. K., 2018 "Jet amplification and cavity formation induced by penetrable fabrics in hydrophilic sphere entry". *Physics of Fluids*, Volume 30, Issue 8, doi:10.1063/1.5036655, August 2018.

Watson, D. A., Binnie, Y., Duncan, K. L., Dorville, J. F., 2017 "Photurgen: The open source software for the analysis and design of hybrid solar wind energy systems in the Caribbean region: An introduction to its development policy". *Energy Reports*, Volume 3, doi:10.1016/j.egy.2017.03.001, November 2017.

B.2 Conference Papers

Alam, E., Smith, N., Watson, D. A., Hassan, T., and Neupane, K., 2019 "Early screening of DDH using SVM classification". *Proceedings of the IEEE SoutheastCon 2019*, April 2019. Alabama, United States of America.

B.3 Conference Presentations

Watson, D. A., Bom, M. J., Souchik, J. C., and Dickerson, A. K., 2019 "Underwater acrobatics of partially-coated spheres". Oral Presentation. American Physics Society: Division of Fluid Dynamics. November 2019. Seattle, Washington, United States of America.

Watson, D. A., Souchik, J. C., Bom, M. J., and Dickerson, A. K., 2019 "Water entry of hydrophilic spheres through fabric-fluid interfaces". Poster Presentation. American Physics Society: Division of Fluid Dynamics. November 2019. Seattle, Washington, United States of America.

Watson, D. A., Khan, H. A., DiAmco, R. C., and Dickerson, A. K., 2019 "On the survival of water striders during raindrop impacts". Oral Presentation. Society for Integrative and Comparative Biology. January 2019. Tampa, Florida, United States of America.

Watson, D. A., Stephen, J. L., and Dickerson, A. K., 2019 "On the reduction of splash-back". Oral Presentation. American Physics Society: Division of Fluid Dynamics. November 2017. Denver, Colorado, United States of America.

B.4 Research Symposium

Watson, D. A., DiAmco, R. C., Khan, H. A., and Dickerson, A. K., 2019 "Survivability of water striders during raindrop collisions". Annual Graduate Research Forum. April 2019. University of Central Florida, United States of America.

Bom, M. J., Souchik, J. C., Watson, D. A., and Dickerson, A. K., 2019 "Vertical impacts of chemically heterogeneous spheres on a deep liquid pool". Showcase of Undergraduate Research Excellence. April 2019. University of Central Florida, United States of America.

Souchik, J. C., Bom, M. J., Watson, D. A., and Dickerson, A. K., 2019 "Vertical impacts of free-falling hydrophilic spheres onto stratified fluid surfaces". Showcase of Undergraduate Research Excellence. April 2019. University of Central Florida, United States of America.

Stephen, J. L., Watson, D. A., and Dickerson, A. K., 2018 "Splash regulation of vertical impacts on a liquid surface by alteration of surface conditions". Showcase of Undergraduate Research Excellence. April 2018. University of Central Florida, United States of America.

Watson, D. A., Binnie, Y., Duncan, K. L., Dorville, J. F., 2017 "Photurgen: The open source software for the analysis and design of hybrid solar wind energy systems in the Caribbean region". Software. Presented at the Annual Research Day Symposium, February 1 – 3, 2017, University of the West Indies, Kingston, Jamaica.

Watson, D. A., Dorville, J. F., and Duncan, K. L., 2015 "First experimentation of Photurgen: An optimization and management software for hybrid renewable energy systems". Poster. Presented at the Faculty of Science and Technology's 10th Biennial Conference, June 8 – 9, 2015, University of the West Indies, Kingston, Jamaica.

B.5 Graduate Theses

Watson, D. A., 2020 "Interfacial properties modulate water entry dynamics for spherical projectiles". Doctor of Philosophy. University of Central Florida, Florida, United States of America.

Watson, D. A., 2016 "Realization of an open source software of computation for the optimization of hybrid renewable energy systems: application in the Caribbean region". Master of Philosophy. University of the West Indies, Kingston, Jamaica.

APPENDIX C: VITA

C.1 Academic Training

Daren A. Watson was born on June 26, 1991, and spent most of his youthful life between St. Catherine, and Kingston, Jamaica. He graduated from the Campion College High School in 2010 with an Associate Degree in Natural Sciences, after which he enrolled at the University of the West Indies, Mona campus where he completed his B.S. in Environmental Physics and Mathematics with First Class Honors in 2013. Daren finished in the top 1% of his class and received a nomination for valedictorian. He then completed an M.Phil. in Physics specializing in Alternative Energy at the University of the West Indies in 2016. After being awarded the prestigious Fulbright Graduate Scholarship in 2017, Daren enrolled at the University of Central Florida, Orlando, Florida, and satisfied the requirements for his M.S. in Mechanical Engineering in 2019. On October 9, 2020, he successfully defended his Ph.D. in Mechanical Engineering and began duties as a Postdoctoral Research Associate in the Fluids and Structures Laboratory at the University of Central Florida.

C.2 Water Entry

Why Water Entry? Towards the end of my M.Phil. in Physics, I began to explore new opportunities for doctoral studies. In 2017, I was awarded the Fulbright Graduate Scholarship and placement at five universities across the United States of America, including at the University of Central Florida (UCF), to pursue a Ph.D. in Mechanical Engineering. While UCF was my preferential choice based on the analogous environmental conditions of Florida and Jamaica, and topics surrounding energy-related research [119, 120, 121] an allure, my initial conversation with Dr. Dickerson about finding ways to reduce splash-back superseded all other considerations. I did not realize at that moment the extent to which I would build an appreciation for, and a relationship with spherical projectiles impacting deep liquid pools, seemingly a most far-fetched fascination relative

to what many consider the interests of mechanical engineers. Armed with a high-speed camera, an aquarium and an array of spheres, we took our first venture into the complex, but extremely beautiful field of water entry. Three years and four articles later, much is still not yet known, so we film on to new discoveries, and take solace in the breathtaking images captured along the way.



LIST OF REFERENCES

- [1] Duez, C., Ybert, C., Clanet, C. & Bocquet, L., 2007 Making a splash with water repellency. *Nature Physics* **3**, 180 – 183. ISSN 17452473.
- [2] Comtet, J., Keshavarz, B. & Bush, J. W., 2016 Drop impact and capture on a thin flexible fiber. *Soft Matter* **12**, 149–156.
- [3] Mahadik, G. A., Hernandez-Sanchez, J. F., Arunachalam, S., Gallo Jr., A., Cheng, L., Farinha, A. S., Thoroddsen, S. T., Mishra, H. & Duarte, C. M., 2020 Superhydrophobicity and size reduction enabled halobates (insecta: Heteroptera, gerridae) to colonize the open ocean. *Scientific Reports* **10**, 7785–. ISSN 2045-2322.
- [4] Laws, J. O., 1943 The relation of raindrop-size to intensity. *Eos, Transactions American Geophysical Union* **24**, 452–460. (doi:10.1029/TR024i002p00452).
- [5] Villermaux, E. & Bossa, B., 2009 Single-drop fragmentation determines size distribution of raindrops. *Nature Physics* **5**, 697–702. ISSN 1745-2481.
- [6] Dickerson, A. K., Shankles, P. G., Madhavan, N. M. & Hu, D. L., 2012 Mosquitoes survive raindrop collisions by virtue of their low mass. *Proceedings of the National Academy of Sciences* **109**, 9822–9827.
- [7] Worthington, A. M. & Cole, R. S., 1897 Impact with a liquid surface studied by the aid of instantaneous photography. *Philosophical Transactions of the Royal Society of London. Series A, Containing Papers of a Mathematical or Physical Character* p. 137. ISSN 02643952.
- [8] Worthington, A. M. & Cole, R. S., 1900 Impact with a liquid surface studied by the aid of instantaneous photography. paper ii. *Philosophical Transactions of the Royal Society*

of London. Series A, Containing Papers of a Mathematical or Physical Character p. 175.
ISSN 02643952.

- [9] Worthington, A. M., 1908 A study of splashes .
- [10] Hu, D. L., Chan, B. & Bush, J. W. M., 2003 The hydrodynamics of water strider locomotion. *Nature* **424**, 663 – 666. ISSN 00280836.
- [11] Bush, J. W. & Hu, D. L., 2006 Walking on water: Bioloocomotion at the interface. *Annual Review of Fluid Mechanics* **38**, 339–369.
- [12] Ortega-Jimenez, V. M., von Rabenau, L. & Dudley, R., 2017 Escape jumping by three age classes of water striders from smooth, wavy and bubbling water surfaces. *Journal of Experimental Biology* **220**, 2809–2815. ISSN 0022-0949.
- [13] Zhao, M.-H., Chen, X.-P. & Wang, Q., 2014 Wetting failure of hydrophilic surfaces promoted by surface roughness. *Scientific reports* **4**, 5376.
- [14] Vakarelski, I. U., Jetly, A. & Thoroddsen, S. T., 2019 Stable-streamlined cavities following the impact of non-superhydrophobic spheres on water. *Soft matter* **15**, 6278–6287.
- [15] May, A., 1951 Effect of surface condition of a sphere on its water-entry cavity. *Journal of Applied Physics* **22**, 1219 – 1222. ISSN 00218979.
- [16] Shin, J. & McMahon, T. A., 1990 The tuning of a splash. *Physics of Fluids A: Fluid Dynamics* **2**, 1312–1317.
- [17] Watson, D. A., Stephen, J. L. & Dickerson, A. K., 2018 Jet amplification and cavity formation induced by penetrable fabrics in hydrophilic sphere entry. *Physics of Fluids* **30**, 082109.

- [18] Watson, D. A., Stephen, J. L. & Dickerson, A. K., 2019 Impacts of free-falling spheres onto a deep liquid pool with altered fluid and impactor surface conditions. *Journal of Visualized Experiments* **144**, e59300.
- [19] Watson, D. A., Souchik, C. J., Weinberg, M. P., Bom, J. M. & Dickerson, A. K., 2020 Making a splash with fabrics in hydrophilic sphere entry. *Journal of Fluids and Structures* **94**, 102907. ISSN 0889-9746.
- [20] Aristoff, J. M., Truscott, T. T., Techet, A. H. & Bush, J. W. M., 2008 The water entry cavity formed by low bond number impacts. *Physics of Fluids* **20**, 091111.
- [21] Aristoff, J. & Bush, J., 2009 Water entry of small hydrophobic spheres. *Journal of Fluid Mechanics* **619**, 45 – 78. ISSN 00221120.
- [22] Truscott, T. & Techet, A., 2009 Water entry of spinning spheres. *Journal of Fluid Mechanics* **625**, 135 – 165. ISSN 00221120.
- [23] Truscott, T. T., 2009 *Cavity dynamics of water entry for spheres and ballistic projectiles*. Doctor of Philosophy, Massachusetts Institute of Technology.
- [24] Aristoff, J., Truscott, T., Techet, A. & Bush, J., 2010 The water entry of decelerating spheres. *Physics of Fluids* **22**. ISSN 10706631.
- [25] Truscott, T., Epps, B. & Techet, A., 2012. Unsteady forces on spheres during free-surface water entry. *Journal of Fluid Mechanics* **704**, 173 – 210. ISSN 00221120.
- [26] Truscott, T. T., Epps, B. P. & Belden, J., 2013 Water entry of projectiles. *Annual Review of Fluid Mechanics* **46**, 355 – 378. ISSN 00664189.
- [27] Kubota, Y. & Mochizuki, O., 2011 Influence of head shape of solid body plunging into water on splash formation. *Journal of Visualization* **14**, 111–119. ISSN 1875-8975.

- [28] Marston, J. O., Truscott, T. T., Speirs, N. B., Mansoor, M. M. & Thoroddsen, S. T., 2016 Crown sealing and buckling instability during water entry of spheres. *Journal of Fluid Mechanics* **794**, 506–529.
- [29] Shi, H., Itoh, M. & Takami, T., 2000 Optical observation of the supercavitation induced by high-speed water entry. *Journal of Fluids Engineering* **122**, 806 – 810. ISSN 00982202.
- [30] Thoroddsen, S. T., Etoh, T. G., Takehara, K. & Takano, Y., 2004 Impact jetting by a solid sphere. *Journal of Fluid Mechanics* **499**, 139–148.
- [31] Beczek, M., Ryzak, M., Sochan, A., Mazur, R., Polakowski, C. & Bieganski, A., 2017 The differences in crown formation during the splash on the thin water layers formed on the saturated soil surface and model surface. *PLOS ONE* **12**. ISSN 19326203.
- [32] Cheny, J. & Walters, K., 1996 Extravagant viscoelastic effects in the worthington jet experiment. *Journal of Non-Newtonian Fluid Mechanics* **67**, 125 – 135. ISSN 0377-0257. Papers Presented at the Workshop on 'Unresolved Experimental Dilemmas in the Dynamics of Complex Fluids'.
- [33] Ogawa, A., Utsuno, K., Mutou, M., Kouzen, S., Shimotake, Y. & Satou, Y., 2006 Morphological study of cavity and Worthington jet formations for Newtonian and non-Newtonian liquids. *Particulate Science & Technology* **24**, 181 – 225. ISSN 02726351.
- [34] Castillo-Orozco, E., Davanlou, A., K. Choudhury, P. & Kumar, R., 2015 Droplet impact on deep liquid pools: rayleigh jet to formation of secondary droplets. *Physical Review E* **92**.
- [35] Mansoor, M. M., Marston, J. O., Vakarelski, I. U. & Thoroddsen, S. T., 2014 Water entry without surface seal: extended cavity formation. *Journal of Fluid Mechanics* **743**, 295–326.
- [36] Techet, A. & Truscott, T., 2011 Water entry of spinning hydrophobic and hydrophilic spheres. *Journal of Fluids and Structures* p. 716. ISSN 0889-9746.

- [37] Gekle, S. & Gordillo, J. M., 2010 Generation and breakup of Worthington jets after cavity collapse. part 1. jet formation. *Journal of Fluid Mechanics* **663**, 293–330.
- [38] Zhao, S., Wei, C. & Cong, W., 2016 Numerical investigation of water entry of half hydrophilic and half hydrophobic spheres. *Mathematical Problems in Engineering* **2016**, 1–15.
- [39] Cai, Y. K., 1989 Phenomena of a liquid drop falling to a liquid surface. *Experiments in Fluids* **7**, 388–394. ISSN 1432-1114.
- [40] Gilbarg, D. & Anderson, R. A., 1948 Influence of atmospheric pressure on the phenomena accompanying the entry of spheres into water. *Journal of Applied Physics* **19**, 127 – 139. ISSN 00218979.
- [41] Cossali, G. E., Marengo, M., Coghe, A. & Zhdanov, S., 2004 The role of time in single drop splash on thin film. *Experiments in Fluids* **36**, 888–900. ISSN 1432-1114.
- [42] Li, D., Zhang, J., Zhang, M., Huang, B., Ma, X. & Wang, G., 2019 Experimental study on water entry of spheres with different surface wettability. *Ocean Engineering* **187**, 106123. ISSN 0029-8018. (doi:<https://doi.org/10.1016/j.oceaneng.2019.106123>).
- [43] Gekle, S., Gordillo, J. M., van der Meer, D. & Lohse, D., 2009 High-speed jet formation after solid object impact. *Physical review letters* **102**, 034502.
- [44] Gordillo, J. M. & Gekle, S., 2010 Generation and breakup of Worthington jets after cavity collapse. part 2. tip breakup of stretched jets. *Journal of fluid mechanics* **663**, 331–346.
- [45] Speirs, N. B., Mansoor, M. M., Belden, J. & Truscott, T. T., 2019 Water entry of spheres with various contact angles. *Journal of Fluid Mechanics* **862**.
- [46] Bodily, K. G., Carlson, S. J. & Truscott, T. T., 2014 The water entry of slender axisymmetric bodies. *Physics of Fluids* **26**, 072108. ISSN 1089-7666. (doi:10.1063/1.4890832).

- [47] Speirs, N. B., Pan, Z., Belden, J. & Truscott, T. T., 2018 The water entry of multi-droplet streams and jets. *Journal of Fluid Mechanics* **844**, 1084–1111.
- [48] Ueda, Y. & Iguchi, M., 2012 Water entry of stripe-coated hydrophobic circular cylinders. *Journal of visualization* **15**, 33–35.
- [49] Caponigro, M. A. & Eriksen, C. H., 1976 Surface film locomotion by the water strider, *Gerris remigis* say. *The American Midland Naturalist* **95**, 268–278. ISSN 00030031, 19384238.
- [50] Spence, J. R. & Anderson, N. M., 1994 Biology of water striders: Interactions between systematics and ecology. *Annual Review of Entomology* **39**, 101–128.
- [51] Kishi, M., Fujisaki, K. & Harada, T., 2006 How do water striders, *aquarius paludum*, react to brackish water simulated by nacl solutions? *Naturwissenschaften* **93**, 33–37. ISSN 1432-1904.
- [52] Andersen, N. M. & Polhemus, J., 1976 Water-striders (hemiptera: Gerridae, veliidae, etc.). *Marine insects*. Elsevier, Amsterdam pp. 187–224.
- [53] Koh, J.-S., Yang, E., Jung, G.-P., Jung, S.-P., Son, J. H., Lee, S.-I., Jablonski, P. G., Wood, R. J., Kim, H.-Y. & Cho, K.-J., 2015 Jumping on water: Surface tension–dominated jumping of water striders and robotic insects. *Science* **349**, 517–521. ISSN 0036-8075. (doi:10.1126/science.aab1637).
- [54] Feng, X.-Q., Gao, X., Wu, Z., Jiang, L. & Zheng, Q.-S., 2007 Superior water repellency of water strider legs with hierarchical structures: experiments and analysis. *Langmuir* **23**, 4892–4896.
- [55] Goodwyn, P. P., tong Wang, J., ji Wang, Z., hong Ji, A., dong Dai, Z. & Fujisaki, K., 2008 Water striders: The biomechanics of water locomotion and functional morphology of the

- hydrophobic surface (insecta: Hemiptera-heteroptera). *Journal of Bionic Engineering* **5**, 121 – 126. ISSN 1672-6529.
- [56] Zhou, Z.-G. & Liu, Z.-W., 2009 Fabrication of biomimetic water strider legs covered with setae. *Journal of Bionic Engineering* **6**, 1 – 6. ISSN 1672-6529.
- [57] Balmert, A., Bohn, H. F., Ditsche-Kuru, P. & Barthlott, W., 2011 Dry under water: Comparative morphology and functional aspects of air-retaining insect surfaces. *Journal of Morphology* **272**, 442–451.
- [58] Ngo, V. & McHenry, M. J., 2014 The hydrodynamics of swimming at intermediate reynolds numbers in the water boatman (corixidae). *Journal of Experimental Biology* **217**, 2740–2751. ISSN 0022-0949. (doi:10.1242/jeb.103895).
- [59] Wang, Q., Yao, X., Liu, H., Quéré, D. & Jiang, L., 2015 Self-removal of condensed water on the legs of water striders. *Proceedings of the National Academy of Sciences* **112**, 9247–9252. ISSN 0027-8424.
- [60] Andersen, N. M., 1977 Fine structure of the body hair layers and morphology of the spiracles of semiaquatic bugs (insects, hemiptera, gerromorpha) in relation to life on the water surface. *Videnskabelige meddelelser fra Dansk naturhistorisk forening i Kjøbenhavn* .
- [61] Kim, S., Wu, Z., Esmaili, E., Dombroskie, J. J. & Jung, S., 2020 How a raindrop gets shattered on biological surfaces. *Proceedings of the National Academy of Sciences* .
- [62] Buhler, O., 2007 Impulsive fluid forcing and water strider locomotion. *Journal of Fluid Mechanics* **573**, 211 – 236. ISSN 00221120.
- [63] Xu, L., Yao, X. & Zheng, Y., 2012 Direction-dependent adhesion of water strider's legs for water-walking. *Solid State Sciences* **14**, 1146 – 1151. ISSN 1293-2558.

- [64] Suter, R. B., 2013 Spider locomotion on the water surface: biomechanics and diversity. *The Journal of Arachnology* p. 93. ISSN 01618202.
- [65] Yin, W., Zheng, Y. L., Lu, H. Y., Zhang, X. J. & Tian, t., Y.1, 2016 Three-dimensional topographies of water surface dimples formed by superhydrophobic water strider legs. *Applied Physics Letters* **109**, 1 – 4. ISSN 00036951.
- [66] Yang, E., Son, J. H., Lee, S., Jablonski, P. G. & Kim, H.-Y., 2016 Water striders adjust leg movement speed to optimize takeoff velocity for their morphology. *Nature Communications* **7**, 13698.
- [67] Spilhaus, A. F., 1948 Drop size, intensity, and radar echo of rain. *Journal of Meteorology* **5**, 161–164.
- [68] Dickerson, A. K., Shankles, P. G. & Hu, D. L., 2014 Raindrops push and splash flying insects. *Physics of Fluids* **26**, 027104.
- [69] Rodriguez, F. & Mesler, R., 1985 Some drops don't splash. *Journal of colloid and interface science* **106**, 347–352.
- [70] Rein, M., 1993 Phenomena of liquid drop impact on solid and liquid surfaces. *Fluid Dynamics Research* **12**, 61.
- [71] Leng, L. J., 2001 Splash formation by spherical drops. *Journal of Fluid Mechanics* **427**, 73–105.
- [72] Manzello, S. L., 2002 An experimental study of a water droplet impinging on a liquid surface. *Experiments of Fluids* **32**, 580.
- [73] Ray, B., Biswas, G. & Sharma, A., 2015 Regimes during liquid drop impact on a liquid pool. *Journal of Fluid Mechanics* **768**, 492–523.

- [74] Hendrix, M. H., Bouwhuis, W., van der Meer, D., Lohse, D. & Snoeijer, J. H., 2016 Universal mechanism for air entrainment during liquid impact. *Journal of fluid mechanics* **789**, 708–725.
- [75] Thoroddsen, S. T. & Takehara, K., 2000 The coalescence cascade of a drop. *Physics of Fluids* **12**, 1265–1267.
- [76] Tran, T., de Maleprade, H., Sun, C. & Lohse, D., 2013 Air entrainment during impact of droplets on liquid surfaces. *Journal of Fluid Mechanics* **726**.
- [77] Agbaglah, G., Thoraval, M.-J., Thoroddsen, S., Zhang, L., Fezzaa, K. & Deegan, R., 2015 Drop impact into a deep pool: vortex shedding and jet formation. *Journal of fluid mechanics* **764**, 1–12. ISSN 0022-1120.
- [78] Dickerson, A. & Stephen, J., 2017 On the reduction of splash-back. In *APS Division of Fluid Dynamics Meeting Abstracts*, APS Meeting Abstracts, p. L6.011.
- [79] Watson, D., Bom, J., Souchik, C. & Dickerson, A., 2019 Underwater acrobatics of partially-coated spheres. *Bulletin of the American Physical Society* .
- [80] Watson, D., Souchik, C., Bom, J. & Dickerson, A., 2019 Water entry of hydrophilic spheres through fabric-fluid interfaces. *Bulletin of the American Physical Society* .
- [81] Watson, D., Kahn, H., Diamco, R. & Dickerson, A., 2019 On the survival of water striders during raindrop impacts. In *Integrative and Comparative Biology*, volume 59, pp. E242–E242. Oxford University Press Inc. Journals Department.
- [82] Lee, M., Longoria, R. & Wilson, D., 1997 Cavity dynamics in high-speed water entry. *Physics of Fluids* **9**, 540–550.
- [83] Cross, R., 2016 Vertical impact of a sphere falling into water. *The Physics Teacher* p. 153. ISSN 0031-921X.

- [84] Krishnan, S. R. & Seelamantula, C. S., 2013 On the selection of optimum savitzky-golay filters. *IEEE Transactions on Signal Processing* **61**, 380–391. ISSN 1053-587X.
- [85] Ishikawa, T. & Chou, T.-W., 1982 Stiffness and strength behaviour of woven fabric composites. *Journal of Materials Science* **17**, 3211–3220.
- [86] Chou, T.-W. & Ishikawa, T., 1983 One-dimensional micromechanical analysis of woven fabric composites. *AIAA journal* **21**, 1714–1721.
- [87] Ishikawa, T. & Chou, T.-W., 1983 Nonlinear behavior of woven fabric composites. *Journal of composite materials* **17**, 399–413.
- [88] Ishikawa, T., Matsushima, M., Hayashi, Y. & Chou, T.-W., 1985 Experimental confirmation of the theory of elastic moduli of fabric composites. *Journal of Composite Materials* **19**, 443–458.
- [89] Dow, N. F., Ramnath, V. & Rosen, B. W., 1987 Analysis of woven fabrics for reinforced composite materials .
- [90] Naik, N., Shembekar, P. & Hosur, M., 1991 Failure behavior of woven fabric composites. *Journal of Composites, Technology and Research* **13**, 107–116.
- [91] Naik, N. & Shembekar, P., 1992 Elastic behavior of woven fabric composites: i—lamina analysis. *Journal of composite materials* **26**, 2196–2225.
- [92] Naik, N. & Shembekar, P., 1992 Elastic behavior of woven fabric composites: iii—laminated design. *Journal of composite materials* **26**, 2522–2541.
- [93] Naik, R. A., 1995 Failure analysis of woven and braided fabric reinforced composites. *Journal of Composite Materials* **29**, 2334–2363.

- [94] Shembekar, P. & Naik, N., 1992 Elastic behavior of woven fabric composites: ii—laminare analysis. *Journal of Composite Materials* **26**, 2226–2246.
- [95] LIU, Y., HE, H. & YAO, J., 2009 Mathematical model for knitted bodywear based on fabric elasticity [j]. *Journal of Textile Research* **4**.
- [96] Zhu, D., Mobasher, B. & Rajan, S. D., 2010 Dynamic tensile testing of kevlar 49 fabrics. *Journal of Materials in Civil Engineering* **23**, 230–239.
- [97] Epps, B. P., Truscott, T. T. & Techet, A. H., 2010 Evaluating derivatives of experimental data using smoothing splines. In *Proceedings of Mathematical Methods in Engineering International Symposium. MMEI, Lisbon Portugal*.
- [98] Maxworthy, T., 1965 Accurate measurements of sphere drag at low reynolds numbers. *Journal of Fluid Mechanics* **23**, 369–372.
- [99] Maxworthy, T., 1969 Experiments on the flow around a sphere at high reynolds numbers. *Journal of Applied Mechanics* **36**, 598–607.
- [100] Achenbach, E., 1972 Experiments on the flow past spheres at very high reynolds numbers. *Journal of Fluid Mechanics* **54**, 565–575.
- [101] Lofquist, K. E. & Purtell, L. P., 1984 Drag on a sphere moving horizontally through a stratified liquid. *Journal of Fluid Mechanics* **148**, 271–284.
- [102] Pochiraju, K. & Chou, T.-W., 1999 Three-dimensionally woven and braided composites. i: A model for anisotropic stiffness prediction. *Polymer Composites* **20**, 565–580.
- [103] Dai, X., Li, Y. & Zhang, X., 2003 Simulating anisotropic woven fabric deformation with a new particle model. *Textile research journal* **73**, 1091–1099.

- [104] Kovar, R. & Gupta, B. S., 2009 Study of the anisotropic nature of the rupture properties of a plain woven fabric. *Textile Research Journal* **79**, 506–516.
- [105] Morris, R., 1959 Single-factor analysis in population dynamics. *Ecology* **40**, 580–588.
- [106] St, L., Wold, S. *et al.*, 1989 Analysis of variance (anova). *Chemometrics and intelligent laboratory systems* **6**, 259–272.
- [107] Peters, W. & Spurgeon, J., 1971 Biology of the water-boatman *krizousacorixa femorata* (heteroptera: Corixidae). *The American Midland Naturalist* **86**, 197–207. ISSN 00030031, 19384238.
- [108] Blake, R. W., 1986 Hydrodynamics of swimming in the water boatman, *cenocorixa bifida*. *Canadian Journal of Zoology* **64**, 1606–1613. (doi:10.1139/z86-242).
- [109] Jones, D., 1966 Factors affecting the recovery from diving bradycardia in the frog. *Journal of Experimental Biology* **44**, 397–411.
- [110] West, N. H. & Jones, D. R., 1976 The initiation of diving apnoea in the frog, *rana pipiens*. *Journal of Experimental Biology* **64**, 25–38.
- [111] Kubota, Y., Mochizuki, O. *et al.*, 2015 Splash formation due to a frog diving into water. *World Journal of Mechanics* **5**, 129.
- [112] Owre, O. T., 1967 Adaptations for locomotion and feeding in the anhinga and the double-crested cormorant. *Ornithological Monographs* pp. 1–138. ISSN 00786594, 19412282.
- [113] Hustler, K., 1992 Buoyancy and its constraints on the underwater foraging behaviour of reed cormorants *phalacrocorax africanus* and darters *anhinga melanogaster*. *Ibis* **134**, 229–236. (doi:10.1111/j.1474-919X.1992.tb03804.x).

- [114] Ryan, P. G., 2007 Diving in shallow water: the foraging ecology of darters (aves: Anhingidae). *Journal of Avian Biology* **38**, 507–514. (doi:10.1111/j.0908-8857.2007.04070.x).
- [115] Speirs, N., Mansoor, M., Hurd, R., Sharker, S., Robinson, W., Williams, B. & Truscott, T., 2018 Entry of a sphere into a water-surfactant mixture and the effect of a bubble layer. *Physical Review Fluids* **3**, 104004.
- [116] de Ruiter, J., Pepper, R. E. & Stone, H. A., 2010 Thickness of the rim of an expanding lamella near the splash threshold. *Physics of Fluids* **22**, 022104. (doi:10.1063/1.3313360).
- [117] Lebanoff, A. P. & Dickerson, A. K., 2020 Drop impact onto pine needle fibers with non-circular cross section. *Physics of Fluids* **32**, 092113. (doi:10.1063/5.0019310).
- [118] Hollies, N. R., Kaessinger, M. M., Watson, B. S. & Bogaty, H., 1957 Water transport mechanisms in textile materials: Part ii: Capillary—type penetration in yarns and fabrics. *Textile Research Journal* **27**, 8–13.
- [119] Watson, D. A., 2016 *Realization of an open-source software of computation for the optimization of hybrid renewable energy systems: application in the Caribbean region*. mathe-sis, University of the West Indies.
- [120] Watson, D., Binnie, Y., Duncan, K. & Dorville, J.-F., 2017 Photurgen: The open source software for the analysis and design of hybrid solar wind energy systems in the caribbean region: A brief introduction to its development policy. *Energy Reports* **3**, 61 – 69. ISSN 2352-4847. (doi:https://doi.org/10.1016/j.egy.2017.03.001).
- [121] Alam, M. E., Smith, N., Watson, D., Hassan, T. & Neupane, K., 2019 Early screening of ddh using svm classification. In *2019 SoutheastCon*, pp. 1–4. ISSN 1558-058X. (doi: 10.1109/SoutheastCon42311.2019.9020565).